

BRNO UNIVERSITY OF TECHNOLOGY

Faculty of Electrical Engineering
and Communication

DOCTORAL THESIS

Brno, 2021

Ing. Jan Dušek



BRNO UNIVERSITY OF TECHNOLOGY

VYSOKÉ UČENÍ TECHNICKÉ V BRNĚ

FACULTY OF ELECTRICAL ENGINEERING AND COMMUNICATION

FAKULTA ELEKTROTECHNIKY
A KOMUNIKAČNÍCH TECHNOLOGIÍ

DEPARTMENT OF THEORETICAL AND EXPERIMENTAL ELECTRICAL ENGINEERING

ÚSTAV TEORETICKÉ A EXPERIMENTÁLNÍ ELEKTROTECHNIKY

OPTIMIZING IMAGE RECONSTRUCTION IN ELECTRICAL IMPEDANCE TOMOGRAPHY

OPTIMALIZACE REKONSTRUKCE OBRAZU V ELEKTRICKÉ IMPEDANČNÍ TOMOGRAFII

DOCTORAL THESIS
DIZERTAČNÍ PRÁCE

AUTHOR
AUTOR PRÁCE

Ing. Jan Dušek

SUPERVISOR
ŠKOLITEL

doc. Ing. Jan Mikulka, Ph.D.

BRNO 2021

ABSTRACT

The thesis presents, analyzes, and discusses the optimization of algorithms that reconstruct images of unknown specific conductivity from data acquired via electrical impedance tomography. In this context, the author provides a brief mathematical description of the forward and inverse tasks solved by using diverse approaches, characterizes relevant measurement techniques and data acquisition procedures, and discusses available numerical tools. Procedurally, the initial working stages involved analyzing the methods for optimizing those parameters of the model that influence the reconstruction accuracy; demonstrating approaches to the parallel processing of the algorithms; and outlining a survey of available instruments to acquire the tomographic data. The obtained knowledge then yielded a process for optimizing the parameters of the mathematical model, thus allowing the model to be designed precisely, based on the measured data; such a precondition eventually reduced the uncertainty in reconstructing the specific conductivity distribution. When forming the numerical model, the author investigated the possibilities and overall impact of combining the open and closed domains with various regularization methods and mesh element scales, considering both the character of the conductivity reconstruction error and the computational intensity. A complementary task resolved within the broader scheme outlined above lay in parallelizing the reconstruction subalgorithms by using a multi-core graphics card. The results of the thesis are directly reflected in a reduced reconstruction uncertainty (through an optimization of the initial conductivity value, placement of the electrodes, and shape deformation of the domains) and accelerated computation via parallelized algorithms. The actual research benefited from an in-house designed automated tomography unit.

KEYWORDS

Electrical impedance tomography, optimization of domain parameters, electrode placement, current patterns, conductivity, data acquisition unit

ABSTRAKT

Tato disertační práce pojednává o optimalizaci algoritmů pro rekonstrukci obrazu neznámé měrné vodivosti z měřených dat pořízených elektrickou impedanční tomografií. Danou problematiku zde věcně vymezuje několik různých prvků, zejména pak stručný matematický popis dopředné a inverzní úlohy řešené různými přístupy, metodika měření a pořizování dat pro rekonstrukci a přehled dostupných numerických nástrojů. Uvedenou charakteristiku rozšiřuje rozbor optimalizací parametrů modelu ovlivňujících přesnost rekonstrukce, způsoby paralelního zpracování algoritmů a souhrn dostupných zařízení pro měření tomografických dat. Na základě získaných poznatků byla navržena optimalizace parametrů matematického modelu, která umožňuje jeho velmi přesný návrh dle měřených dat. V této souvislosti dochází ke snížení nejistoty rekonstrukce rozložení konduktivity. Pro zefektivnění procesu získávání dat bylo navrženo zařízení k automatizaci tomografie s důrazem na cenovou dostupnost a snížení nejistoty měření. V oblasti tvorby numerického modelu byly dále zkoumány možnosti užití otevřených a uzavřených domén pro různé metody regularizace a hrubost sítě, a to s ohledem na velikost chyby rekonstruované konduktivity a výpočetní náročnost. Součástí práce je také paralelizace subalgoritmů rekonstrukce s využitím vícejádrové grafické karty. Předložené výsledky mají přímý vliv na snížení nejistoty rekonstrukce (optimalizací počáteční hodnoty konduktivity, rozmístění elektrod a tvarové deformace domény, regularizačních metod a typu domén) a urychlení výpočtů paralelizací algoritmů, přičemž výzkum byl podpořen vlastním návrhem jednotky pro automatizaci tomografie.

KLÍČOVÁ SLOVA

Elektrická impedanční tomografie, optimalizace parametrů domény, rozmístění elektrod, proudové vzory, měrná konduktivita, měřicí jednotka

DUŠEK, Jan. *Optimizing Image Reconstruction in Electrical Impedance Tomography*.
Brno: Brno University of Technology, Faculty of Electrical Engineering and Communica-
tion, Department of Theoretical and Experimental Electrical Engineering, 2021, 123 p.
Doctoral thesis. Advised by Assoc. Prof. Jan Mikulka

Author's Declaration

Author: Jan Dušek, M.Sc.
Author's ID: 146814
Paper type: Doctoral thesis
Academic year: 2021/22
Topic: Optimizing Image Reconstruction
in Electrical Impedance Tomography

I declare that I have written this thesis independently, under the guidance of the supervisor and using exclusively the technical references and other sources of information cited in the text and listed in the comprehensive bibliography at the end of the thesis.

As the author, I furthermore declare that, with respect to the creation of this thesis, I have not infringed any copyright or violated anyone's personal and/or ownership rights. In this context, I am fully aware of the consequences of breaking the provisions of Regulation §11 of the Copyright Act No.121/2000 Coll. of the Czech Republic, as amended, and I recognize the impact of any breach of rights relating to intellectual property or introduced within amendments to relevant Acts such as the Intellectual Property Act or the Criminal Code, Act No. 40/2009 Coll. of the Czech Republic, Section 2, Title VI, Part 4.

Brno,

.....

author's signature*

*The author signs only in the printed version.

ACKNOWLEDGEMENT

I am deeply indebted to my advisor, Assoc. Prof. Jan Mikulka, for his unwavering support, patience, encouragement, and motivation during my Ph.D. studies. His guidance and profound knowledge helped me to find the way through the research and to complete the thesis.

My sincere thanks also go to Prof. Tomasz Rymarczyk and Andrés Véjar, Ph.D. for facilitating my internship at the Lublin-based Netrix Research and Development Center and supervising me in a project focused on domain modeling.

I thank Assoc. Prof. Jana Pařílková and Zuzana Münsterová, M.Sc. for their cooperation, encouragement, insightful comments, and preparation of the experiments within the interfaculty project FAST/FEKT-J-18-5385.

By extension, a great thank you should not be owed to Přemysl Dohnal, M.A. for patiently reading, commenting on, and editing a substantial portion of the original text.

Last but not least, none of the efforts herein would have materialized without the care and inspiration granted by my family and close relatives.

Contents

Introduction	12
1 Electrical impedance tomography	14
1.1 Mathematical formulation	15
1.2 Forward problem	17
1.3 Inverse problem: deterministic approaches	19
1.4 Inverse problem: stochastic methods	23
1.5 Inverse crime	26
1.6 Measurement strategies: current patterns	29
1.7 EIDORS library	33
1.8 Domain meshing	35
1.9 Complete electrode model parameters	39
1.10 Approaches to solving the domain parameters	41
1.11 Algorithm parallelization	47
1.12 Instrumentation and devices	48
2 Aims and objectives	50
3 Experiments	51
3.1 Optimizing the domain parameters	52
3.2 Hardware for the tomographic measurement	68
3.3 Error exploration in the open and closed domains	83
3.4 Parallelization	92
Discussion	96
Conclusion	100
Bibliography	101
Author's publications	113
Symbols	116
Abbreviations	119
A Preliminary results	122

List of figures

1.1	The domain Ω ; the electrodes, current feeding, and voltage sensing [9].	14
1.2	A basis function for approximating via the FEM; φ_i denotes the approximation function, and x_i is a node of the mesh [17].	18
1.3	A multilayer artificial neural network.	23
1.4	A structural flowchart to illustrate a genetic algorithm.	25
1.5	The adjacent stimulation pattern [37].	29
1.6	The opposite stimulation pattern [37].	30
1.7	Trigonometric driving [37].	30
1.8	The Wenner scheme-based arrangement [13].	31
1.9	The Schlumberger approach in use [13].	31
1.10	Sample FEM-based models with inserted electrodes: A 2D and a 3D domains generated via Distmesh and Netgen, respectively [39].	33
1.11	The initial model with an inserted inhomogeneity (left) and the reconstructed conductivity distribution (right) [39].	34
1.12	An extended 2D mesh of a geophysical domain [13].	35
1.13	A simple 3D domain to allow water dam imaging [7].	35
1.14	A complex geophysical 3D domain for ERT imaging [40].	36
1.15	An image reconstruction domain generated with EIDORS [13].	37
1.16	The impact of precise inhomogeneity meshing [41].	38
1.17	The design and equivalent diagrams of a compound (a,b) and a simple (c,d) electrodes [44].	41
1.18	Top left: The measurement setup. Top right: Reconstructing the isotropic conductivity. Bottom left: Reconstructing the isotropic conductivity by using an incorrect model. Bottom right: The uniformly anisotropic conductivity in a deformed domain. The displayed quantity is η [AU] [47].	42
1.19	Various MAP estimates with simulated data; Δ_σ denotes the relative errors, and N_n represents the number of nodes in the mesh [49].	43
1.20	The concurrently reconstructed conductivity distribution and electrode location, as compared with the fixed placement [50].	44
1.21	The electrode placement computed through the Bayesian approach, utilizing Fréchet derivatives for non-circular shapes [52].	45
1.22	Optimizing the electrode placement with a neural network [54].	46
1.23	The elements forming an EIT data acquisition system.	48
3.1	The Nelder-Mead method [81].	52
3.2	The flowchart of the optimization procedure based on the measured dataset and selected parameters [81].	54

3.3	The tomograph and the related Netgen-based numerical model [81].	55
3.4	The data acquisition setup [81].	56
3.5	The variation of the (a) minimization function, and (b) conductivity value during the optimization [81].	56
3.6	(a) The variation of the diameters on the axes X and Y, relating to the OSP in the non-optimized (solid lines) and optimized (dotted lines) scenarios, and (b) the tomograph containing water and an inserted aluminum pipe [81].	58
3.7	The conductivity distribution in the water with an inserted aluminum object, obtained through the ASP (top) and the OSP (bottom). The tomograph's axial dimensions equal $X = 18.6$ cm and $Y = 19.4$ cm; (a,c) wrongly selected circular shapes, and (b,d) the true model of the elliptic domain [81].	59
3.8	(a) The setup including the shifted 6 th electrode (highlighted in yellow); (b) the circular tomograph filled with water, comprising an aluminum object [81].	60
3.9	Optimizing the electrode misplacement: (a) the error associated with the minimization function, varying with iteration; (b) the function count [81].	61
3.10	A top view of the optimized domain meshes, focusing on the electrode shift in the (a) circular and (b) elliptic shapes [81].	62
3.11	A top view of the opposite sensing-optimized models, focusing on the electrode misplacement. The images display a duality of the solution, with either (a) the 2 nd or (b) the 6 th electrode shifted [81].	62
3.12	The reconstructed conductivity distributions in the (a) inaccurate regular electrode setup and (b) correct placement of the 6 th electrode [81].	63
3.13	The PLI EIT system [88].	68
3.14	The dual op-amp Howland current source.	70
3.15	The photorelay switching of the current source and the voltmeter [88].	72
3.16	The measuring branch containing a programmable gain amplifier, a filter, an ADC, and a hysteresis comparator.	74
3.17	The PLI EIT prototype [88].	75
3.18	The frequency characteristics of the multiplexer's resistance, reactance, impedance, and phase.	76
3.19	(a) A diagram characterizing the voltage and phase shift measurement circuit; (b) the tomograph with an inserted graduated cylinder [91].	77

3.20	The sequences of (a) the voltage and (b) the phase shift of the signals between the pairs of excitation and measuring electrodes. The sensing of the homogeneous and the inhomogeneous media is illustrated by the blue and the red teeth, respectively [91].	78
3.21	The reconstructed difference in the admittivity distribution: three-dimensional cross-sectional images (top), and two-dimensional cross-sections at the electrode level (bottom) [91].	80
3.22	The unstructured mesh for the closed domain, including the point electrodes and two square subspaces to accommodate the inhomogeneities [92, 93].	83
3.23	The unstructured open domain mesh. The left-hand image shows a detail of the domain; this detail corresponds to the closed domain. On the right-hand side, we display a domain extension with the side length 10 times greater than in the closed domain [92, 93].	84
3.24	An example of the discretization error differences between a regular and an "ugly" optimized adaptive mesh [94].	84
3.25	The individual stages in evaluating the domains [92].	85
3.26	The reconstruction in the closed (top) and the open (bottom; zoomed to detail at the regions of interest) domains, executed via the Gauss-Newton method including the Tikhonov penalty. The left-hand column shows the original closed and open domains (4,463 and 4,734 elements) with inserted inhomogeneities; the right-hand column then presents an inverse image computed on a mesh of 3,433 and 2,712 items relating to the closed and the open domains, respectively [92].	86
3.27	The relationship between the number of mesh elements and the computational time in the selected reconstruction methods [92].	87
3.28	The error convergence estimates normalized in the range of 0 to 1, characterizing the closed (left-hand column) and the open (right-hand column) domains and considering the numbers of mesh elements and regularizations [92].	88
3.29	The flowchart of the forward and the inverse tasks [96].	92
3.30	The flowcharts of the A) sequential and B) the parallel implementations of the Jacobian [96].	93
3.31	The flowcharts of the differently processed forward and inverse tasks [97].	94
A.1	(a) The setup of the experiment; (b) the conductivity distribution of the soil sample, computed via a difference inverse algorithm [99].	122
A.2	(a) The setup of the experiment, and the reconstructed differences of the (b) real and the (c) imaginary parts of admittivity [100].	123

List of tables

1.1	The Wenner measurement sequence.	32
1.2	The Schlumberger measurement sequence.	32
1.3	Comparing the stimulation patterns in terms of the individual parameters and current injection requirements [42, 43].	40
1.4	The most widely favored EIT systems/devices.	49
3.1	Comparing the stimulation patterns in terms of the actual parameters and current injection values [81].	57
3.2	The image errors in the boundary deformations [81].	64
3.3	The image errors and electrode positioning [81].	65
3.4	The ideal parameters of the equipment.	69
3.5	Some of the amplifiers for the dual op-amp Howland current source.	71
3.6	Selected multiplexers and their parameters.	71
3.7	A selection of suitable amplifiers.	72
3.8	A selection of suitable ADCs.	73
3.9	A selection of convenient comparators.	73
3.10	The Jaccard distance, MMSE, and SSE: The values over the mesh element scale provided by the selected regularization methods [92].	89
3.11	Comparing the Jacobian computing procedures [96].	94
3.12	The computational times in the individual reconstruction steps: the CPU- and GPU-based procedures [97].	95
3.13	The regularization approaches compared in terms of the Jaccard distance, MMSE, and SSE over the mesh element scale.	98

Introduction

This doctoral thesis discusses current challenges in electrical impedance tomography (EIT), a relatively new, non-destructive and non-invasive diagnostic method that, thanks to its properties and capabilities, is advantageously applied in various fields of technology. An acceptable cost and practical design of the equipment then make EIT an inexpensive and effective data acquisition technique.

From the historical perspective, EIT image reconstruction was invented in response to various needs of geophysical exploration. At this point, two landmarks need to be mentioned: the first reconstruction and the proof of uniqueness. In the 1930s, the initial, regularization-based reconstruction was published by Tikhonov, who consequently received the Soviet state award for his efforts. More concretely, the scientist's research was focused on the detection of copper deposits, and the innovative algorithms paved the way for survey procedures that materialized successfully in the 1940s [1]. The other major breakthrough, namely, the proof of the uniqueness of an inverse ill-posed problem, was introduced by the Argentinian mathematician Albert Calderón in 1980 [1, 2].

In functional terms, the method applies an AC current to an electrode system. The electrodes are usually placed equidistantly on the border of the examined object (domain), except in geophysical measurement. The voltage is commonly measured on the non-current carrying electrodes, and the relevant values correspond to the magnitude of the flowing current and the conductivity or impedivity distribution inside the domain. Based on the obtained results, the inverse task is processed and the inverse image calculated. Overall, the spatial resolution of the reconstructed image is improvable by increasing the number of electrodes.

The outlined properties enable EIT to be employed in a variety of science and technology fields, such as biomedicine, material engineering, geophysical mapping, and monitoring of chemical processes. In biomedicine, EIT finds use in imaging centered on tissues and internal body structures. The imaging, i.e., the reconstruction, is generally static or dynamic, and it facilitates detecting or monitoring blood clots [3], tumors, brain hemorrhages, lungs, oxygenation during the respiration cycle [4], and other issues or parts of the body.

In material engineering, EIT has become popular thanks to its non-destructive character. By extension, non-destructive diagnostics embodies one of the most convenient approaches wherever the detection of inhomogeneous particles, cracks, defects, and corrosion is indispensable. EIT, however, also allows destructive inspection of reinforced concrete beams to determine the strength limits and to detect cracks during stress tests [5].

In recent years, EIT has established itself firmly in chemistry, with some of the

most frequent applications being in the precise monitoring of chemical emulsions to perform process tomography; the method then enables the observation of various substances in emulsions on the one hand and facilitates the quantification of the conductivity distribution during mixing on the other [6].

Within geophysical mapping, EIT monitors or explores structurally the formation of subsoils and observes underground watercourses or flood embankments. The detection of local subsoil inhomogeneities can highlight areas having a higher water content or different material composition and allows tracking the changes over time [7]. Another, albeit only experimental, target field is the monitoring of volcanoes [8].

One of the topical problems in EIT rests in optimizing algorithms with respect to image reconstruction; functionally, the optimization can be carried out through novel numerical methods (e.g., the non-iterative D-Bar method with scattering transformation), precise FEM modeling (domain deformation, electrode placement, contact impedance), suppressing undesired changes in the tomographic domain (e.g., during breathing), and eliminating the measurement uncertainties (such as the stability of the current sources, and phase shift sensing). The thesis focuses on the precise FEM-based modeling, for which an optimization process using EIDORS was designed. The numerical solution was correlated with diverse laboratory experiments to verify the optimization functionality.

The thesis contains relevant experiments and results executed or otherwise acquired within cooperation between the Faculty of Electrical Engineering and Communication and the Faculty of Civil Engineering, Brno University of Technology. Additionally, the experimental chapters present the deterministic methods practised during the author's internship at Netrix (Net-Art) Research and Development center, Lublin, Poland.

1 Electrical impedance tomography

Electrical impedance tomography is a diagnostic method for estimating the conductivity or impedivity distribution in conductive objects. To illustrate the underlying concept in general terms, we can imagine a domain Ω having a pre-defined shape and material properties (Fig. 1.1). As is shown in the figure below, selected pairs of electrodes on the domain border are fed with a current whose response is observable via voltage measurement. Naming and characterizing the main relevant procedures

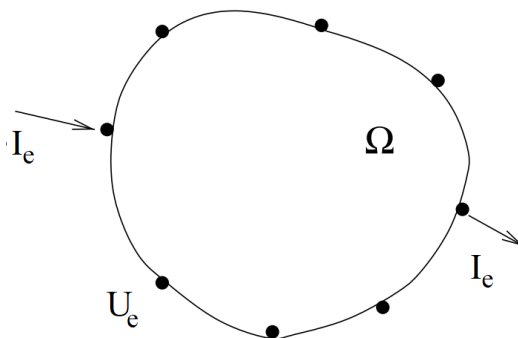


Fig. 1.1: The domain Ω ; the electrodes, current feeding, and voltage sensing [9].

requires us to note that the approximation of the conductivity inside the domain is referred to as *image reconstruction* and that, in EIT, this activity comprises two main processes: the forward and the inverse tasks [2, 10].

The forward task calculates the voltage on the electrodes with respect to the conductivity distribution inside a domain. The inverse task, by contrast, is a non-linear ill-posed problem which evaluates the estimated conductivity distribution from the measured voltages. The ill-posedness means that minor undesired changes or flaws occurring at the beginning of the process can produce markedly more significant errors in the final estimated conductivity. Thus, special numerical techniques have been invented to improve the stability of the inverse solution; these tools (and procedures) are called *regularizations*. The central aims of a regularization include minimizing the spurious effects that accompany the construction of the model, reducing the numerical instability, and diminishing the impact of the measurement uncertainty. In practice, there exist problematic conductivity distribution cases, such as scenarios where the measured voltage values almost match those of the noise or where the model was constructed inaccurately. Any acquired data affected by a high measurement uncertainty or wrong construction of the model can produce differences between the results of the real conductivity and its estimated form delivered by the inverse task [11, 12].

1.1 Mathematical formulation

The mathematical model for EIT was derived from the first (Ampere's law, 1.1) and the second (Faraday's law of induction, 1.2) Maxwell's equations in the differential form, reading

$$\nabla \times \mathbf{H} = \mathbf{J} + \frac{\partial \mathbf{D}}{\partial t}, \quad (1.1)$$

$$\nabla \times \mathbf{E} = -\frac{\partial \mathbf{B}}{\partial t}, \quad (1.2)$$

where \mathbf{H} is a magnetic field strength, \mathbf{J} denotes an electric current density, \mathbf{D} represents an electric induction, \mathbf{E} stands for an electric field, and \mathbf{B} is a magnetic flux density.

The above equations, 1.1 and 1.2, are related through the vector quantities indicated below. In this context, equation 1.3 describes Ohm's law for the vector of the current density \mathbf{J} , which equals a conductivity σ and the vector of the electric field \mathbf{E} ; equation 1.4 defines the vector of the electric induction \mathbf{D} , which equals the vector of the electric field \mathbf{E} and a permittivity ϵ ; and equation 1.5 characterizes the magnetic flux density \mathbf{B} as equaling the intensity of the magnetic field strength \mathbf{H} , and a permeability μ . The discussed equations

$$\mathbf{J} = \sigma \mathbf{E}, \quad (1.3)$$

$$\mathbf{D} = \epsilon \mathbf{E}, \quad (1.4)$$

$$\mathbf{B} = \mu \mathbf{H} \quad (1.5)$$

are valid for a linear and isotropic system. In a system fed with a DC or an AC current at a low frequency, the change of the electric and the magnetic inductions in time can be considered virtually negligible, almost equaling zero [11, 13], defined as

$$\frac{\partial \mathbf{D}}{\partial t} = 0, \quad (1.6)$$

$$\frac{\partial \mathbf{B}}{\partial t} = 0. \quad (1.7)$$

Substituting eqs. 1.6 and 1.7 in the Maxwell's equations (1.1 and 1.2) will yield the statements

$$\nabla \times \mathbf{H} = \mathbf{J}, \quad (1.8)$$

$$\nabla \times \mathbf{E} = 0. \quad (1.9)$$

Of these, item 1.9 clearly indicates that the rotation of the electric field equals zero. Considering that the field has a quasistatic character, we can substitute the rotation with the gradient of the scalar potential φ , obtaining

$$\mathbf{E} = -\nabla \varphi. \quad (1.10)$$

After that, the Ohm's law from 1.3 is integrated in statement 1.8, and the divergence operator is applied. At the last stage of the EIT formulation procedure, the vector of the electric field is replaced with the scalar potential from 1.10, through the following steps:

$$\nabla \times \mathbf{H} = \sigma \mathbf{E}, \tag{1.11}$$

$$\nabla(\nabla \times \mathbf{H}) = \nabla(\sigma \mathbf{E}), \tag{1.12}$$

$$\nabla(\sigma \mathbf{E}) = 0, \tag{1.13}$$

$$-\nabla(\sigma \nabla \varphi) = 0. \tag{1.14}$$

The resulting statement (1.14), namely, the Laplace equation, describes the behavior of the electric potential inside the domain Ω , and its solution is supposed to be in accordance with the Dirichlet and Neumann conditions on the domain's boundary. The boundary conditions are processed via the forward problem [13, 14].

1.2 Forward problem

The EIT physical model of the forward problem is based on describing the domain Ω in an \mathbb{R}^n , $n = 1, 2, 3$ -dimensional space. We assume that the domain exhibits a smooth and continuous boundary, with the electrodes placed equidistantly on the domain's surface. An AC current is injected into the volume of the domain through the electrodes; the flowing current then causes voltage drops, whose magnitude depends on the applied medium. The forward problem (or, by another definition, injecting the current and measuring the voltage on the electrodes with respect to the conductivity of the medium) is best illustrated by the complete electrode model (CEM), as follows:

$$\nabla(\sigma(x)\nabla\varphi(x)) = 0, x \in \Omega, \quad (1.15)$$

$$\varphi(x) + \hat{\mathbf{z}}_l\sigma(x)\frac{\partial\varphi(x)}{\partial\mathbf{n}} = U_l, x \in E_l, l \in (1, L), \quad (1.16)$$

$$\int_{E_l} \sigma(x)\frac{\partial\varphi(x)}{\partial\mathbf{n}}dS = I_l, l \in (1, L), \quad (1.17)$$

$$\sigma(x)\frac{\partial\varphi(x)}{\partial\mathbf{n}} = 0, x \in \partial\Omega \setminus \bigcup_{l=1}^L E_l, \quad (1.18)$$

$$\sum_{l=1}^L I_l = 0, \quad (1.19)$$

$$\sum_{l=1}^L U_l = 0, \quad (1.20)$$

where x represents a coordinate of the domain Ω ; $\sigma(x)$ denotes the conductivity of the examined medium; $\varphi(x)$ describes the electric potential inside the domain; U_l and I_l are the voltage and the current, respectively, on the electrodes l ; $\hat{\mathbf{z}}_l$ expresses the contact impedance between an electrode and the unknown conductivity; \mathbf{n} stands for the normal vector with respect to the surface of the domain Ω ; and dS is the domain's surface. The last two equations, 1.19 and 1.20, express Kirchhoff's laws within the physical formulation of the forward problem [2, 13, 14].

The numerical calculation is stable and unambiguous, and the actual solution exploits discretization; the partial differential equations (PDEs) are then usually approximated with the finite element method (FEM). By extension, discretizing the problem via the FEM leads to the following equation:

$$\varphi(x) = \sum_e \sum_n \varphi_{e,n}(x)W_{e,n}(x, y), \quad (1.21)$$

where $\varphi(x)$ is the electric potential, $\varphi_{e,n}(x)$ denotes the potential in the nodes of the mesh, and $W_{e,n}(x, y)$ represents a basis function to facilitate the approximation. Multiple basis functions are available, including, for example, the linear, quadratic,

and sine variants. The most common approach rests in the linear basis function¹ (Fig. 1.2), which complies with the homogeneous boundary conditions² [15, 16].

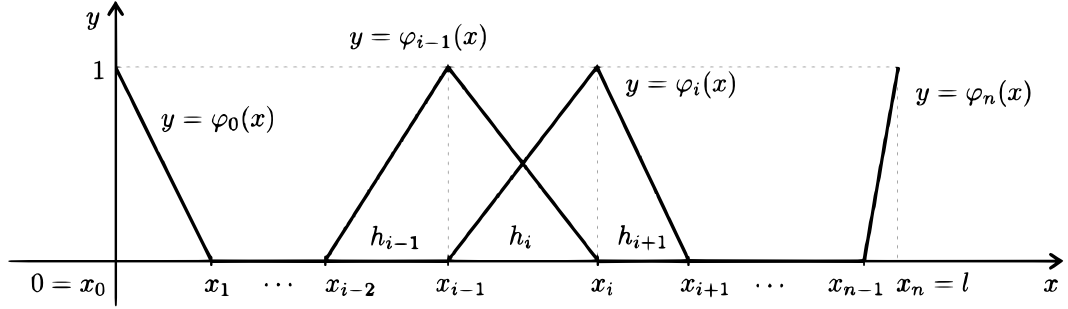


Fig. 1.2: A basis function for approximating via the FEM; φ_i denotes the approximation function, and x_i is a node of the mesh [17].

The discretization using the above CEM equations, 1.15 - 1.20, could be performed via the FEM to yield the term³

$$\mathbf{K}\boldsymbol{\varphi} = \mathbf{f}, \quad (1.22)$$

where \mathbf{K} denotes the FEM matrix of the system (stiffness matrix), $\boldsymbol{\varphi}$ expresses the vector of the electric potential, and \mathbf{f} represents the load vector [11, 17].

The equation can be rewritten to read

$$\begin{bmatrix} \mathbf{G} + \mathbf{B} & \mathbf{C} \\ \mathbf{C}^T & \mathbf{D} \end{bmatrix} \begin{bmatrix} \boldsymbol{\varphi}_x \\ \boldsymbol{\varphi}_e \end{bmatrix} = \begin{bmatrix} \mathbf{0} \\ \mathbf{i} \end{bmatrix}, \quad (1.23)$$

where $\boldsymbol{\varphi}_x$ characterizes the vector of the electric potential on the mesh nodes, $\boldsymbol{\varphi}_e$ denotes the potential measured on the electrodes, and \mathbf{i} expresses the vector of the injected currents. The remaining matrix elements, i.e, \mathbf{G} , \mathbf{B} , \mathbf{C} , \mathbf{D} , are defined as

$$G_{i,j} = \int_{\Omega} \sigma \nabla W_i \nabla W_j d\Omega, \quad (1.24)$$

$$B_{i,j} = \sum_{l=1}^L \int_{E_l} W_i W_j, \quad (1.25)$$

$$C_{l,j} = -\frac{1}{\hat{\mathbf{z}}_l} \int_{E_l} W_j, \quad (1.26)$$

$$D_{i,j} = \frac{|E_l|}{\hat{\mathbf{z}}_l} (\text{with } i = j = l \text{ equaling } 0), \quad (1.27)$$

where W describes the linear basis functions, σ denotes the conductivity, $\hat{\mathbf{z}}_l$ characterizes the contact impedance between an electrode and the medium inside the domain, and $|E_l|$ stands for the surface of an electrode [13, 18].

¹A linearly independent basis function.

²The homogeneous boundary condition equals zero on the border of the domain Ω .

³The complete, step-by-step derivation of the formula is described within the monograph [2].

1.3 Inverse problem: deterministic approaches

Generally, the inverse problem is defined as an ill-posed mathematical task; in EIT, the relevant procedure consists in estimating the conductivity inside the domain Ω . Unlike the forward problem, the inverse task is non-linear and difficult to solve, and it cannot produce an unambiguous result.

Electrical impedance tomography comprises two main submethods for the inverse solution: difference and absolute imaging. The former option reconstructs two different instances of measurement, each executed at either a particular time (time difference) or a modified frequency (frequency difference); selecting any of the scenarios then enables us to compute relative changes of the conductivity. The latter alternative, by comparison, utilizes only a single measurement [19].

Principally, the inverse task seeks a conductivity matrix that satisfies the conditions set out in equation 1.15, and it also maintains the voltage and current values in the domain Ω . In EIT, the problem is derived from the statement

$$\boldsymbol{\Psi}(\sigma) = \mathbf{A}^\dagger \mathbf{b}, \quad (1.28)$$

where $\boldsymbol{\Psi}(\sigma)$ is the conductivity change vector, \mathbf{A} denotes the system matrix (Jacobian), and \mathbf{b} represents the right-hand side vector (voltage error) [2].

After applying the Moore-Penrose inverse, we yield

$$\boldsymbol{\Psi}(\sigma) = \mathbf{A}^\dagger \mathbf{b} = (\mathbf{A}^T \mathbf{A})^{-1} \mathbf{A}^T \mathbf{b}, \quad (1.29)$$

leading to a solution that exploits the least squares method (LSM) in the generalized form; thus, we have

$$\boldsymbol{\Psi}(\sigma) = \min_{\mathbf{x}} \|\mathbf{A}\mathbf{x} - \mathbf{b}\|. \quad (1.30)$$

If the matrix \mathbf{A} is badly conditioned, the least squares method may fail when computing the inverse task, and no outcome is delivered. For this reason, the LSM utilizes complementary regularizations, of which the most significant ones are discussed on the final pages of this section.

In EIT, the objective function for the inverse task is mathematically defined as

$$\boldsymbol{\Psi}(\sigma) = \min \frac{1}{2} \sum \|\mathbf{U}_M - \mathbf{U}_{\text{FEM}}(\sigma)\|^2, \quad (1.31)$$

where \mathbf{U}_M is the vector of the voltages measured on the boundary, and $\mathbf{U}_{\text{FEM}}(\sigma)$ denotes the vector of the voltage values computed via the forward task. The choice of the norm defines the rate in suppressing sharp changes, as penalization with the L2 norm is more effective than its L1-based counterpart [10, 12].

In the image reconstruction process, the conductivity vector σ is sought with respect to minimizing the objective function $\Psi(\sigma)$. For the given conductivity vector σ , the algorithm reads

$$\sigma_{i+1} = \sigma_i - (\mathbf{J}_i^T \mathbf{J}_i)^{-1} \mathbf{J}_i^T (\mathbf{U}_M - \mathbf{U}_{\text{FEM}}(\sigma_i)), \quad (1.32)$$

where σ_{i+1} stands for a novel approximation of the conductivity vector, σ_i represents the conductivity vector computed in the previous iteration, and \mathbf{J}_i denotes the Jacobian expressing the sensitivity of the electrode potentials to changes in the conductivity vector at the relevant mesh elements [2, 12].

Applying the bare LSM to the inverse problem is insufficient, especially due to the actual ill-conditioning; thus, increasing the stability and convergence of the reconstruction requires a mathematical complement, namely, regularization. The best known regularization instruments, such as the Tikhonov, Laplace, and NOSER techniques, range among deterministic methods; in addition to these, however, there are also stochastic techniques, which utilize neural networks or genetic algorithms [11].

Tikhonov regularization

The Tikhonov technique embodies one of the first regularization approaches applied in inverse image reconstruction, and, importantly, it still remains a commonly employed tool. The general principles of this regularization procedure are characterized above, within objective function 1.31. In an expanded form, the method is defined as follows:

$$\Psi(\sigma) = \min \frac{1}{2} \sum \|\mathbf{U}_M - \mathbf{U}_{\text{FEM}}(\sigma)\|^2 + \alpha \|\mathbf{R}\sigma\|^2, \quad (1.33)$$

where \mathbf{U}_M stands for the vector of the voltages measured on the border of the domain Ω ; $\mathbf{U}_{\text{FEM}}(\sigma)$ represents the vector of the voltages on the electrodes, obtained with the forward solution; α is the regularization parameter; and \mathbf{R} denotes the regularization matrix [10, 20].

If we regularize the iterative algorithm from 1.32, the sought conductivity vector σ will take the following form:

$$\sigma_{i+1} = \sigma_i - (\mathbf{J}_i^T \mathbf{J}_i + \alpha \mathbf{R}^T \mathbf{R})^{-1} (\mathbf{J}_i^T (\mathbf{U}_M - \mathbf{U}_{\text{FEM}}(\sigma_i)) - \alpha \mathbf{R}^T \mathbf{R} \sigma_i). \quad (1.34)$$

The Jacobian characterizes the sensitivity of the potentials on the electrodes with respect to the conductivity changes at the given mesh element; we have

$$\mathbf{J}_i = \begin{bmatrix} \frac{\partial \mathbf{U}_1}{\partial \sigma_1} & \cdots & \frac{\partial \mathbf{U}_n}{\partial \sigma_1} \\ \vdots & \ddots & \vdots \\ \frac{\partial \mathbf{U}_1}{\partial \sigma_n} & \cdots & \frac{\partial \mathbf{U}_n}{\partial \sigma_n} \end{bmatrix}. \quad (1.35)$$

The stability and sensitivity features of the Tikhonov approach depend on the regularization parameter α and also on the initial conductivity value. Within the sequential processing, computing the Jacobian is the most time-consuming activity because the actual solution requires multiple results of the forward calculation [11, 20].

Total variation method

The total variation method (TVM) constitutes another deterministic approach to regularize the inverse task. In addition to effectively suppressing the noise, this instrument facilitates detection of sharp inhomogeneity contours in the simulated system. The technique's regularization term reads αTV_β and can be rewritten as

$$TV_\beta = \sum \sqrt{\|\mathbf{R}\sigma\|^2 + \beta}, \quad (1.36)$$

where \mathbf{R} denotes the regularization matrix expressing the relationship between neighboring elements of the mesh, and β is the parameter that characterizes the smoothness of the course of the objective function $\Psi(\sigma)$.

By extension, the TVM subsumes an alternative concept, the primal-dual interior-point method (PD-IPM). This subsidiary tool combines together two algorithms, namely, the lagged diffusivity and the Newton methods; function-wise, the former is used at the beginning of the image reconstruction to reach close to the final image, while the latter allows us to perform the remaining stages of the procedure [2, 10, 11].

Newton's one step error reconstructor (NOSER)

The NOSER-based regularization relies on calculating only one step of the image reconstruction, utilizing Newton's method. Such an approach usually finds use in difference imaging. This type of imaging comprises three stages, namely, obtaining the reference voltage U_{ref} , which corresponds to the conductivity σ_{ref} ; measuring the voltage to acquire the unknown conductivity distribution σ ; and reconstructing the conductivity difference to yield

$$\delta\sigma = \sigma - \sigma_{\text{ref}}. \quad (1.37)$$

The method also assumes the conductivity of an inhomogeneity to be markedly dissimilar from that of the medium inside the domain. In the reconstruction of the conductivity $\delta\sigma$ via difference imaging, we exploit the linearized model

$$\mathbf{U} \approx \mathbf{U}(\sigma_{\text{ref}}) + \mathbf{J}(\sigma - \sigma_{\text{ref}}) + e, \quad (1.38)$$

where $\mathbf{U}(\sigma_{\text{ref}})$ denotes the matrix of the voltage values obtained through the forward solution; \mathbf{J} indicates the Jacobian, i.e., the sensitivity matrix of the forward task, and this in turn is evaluated at the conductivity σ_{ref} ; and e stands for a randomly generated value expressing the noise [20, 21].

In difference imaging, the forward solution is substituted with measurement of the reference voltage \mathbf{U}_{ref} [20, 21], allowing us to modify equation 1.38 into

$$\mathbf{U} - \mathbf{U}_{\text{ref}} \approx \mathbf{J}(\sigma - \sigma_{\text{ref}}) + e. \quad (1.39)$$

Laplace method

Conceptually, the Laplace method consists in utilizing a high pass filter of the second order. As a rule, the technique operates in the form of an edge sensitive filter where a penalty term is computed for each element and its neighbors. The relevant regularization matrix is shown below, reading

$$\mathbf{R}_{ij} = \begin{cases} D + 1 & \text{if } i = j, \\ -1 & \text{if element } i \text{ is adjacent to } j, \\ 0 & \text{otherwise.} \end{cases} \quad (1.40)$$

The element itself is weighted by $D + 1$, with D representing the dimension of the model. Each neighboring element is assigned the weighting of -1; this leads to a zero sum in the penalty term in smooth images. The method can be characterized as an edge sensitive filter, although the actual classification depends on the *a priori* knowledge of the reconstructed conductivity distribution. If the *a priori* information is not available, the inverse imaging via this method induces noise amplification and decreases the stability of the solution [22].

1.4 Inverse problem: stochastic methods

This chapter briefly discusses the artificial neural networks and genetic algorithms for inverse imaging.

Artificial neural networks

Artificial neural networks (ANNs) constitute a stochastic tool that finds frequent use in EIT spatial conductivity reconstruction. Principally, a neural network relies on the excitation of neurons, a process identical with that which defines the functioning of a biological nervous system. Such a network embodies a novel algorithmic architecture (Fig. 1.3) enabling us to execute relevant basic functions, e.g., addition, multiplication, and Boolean logic operations to solve complex, ill-posed, and non-linear mathematical problems. An ANN has a simple computational and algorithmic

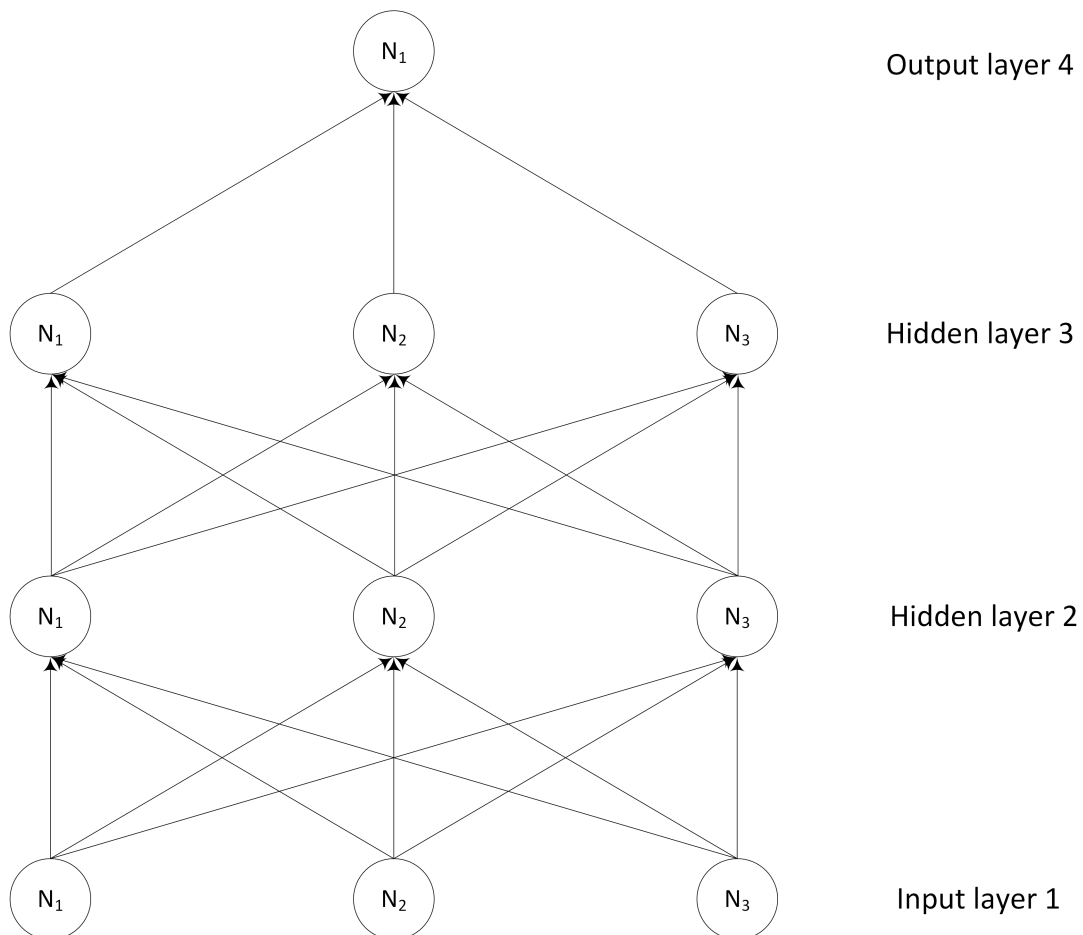


Fig. 1.3: A multilayer artificial neural network.

structure but requires a long and complicated procedure of prior learning. An optimal description and precise solution of a problem necessitate application of the

simplest ANN available. Generally, an ANN ensures a high level of parallelization to each neuron, i.e., network element [23, 24].

An ANN possesses a pre-defined number of input neurons, depending on the count of variables in the problem being solved. Each input neuron has a particular weight affecting the whole computation. There exist several types of activation and transition functions, which influence both the convergence of the problem and the learning of the ANN. An activation function is an output signal transferred to the neural network level; to name several examples, we can refer to the Heaviside step function and the linear, hyperbolic, and sigmoid activation functions [23].

The architecture of an ANN is topological, and the topology consists of individual layers. The smallest network constructible comprises one layer having one neuron; more complex architectures are then known as multilayer neural networks, and these enable EIT imaging. A multilayer network subsumes an input and an output layers, and several hidden ones. Each layer contains a pre-defined number of neurons, according to the target application. In recent years, diverse improvements and optimizations have been introduced into EIT neural networks, becoming a significant trend; one such tool is particle swarm optimization [25, 26].

A major methodological prerequisite for any successful use of a neural network rests in machine learning. The procedure cooperates with algorithms that evaluate the outputs in relation to weight changes, as these affect the results delivered by a network; the set of relevant algorithms includes, for instance, back projection and the dynamic neural network [24, 27].

As regards the two last-named instruments and their principal capabilities, we can choose back projection to present several functional details. Basically, this technique reviews and classifies the outcomes acquired from the output layer; these outcomes are generated by the flow of the applied inputs through the neural system. The values obtained via the classification are then sent back across the network, leading to an adjustment of the weights in each input neuron. The entire learning scheme continues running until the required accuracy is achieved [27, 28].

Genetic algorithms

Genetic algorithms (GAs) embody the alternative to the classic ANNs when an optimal solution of complex problems is desired. In terms of the componential stages, GAs involve population initialization, selection, crossover, and mutation. The structure of a GA is shown in the figure below.

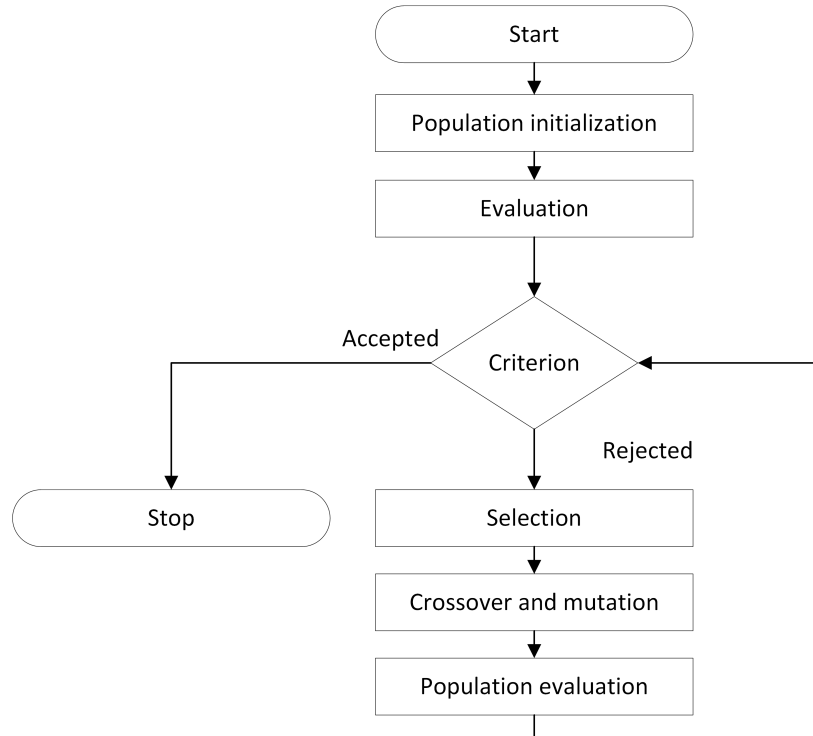


Fig. 1.4: A structural flowchart to illustrate a genetic algorithm.

As is obvious from the diagram, the individual phases are closely linked, and the actual execution unfolds as follows: Initially, a random population begins to be generated, and the eventual product is then subject to an evaluation that relies on correlating the results with the required function. In the next step, the convergence criterion is inspected. If this criterion is satisfied, the algorithm will stop operating; otherwise, a new population-making cycle will be launched, utilizing the crossover mechanism to adopt portions of the previous population. Afterwards, during the mutation phase, the properties and characteristics of randomly selected individuals are adjusted to allow the final stage, namely, evaluating the survivors and their fitness. The algorithm repeats until the criterion has been met [28, 29]. In EIT, various GAs are available, including modified variants and adaptive differential algorithms with a circular topology [30, 31, 32].

1.5 Inverse crime

The inverse task comprises certain ill-posed features that limit the algorithms and their capability of delivering accurate reconstruction as well as adequate noise suppression. In this context, let us note that the noise level is partially adjustable through the forward solver integrated in an algorithm: Such a solver allows us to test the inverse task via the procedurally easiest approach, where the forward output data are generated without noise to enable smooth recovery of the conductivity. The only difficulty rests in the *a priori* assumptions and precision of the floating-point arithmetic. To outline the purpose of the fundamental test, we can stress, above all, that it facilitates verifying the designed algorithm's performance and effectivity [1].

Using different meshes

Before solving a forward and an inverse tasks, we have to consider the fact that each of these requires a specifically configured mesh. This aspect, by extension, makes us realize that the relevant measurements can be performed and the desired experimental data obtained only with sufficiently precise equipment; under all other conditions, we need to rely solely on the simulated data from the forward task, thus obeying the most frequent scenario. This commonly applied option nevertheless requires us not to commit an *inverse crime* [33]. To obviate the issue, we can generate two separate original models, bearing in mind that the forward and the inverse variants are differentiable in factors such as the mesh density or element shape. The reconstructed conductivity should then be represented on the inverse model mesh; by contrast, the forward model mesh will likely remain unknown to the algorithm if the *a priori* information about the position of the inhomogeneity boundary was not employed [1, 34].

Simulation noise

The noise in the simulated data and the measurement error in the experiments proved to have a major impact on the reconstruction. In this connection, and within this subchapter, we can illustrate the inverse crime on a case where the researchers added Gaussian noise to the input data by applying a mathematically trained pseudo-random number generator and subsequently calibrated the device(s) or software(s) to reduce the systematic error in a manner that left only the random processes (discretization of measurement and thermal noise). Averaging the multiple measurements then ensured a good approximation of the data error corresponding to the output from the number generator; moreover, the approximation was characterized as sufficient by the central limit theorem. Such a scenario nevertheless occurs very rarely in real-world experiments. Real phantom vessels comprise many sources

of flaws that are difficult to suppress, e.g., contact impedance, motion artifacts, and variable surface geometry. Further, we will focus on the discretization error, whose simulation requires prior knowledge of the measurement setup. During the data acquisition stage, the signal is digitized in an ADC, which scales the input by using an amplifier. In the Sheffield-type adjacent pair drive system [35], the scale factor is defined by the position of the electrodes, allowing us to exploit the optimum range of the ADC. The multiple-drive system [36], by extension, relies on different strategies, and the values obtained via these strategies should ideally comprise noise uniformly distributed and scaled to the measured data. Generally, in the discussed context, a frequent flaw rests in an insufficient description of the simulated noise level [1, 34].

Pseudo-random numbers

These sets of values involve two main negatives (and related precautionary steps) that may influence the outcomes. First, we have to consider the undesired impacts of using a pseudo-random number generator, as some of these softwares generate one and the same sequence of mock random numbers after each start of the program. Second, there appears the need to avoid assigning pseudo-random numbers the role of errors. Such a goal can be achieved by, for instance, generating a sequence of numbers to run a reconstruction and to determine its mean error and variance; the parameters are then evaluated also in the data fitting. Due to the non-linear character of an EIT inversion, introducing Gaussian error in the data will not yield any Gaussian reconstruction error, and the overall distribution of errors has to be applied, with the assumption that small noise levels will be linearly approximable. In practice, mock random numbers can produce an outlier that the experimenter might reveal via comparing the reconstruction error and its data counterpart. Such a possibility then most plausibly explains why some experimenters manage to sidestep the inverse crime while avoiding the use of pseudo-random numbers as a source of flaws [1, 34].

Additional tuning of the process

The tuning is performable via “tweaking” the reconstruction parameters, including the number of iterations, smoothing level, constraints, and small variations in the algorithm. This approach stands in contrast with the regular scheme, where we can either acquire the value (e.g., a hyperparameter, retrievable by using the L -curve) and estimate the data error (Morozov’s stopping criterion) or repeatedly simulate and measure various conductivities to seek the parameters that might deliver acceptable results. In terms of the tuning, the classic inverse crime, as compared to a standard research case based on original data, rests in training a neural network and then conducting an experiment designed around the training set. To provide an-

other convenient example, we can refer to testing an algorithm on an already known scenario involving a circular inhomogeneity which has not been verified by means of complex anomalies with varying contrasts. The best way to obviate the “tweaking” is to employ a blind sample when acquiring the simulated and the experimental data [34].

A revision of the entire chapter will lead us to conclude that the inverse crime takes the following forms [1]:

- using one and the same forward model in both simulating the data and executing the reconstruction;
- not adding simulated noise to the synthetic data;
- showcasing the reconstruction of a few special cases that produced reliable results and claiming these to represent the general performance;
- tuning the reconstruction parameters manually, using prior knowledge of the correct answer, and not presenting any blind trials, where the parameters cannot be “tweaked” (e.g., teaching a neural network by utilizing solely a training set).

1.6 Measurement strategies: current patterns

In EIT, the data acquisition mode depends on the system of electrodes and the adopted feeding method. By a narrower definition, this chapter presents the most common current patterns, all classifiable into two main groups indicating whether the target application is in an open or a closed domain.

The closed domain is defined as a system with electrodes placed equidistantly on the boundary. Such a setup can be fed via diverse strategies, a very traditional one being the adjacent stimulation pattern (ASP). Here, the principle lies in injecting a current into two neighboring electrodes while leaving the others to carry out the voltage sensing. Thus, the feeding and the measuring electrodes shift along the boundary to cover all combinations possible, Fig. 1.5. The number of values measured in a 16-electrode system reaches 208; however, the count of independent voltage values obtainable with the ASP is only 104, due to a redundancy of the electrode pairs [10, 13, 37].

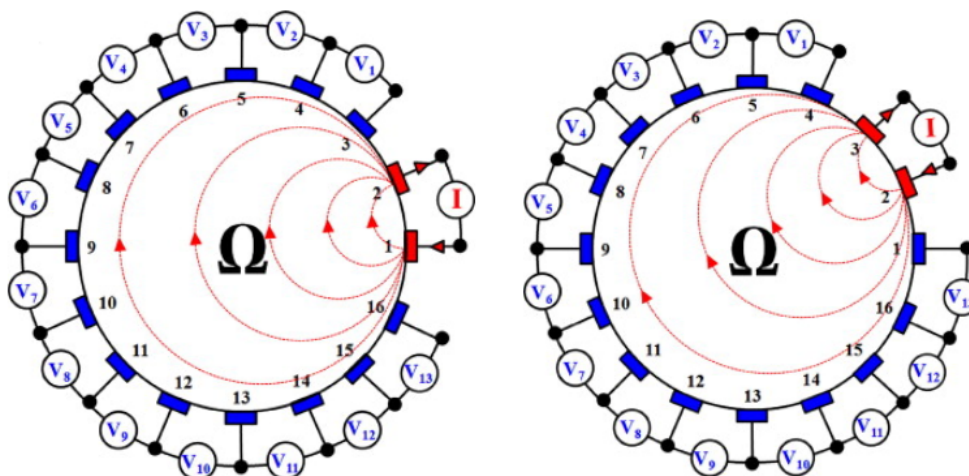


Fig. 1.5: The adjacent stimulation pattern [37].

Another current driving option for the closed domain is embodied in the opposite stimulation pattern (OSP). Procedurally and configuration-wise, the technique installs the feeding electrodes on the opposite side, using the others to conduct the measurement. When the first sequence ends, the current source moves to the next pair, and the measurement protocol repeats (Fig. 1.6). The procedure provides 104 independent voltage values in total [10, 37].

In addition to the ASP and the OSP, the means available comprise Skip-X patterns, where a selected number of electrodes X is skipped between the current-carrying electrodes. This strategy combines the features of the opposite and the adjacent ones, and its best known variant is Skip-4.

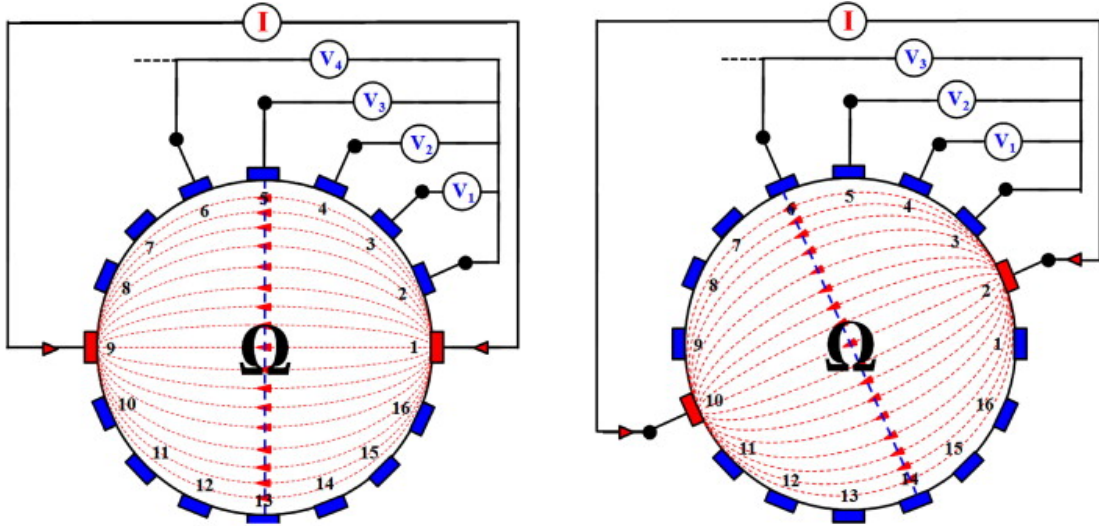


Fig. 1.6: The opposite stimulation pattern [37].

To complement the single-source methods, experts in the field have designed multi-source driving, namely, the trigonometric stimulation pattern, which relies on multiple independent sources capable of creating a homogeneous current density inside the investigated domain. Measurement is performed on all of the electrodes, Fig. 1.7; generally, the pattern allows us to obtain 120 independent voltage values in a 16-electrode system. The strategy has not found wide application, due to a number of independent current sources [10, 37].

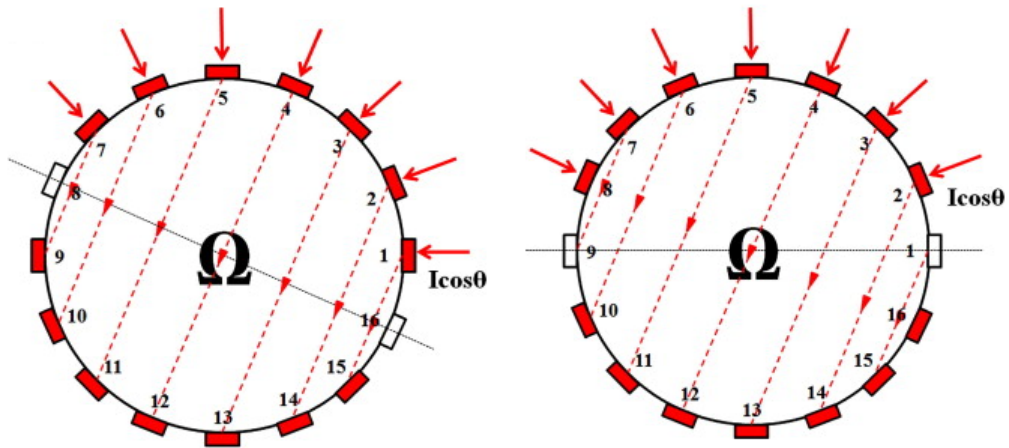


Fig. 1.7: Trigonometric driving [37].

Working with open domains is then facilitated by a different set of techniques, as presented below. First of all, let us note that the open domain is a system having infinitely approximable boundaries. This property can be demonstrated on geophysical measurement, in which the electrodes are pinned to the ground equidistantly in

a line or a matrix but the first and the last electrode do not neighbor on each other.

Open domain patterns are often exemplified through Wenner driving, a strategy that exploits dipole-dipole feeding and measurement, utilizing also a gradual movement and an increasing distance (value a in Fig. 1.8) between the electrodes to secure the possibility of underground mapping [13, 38].

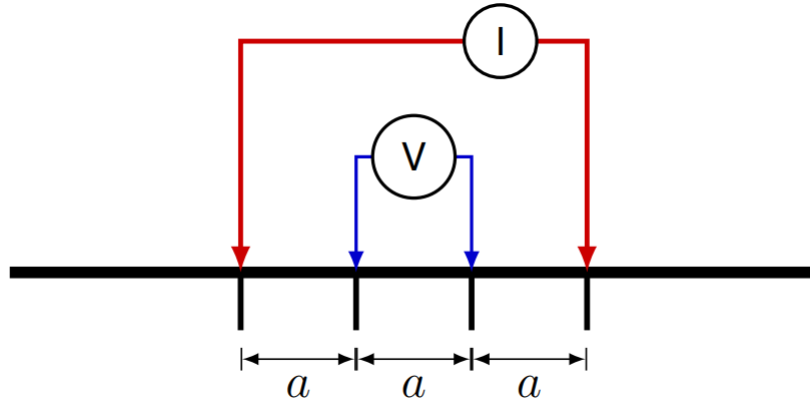


Fig. 1.8: The Wenner scheme-based arrangement [13].

An alternative approach is embodied in the Schlumberger method. Being a modified Wenner pattern, the concept shares some of its predecessor's features, such as the dipole-dipole feeding and measurement. Naturally, however, there are also major differences, including the fact that Schlumberger driving relies on symmetrical and non-equidistant electrode placement (Fig. 1.9). If an equidistant configuration is employed, the Schlumberger concept passes into the original Wenner scheme [13, 38].

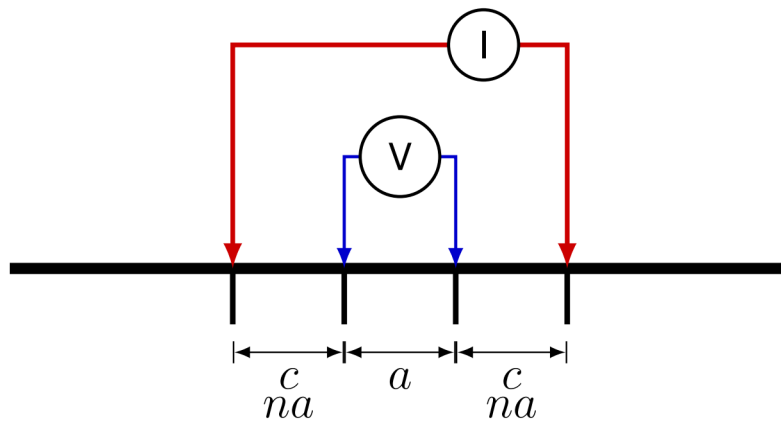


Fig. 1.9: The Schlumberger approach in use [13].

Various feeding and measuring combinations in the Wenner and the Schlumberger techniques are introduced in the tables below. The letters A and B represent the current-carrying electrodes, whereas M and N denote the measuring ones. In

Schlumberger driving, the sequence between the first and the twelfth measurements remains the same; Tab. 1.2 thus begins with the thirteenth cycle [13].

Tab. 1.1: The Wenner measurement sequence.

Wenner												
Measurement	1	2	3	4	5	6	7	8	9	10	11	12
A	1	2	3	4	5	6	7	1	2	3	4	1
B	4	5	6	7	8	9	10	7	8	9	10	10
M	2	3	4	5	6	7	8	3	4	5	6	4
N	3	4	5	6	7	8	9	5	6	7	8	7

Tab. 1.2: The Schlumberger measurement sequence.

Schlumberger										
Measurement	13	14	15	16	17	18	19	20	21	
A	1	2	3	4	5	1	2	3	1	
B	6	7	8	9	10	8	9	10	10	
M	3	4	5	6	7	4	5	6	5	
N	4	5	6	7	8	5	6	7	6	

Other data acquisition patterns relating to the open and the closed domains are discussed in references [13, 38].

1.7 EIDORS library

The above-characterized numerical tools for EIT image reconstruction are implemented within several libraries, among which EIDORS (Electrical Impedance Tomography and Diffuse Optical Tomography Reconstruction Software) stands out as a most common choice. Developed by Andy Adler, William R. B. Lionheart, Nick Polydores, and other specialists, the library is executable in Matlab or Octave and provides forward and inverse solvers [22].

The forward task is computed via the FEM, while the inverse problem can be resolved through absolute of difference reconstruction. The library contains a variety of algorithms, such as the Gauss-Newton, conjugate gradient, GREIT (the Graz Consensus Reconstruction Algorithm for EIT), back projection, and Kalman filter methods, all facilitating dynamic imaging [22, 39].

Besides inverse techniques, various regularization options are available, including, for instance, the Tikhonov, Laplace, NOSER, and total variation-based ones. The library also offers a function to support domain triangulations and to deliver pre-defined FEM models in biomedicine or industry (Fig. 1.10) [22, 39], where displaying the thorax or the head in 3D and circular objects in 2D is desired. EIDORS cooperates with several mesh generators, in particular Distmesh (2D), Netgen (2D/3D), and GMSH (3D).

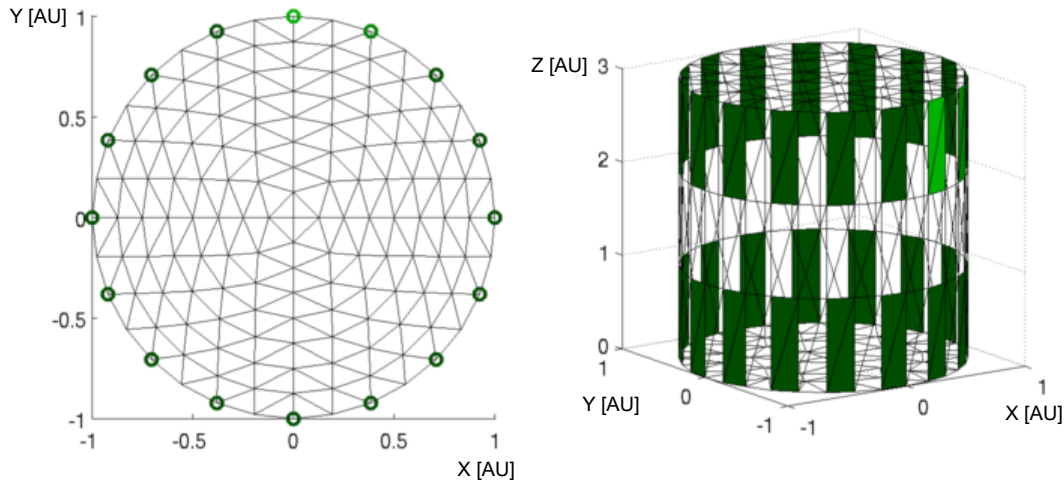


Fig. 1.10: Sample FEM-based models with inserted electrodes: A 2D and a 3D domains generated via Distmesh and Netgen, respectively [39].

In the figure above, the left-hand sector shows the mesh of a 2D domain containing 16 equidistantly distributed point electrodes, and the right-hand zone introduces a 3D model comprising two levels of rectangular electrodes; the first of these electrodes is highlighted in light green.

To present further details, Fig. 1.11 visualizes sample FEM meshes. The smooth model on the left-hand side comprises electrodes, the initial conductivity, and an inhomogeneity, while the coarse one in the right-hand area defines a reconstruction scenario where the conductivity distribution was evaluated from the initial layout.

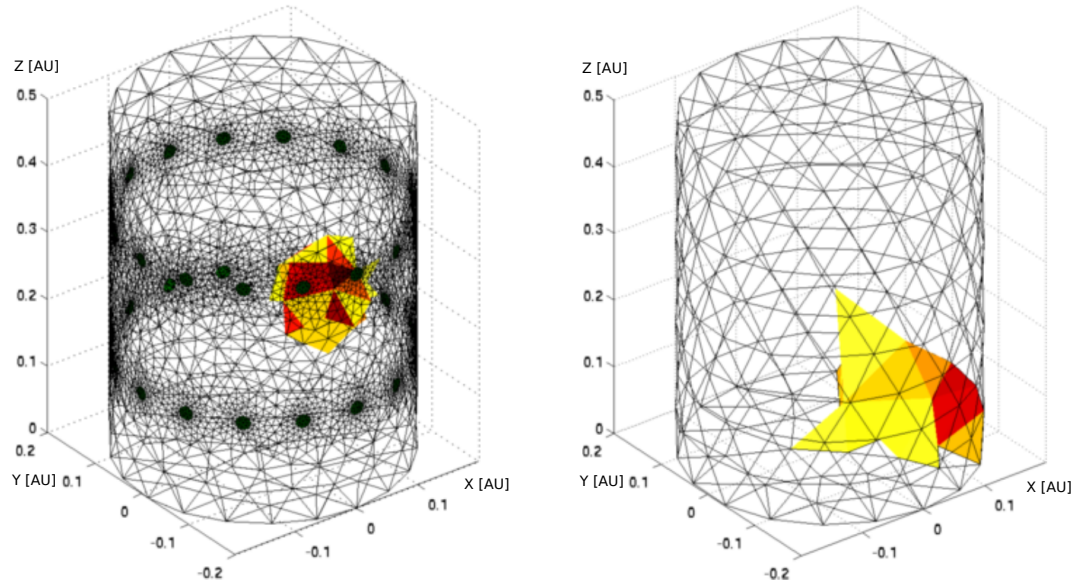


Fig. 1.11: The initial model with an inserted inhomogeneity (left) and the reconstructed conductivity distribution (right) [39].

1.8 Domain meshing

This chapter outlines diverse methods for domain meshing in geophysical applications. To start the discussion, we can point out that most of the domains that serve EIT imaging exploit simple 2D models involving mesh refinement around the electrodes. Another relevant effect, namely, domain extension⁴, is visualized in Fig. 1.12.

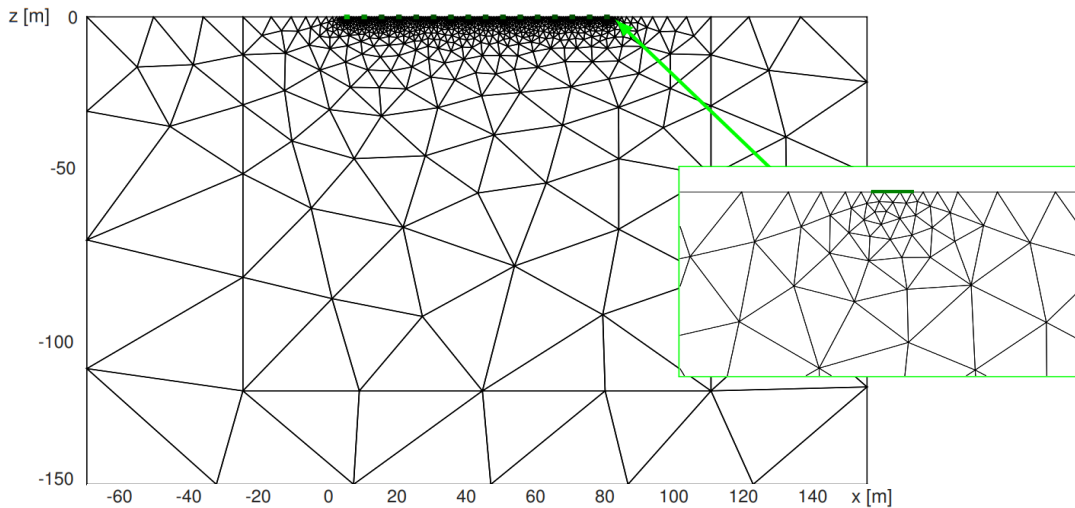


Fig. 1.12: An extended 2D mesh of a geophysical domain [13].

The extension provides additional elements affected by diffusion; these, however, are placed rather far from the investigated area. As a result, the diffusion has a negligible impact within the examined space. In the given context, it might be useful to illustrate the usability of 3D modeling instead of the standard 2D approach; we therefore propose the water dam domain in Fig. 1.13 as a convenient example [7].

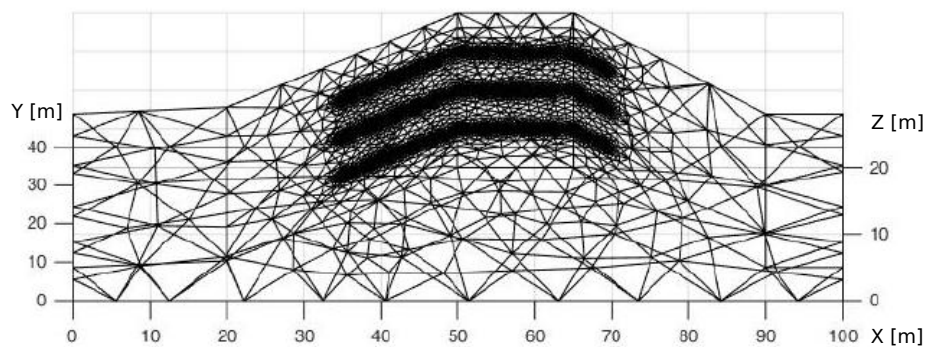


Fig. 1.13: A simple 3D domain to allow water dam imaging [7].

⁴The domain is extended due to the diffusion accompanying the actual solution.

By contrast, more complex models are employed very rarely in image reconstruction [8, 40]; the reasons lie in the ill-posedness of the inverse problem, requiring precise meshes, and the high number of elements, causing a rapid rise in the computational cost. An inaccurate domain mesh can produce an error greater than those of the reconstruction-based numerical solution and the related measurement uncertainty combined together.

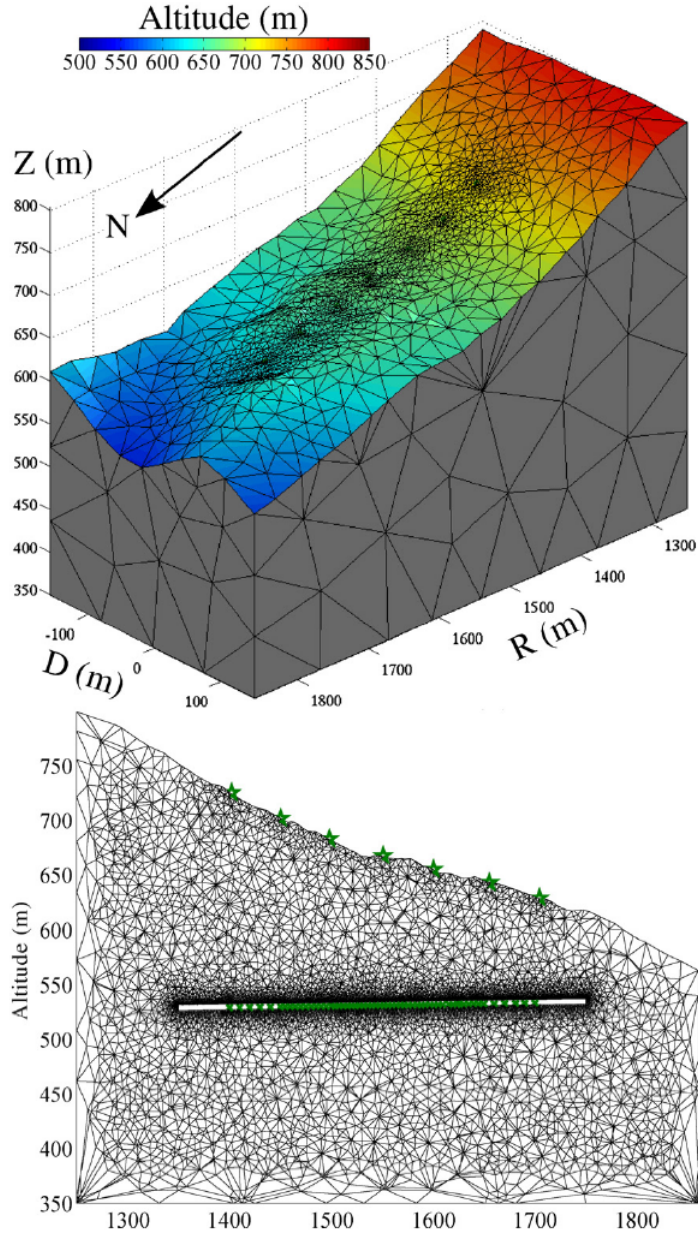


Fig. 1.14: A complex geophysical 3D domain for ERT imaging [40].

Generating the meshes displayed in Fig. 1.14 exploits algorithms that enable geophysical surface mapping. To supply relevant details, the top image displays an

experimentally made, Netgen and GMSH-generated complex 3D mesh comprising electrodes, and the bottom one presents a cross-section of the domain on which the conductivity is reconstructed. In the latter mesh, the electrodes are represented as points to ensure correctly proportional dimensions. Advantageously, sophisticated 3D models are often converted into 2D ones during the reconstruction to reduce both the complexity of the solution and the time cost [8, 40].

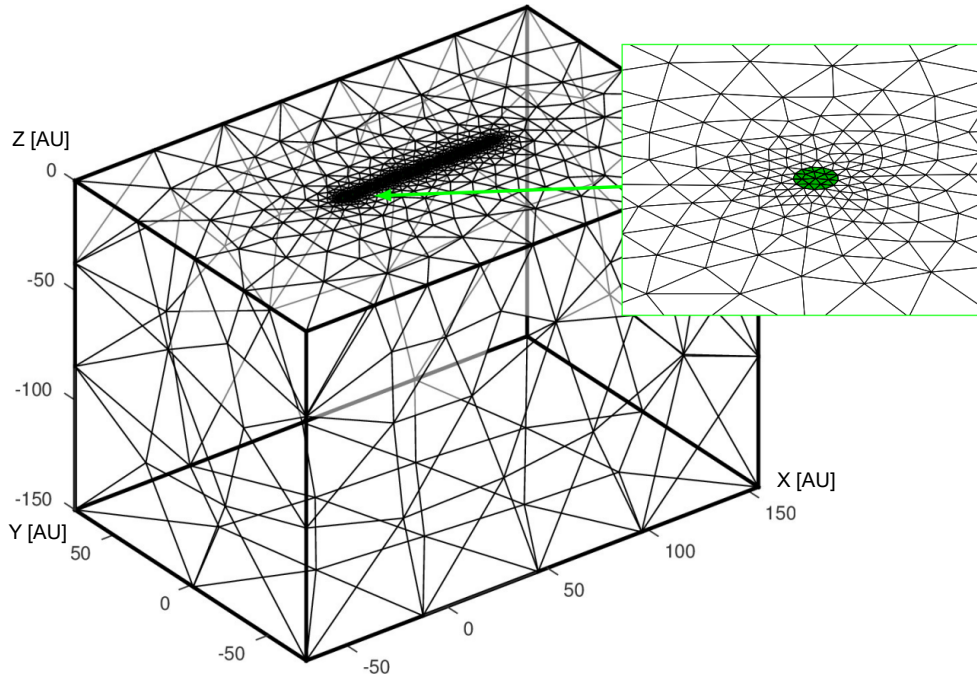


Fig. 1.15: An image reconstruction domain generated with EIDORS [13].

Returning to mesh refinement, we can now refer to Fig. 1.15 and the region near the surface of the electrodes. The effect observable on the top plane of the object in the upper image renders the inversion more precise; however, the surface electrode does not suit real-world geophysical survey, where the electrodes are burrowed in the ground. In practice, an electrode convenient for the purpose is manufactured in a single piece or can be assembled from multiple components, namely, smaller vertical electrodes that interfere with the domain [7, 13].

In EIT imaging research, domain meshing is matched in importance by resolving the Jacobian [13] as an instrument to correct the solution with respect to the movement of the electrodes. To demonstrate this, the authors of the referenced article performed operations such as evaluating artifacts which occur through electrode bending. Other interesting subprovinces are, for instance, reconstruction in $2\frac{1}{2}$ D space to reduce the memory requirements [18] or evaluation of inverse image artifacts arising from the actual forward task (Fig. 1.16) [41].

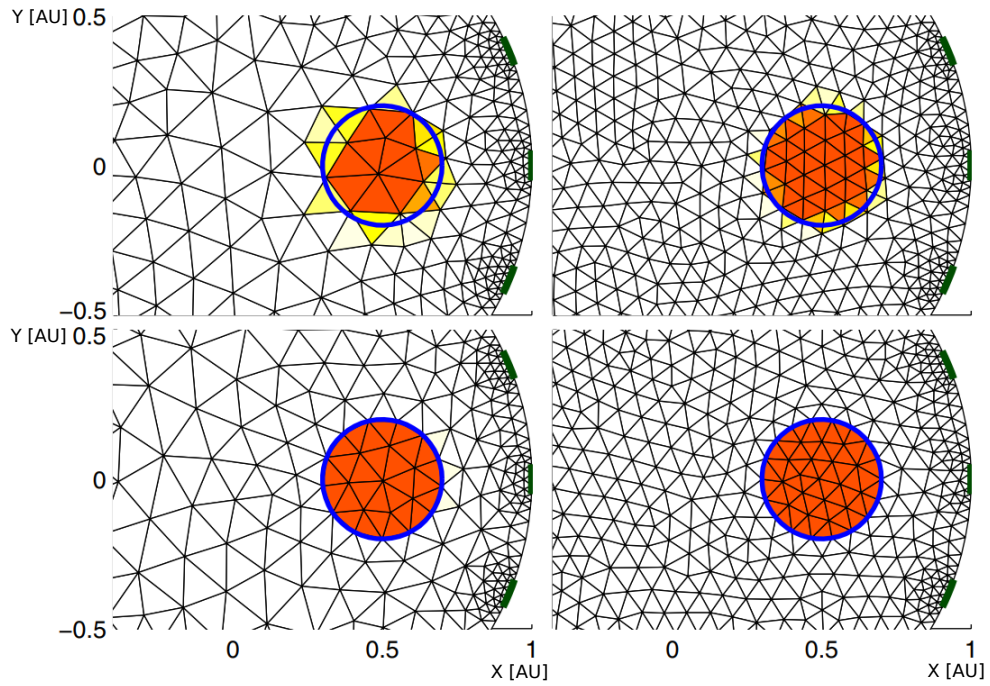


Fig. 1.16: The impact of precise inhomogeneity meshing [41].

An initial conductivity distribution discretized via a mesh is shown in Fig. 1.16. The precision of the domain model comprises also the precision of the inhomogeneity shape, as is shown in the top left object. Refining the mesh and specifying the border and shape correspondingly to the inhomogeneity enhance the quality of the final solution; conversely, each inaccuracy produced by the forward model affects the results of the forward and the inverse tasks [41].

1.9 Complete electrode model parameters

The number of parameters accurately estimable during a reconstruction cycle is small, due to the ill-posedness of the inverse problem and the increased computational cost. Thus, the individual parameters can be evaluated through an *a priori* operation, using a forward solver together with a clearly defined physical and numerical model. Further, optimizing each domain parameter before launching the image reconstruction brings an advantage for the subsequent non-linear inverse ill-posed task. The parameters that affect the inverse imaging include boundary deformation, inaccurate electrode placement, imprecise electrode surface, and contact impedance; their character and impact on the reconstructed image are briefly described below.

The first item on the list, an imperfect boundary shape, influences the potential on the electrodes significantly, even more than inhomogeneities. To expose this effect, let us have an elliptically or otherwise deformed circular domain, where the distortion leads to marked changes in the product of the forward task. In concrete terms, the faulty boundary can result in image blurring, incorrect localization, and wrong recognition of an inhomogeneity. Viewing the issue from the perspective of data acquisition then shows that the boundary deformation causes more imaging errors in the single-source patterns (ASP, OSP, and Skip-X) than in trigonometric driving [42].

Next let us focus on electrode misplacement, another major source of incorrect imaging that arises from an inaccurate model. In difference imaging, such flawed positioning does not generate artifacts, because the errors are subtracted from two identical mesh designs. By contrast, the misplacement significantly affects the static reconstruction, rendering the image very sensitive to this type of modeling fault. Placing an electrode imprecisely may introduce an error greater than that produced through all uncertainties given by the measurement system. The mismodeling eventually causes image blurring, wrong recognition of an inhomogeneity, and artifacts, i.e., difficulties of which some were already noted above. These spurious effects are suppressible by strong regularization; the procedure, however, materializes at the cost of losing information about the absolute conductivity value. The impact of the misplacement is generally more prominent in the single-source patterns than in trigonometric driving [42].

Another one of the important domain model parameters rests in an inaccurate electrode surface. The actual role of such a surface in the imaging depends on the applied current pattern. Single source driving is overall not sensitive to electrode mismodeling, as the measuring electrodes conduct a low-level current, stemming from the high impedance of the amplifier. In the trigonometric pattern, by comparison, any small change on the surface has a marked influence upon the imaging,

mainly due to the induced ring artifacts. At this point, we can also stress that the surface mismodeling error is inversely proportional to that generated by an incorrect contact impedance value [42].

Regarding the above-outlined set of adverse factors, the last item to be discussed is contact impedance. This effect remains negligible in single-source patterns, thanks to the level of the current being kept low by the high impedance of the amplifier; the exception lies with the feeding pair of electrodes, where the measured potential is affected by the contact impedance and, at the same time, the current injected from the source. In the trigonometric pattern, the contact impedance exerts a serious impact on the measurement, owing to the current-carrying electrodes; such a condition then produces image blurring and ring artifacts [42].

The domain parameters and current distributions as related to the stimulation patterns [43] are summarized in the table below.

Tab. 1.3: Comparing the stimulation patterns in terms of the individual parameters and current injection requirements [42, 43].

Parameter	Adjacent	Opposite	Trigonometric
Sensitivity at domain boundary	✓	✗	✓
Sensitivity in the middle of the domain	✗	✓	✓
Required VCCS output voltage	Lower	Higher	Higher
Sensitivity to electrode position	High	High	Mid
Impact of contact impedance	Negligible	Negligible	High
Sensitivity to domain shape	High	High	Mid
Sensitivity to electrode surface	Low	Low	High
Electrode noise interference	High	High	Low
Uniform current density	✗	✗	✓
Signal to noise ratio	Low	Low	High
Multiple current sources	✗	✗	✓

As is shown, the measurement results reflect diverse effects, of which some are suppressible via a convenient choice of the current pattern.

1.10 Approaches to solving the domain parameters

In the real-world environment, most of the individual parameters are unknown; some, however, can be directly measured or computed before or during the image reconstruction. The concepts currently available for evaluating the domain parameters are outlined below, through a selective insight into major research subtopics and outcomes relevant to this particular segment of the field.

The compensation of skin contact impedance was studied in article [44], whose authors compared the two- and four-electrode methods, designing a three measurement technique to carry out the compensation. Generally, the aim of the project lay in determining the contact impedance and suppressing its impact via a novel construction of the electrodes. To reach the desired result, the researchers fabricated compound electrodes, in which the feeding and the sensing components operate separately within one compact unit (Fig. 1.17). The electrodes were built according to the four-electrode method and then successfully verified.

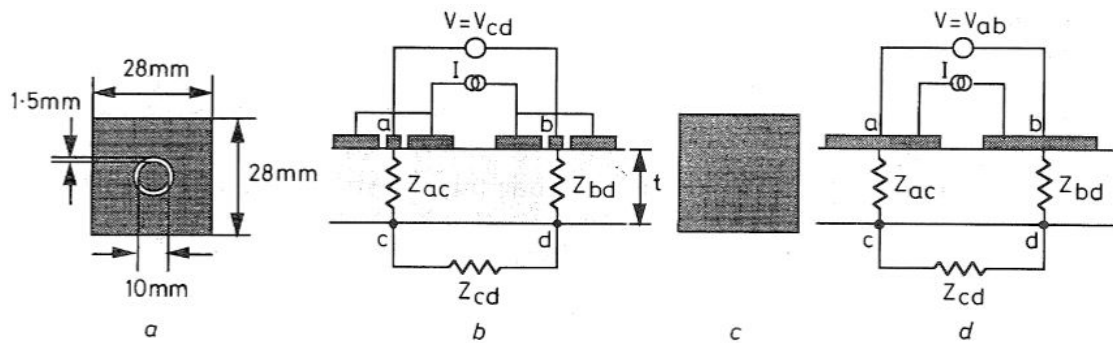


Fig. 1.17: The design and equivalent diagrams of a compound (a,b) and a simple (c,d) electrodes [44].

The effect of unknown contact impedance was further investigated in sources [45, 46], with a focus on the possibility of estimating the impedance by utilizing the CEM. The proposed procedure was compared with a measurement involving an Oxford Brookes (OXBACT) and a Kuopio impedance (KIT 4) tomographs. The distribution of the conductivity and contact impedance was reconstructed via real data within five different experiments. The results showed that the two quantities are, as a rule, inseparable and cannot be estimated without a measurement using a uniform conductive medium.

The unknown boundaries and contact impedance in relation to clinical applications were examined in article [47], which discussed these issues as a potential source of systematic errors during the reconstruction. The authors' novel approach allowed challenging the inaccuracies numerically to successfully reduce the errors (Fig. 1.18).

In procedural terms, interestingly, the original image was based on a measurement, but the deformation was only simulated.

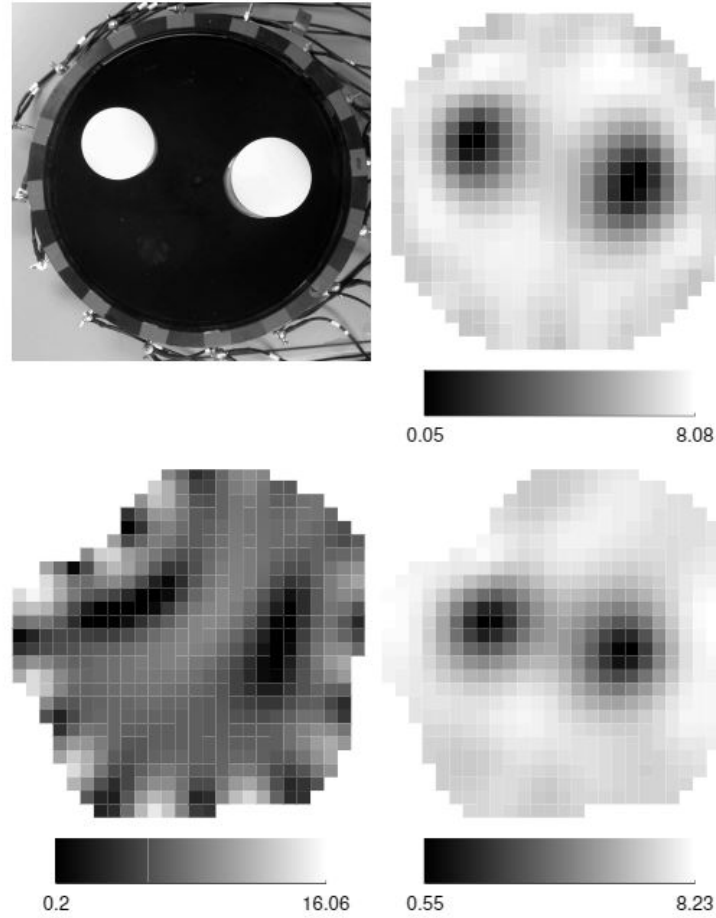

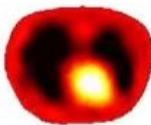
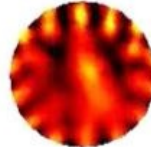
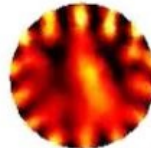
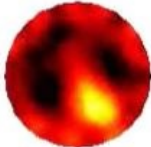
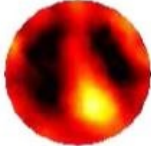


Fig. 1.18: Top left: The measurement setup. Top right: Reconstructing the isotropic conductivity. Bottom left: Reconstructing the isotropic conductivity by using an incorrect model. Bottom right: The uniformly anisotropic conductivity in a deformed domain. The displayed quantity is η [AU] [47].

A method for compensating variable electrode contact was introduced through a Boverman et al. article of 2009 [48]. The researchers developed a hybrid nonlinear-linear reconstruction algorithm, utilizing the CEM; the algorithm exploited the Levenberg-Marquardt optimization with analytical computation of the Jacobian matrix. In terms of overall capabilities, the procedure indicates and significantly reduces artifacts caused by poor contact. The functional testing was performed on a set of clinical data.

Another technique to reduce the modeling error associated with unknown domain boundaries was characterized in reference [49]. Generally, the concept exploits the Bayesian approximation error approach and is applicable to problems that arise from

coarse discretization or domain truncation. Regarding the experiment, the image reconstruction using original and mapped models at unknown domain boundaries took 14 to 210 seconds in 2D models (Fig. 1.19) and 65 to 383 seconds in 3D meshes. The results showed that the method ensures efficient compensation, and this outcome was also verified through an experimental measurement with a KIT 4.

Estimate	Forward model	Reconstruction	Δ_σ	N_n	CPU time
Actual conductivity (arbitrary units)					
Lungs = 1.2 Background = 2 Heart = 3.6					
MAP-CEM	$U_\delta(\bar{\sigma}, \gamma)$		11.01	4818	210 s
MAP-CEM	$U_\delta(\sigma, \tilde{\gamma})$		34.52	1596	47 s
MAP-CEM	$U_h(\sigma, \tilde{\gamma})$		36.62	551	17 s
MAP-AEM	$U_\delta(\sigma, \tilde{\gamma})$		19.67	1596	45 s
MAP-AEM	$U_h(\sigma, \tilde{\gamma})$		19.56	551	14 s




Fig. 1.19: Various MAP estimates with simulated data; Δ_σ denotes the relative errors, and N_n represents the number of nodes in the mesh [49].

An innovative scheme for optimizing the electrode position based on different domain shapes was devised by Dardé et al. [50]. The method allowed fine-tuning the electrodes, involving the localization and surface problems. To tackle the imperfect nature of the electrode information, the authors utilized the Fréchet derivative of the CEM, incorporating it into the output of the least squares method. The proposed modification of the Newton-type reconstruction algorithm facilitated reconstructing simultaneously the conductivity distribution and electrode locations. The overall feasibility was verified on a two-dimensional domain.

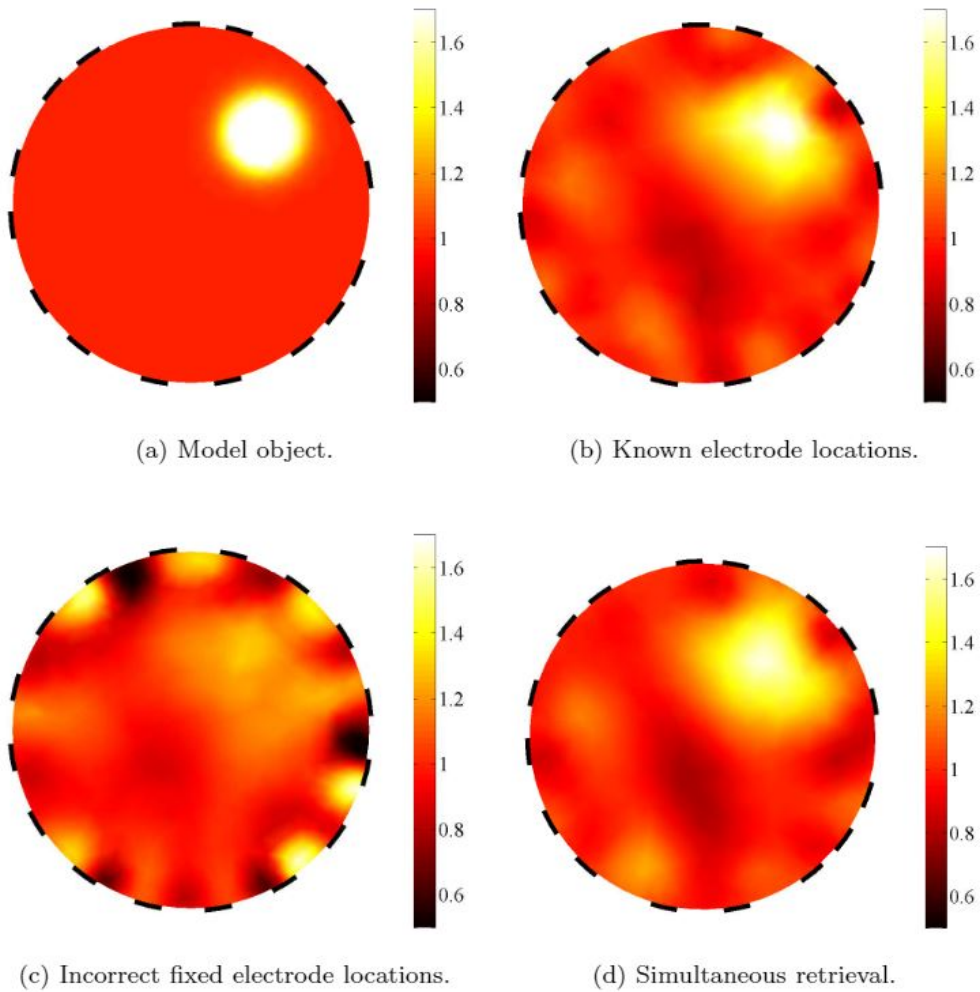


Fig. 1.20: The concurrently reconstructed conductivity distribution and electrode location, as compared with the fixed placement [50].

A fast and simultaneous statistical estimation of the conductivity and electrode contact impedances in a 2D disc was formulated within a 2011 article by Demidenko et al. [51]. The method exploited Toeplitz matrices to identify bad contact, employing a Toeplitz matrix as a Neumann-to-Dirichlet map in linearizing via the gapZ

model. The technique performed successfully and was validated via an experimental measurement on a homogeneous vessel. After that, the experts applied their concept in an estimation of contact impedance in breast, relying on Dartmouth EIT hardware.

Various electrode placement options were studied in a Hyvonen et al. article of 2014 [52]. The researchers proposed an optimality criterion derived from the Bayesian approach, approximating the posterior density of the conductivity localization by linearizing the current-to-voltage map of the CEM. The discussed optimization algorithm was of the steepest descent type. Based on the Fréchet derivatives of the CEM, the electrode locations were numerically simulated (Fig. 1.21). The optimization process was evaluated on a homogeneous conductivity distribution, with white noise added. The method is suitable for circular and irregular boundary shapes.

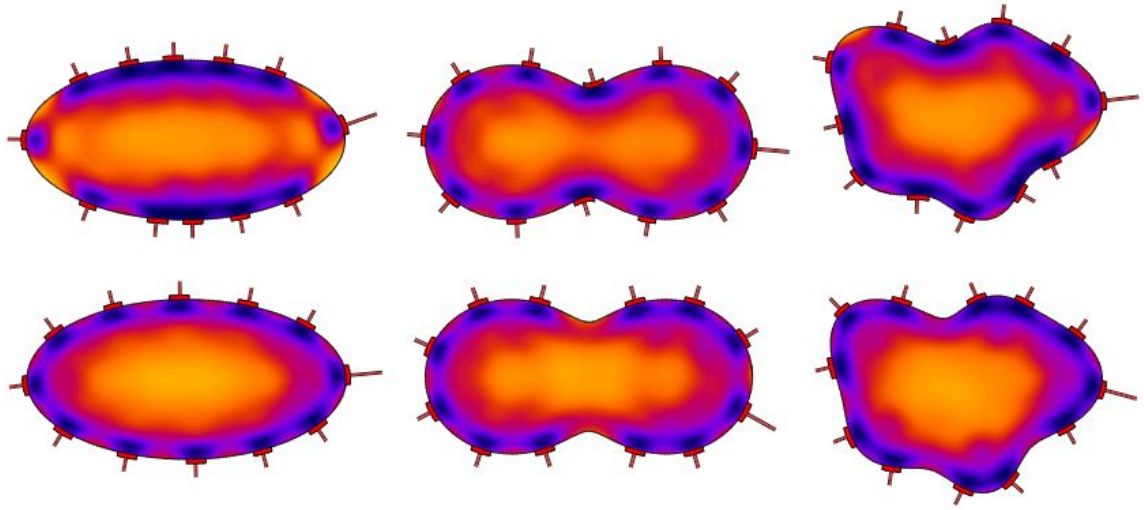


Fig. 1.21: The electrode placement computed through the Bayesian approach, utilizing Fréchet derivatives for non-circular shapes [52].

A further research on imprecise electrode modeling, electrode movement artifacts, and surface movement reconstruction was detailed in source [13], whose author, A. J. S. Boyle, carried out simulations to compare the compensation procedures (naïve, minimal, rank-one update perturbation, and Fréchet derivative) via EIDORS library. As regards the perturbation method, the results were unstable at small contact impedances, depending on the perturbation magnitude. The Fréchet derivative approach proved inappropriate at such impedances and exhibited a sensitivity to coarse meshes. The Fréchet derivative and the rank-one update techniques are very fast and computationally effective. In addition to comparing the compensation methods, Boyle performed a concurrent reconstruction of the resistivity and

surface movement on an open domain and discussed the limitations of the process. The applied solution was verified by using real and reproduced data sets.

A simultaneous reconstruction of time-varying images and contact impedances was outlined in article [53], including an algorithm designed via general singular value decomposition and a dual-mesh FEM framework to allow real-time reconstruction of the contact impedance and the admittivity image. This concept led to an effective suppression of artifacts due to electrode drift and motion. After being evaluated, the method was verified on reconstructed (clinical) data acquired with a GE GENESIS system.

Another procedure for optimizing the electrode position was introduced by Smyl and Liu [54], who employed an artificial neural network to resolve electrode misplacement, exploiting EIDORS. The algorithm was validated by means of noisy simulated voltage measurements (Fig. 1.22).

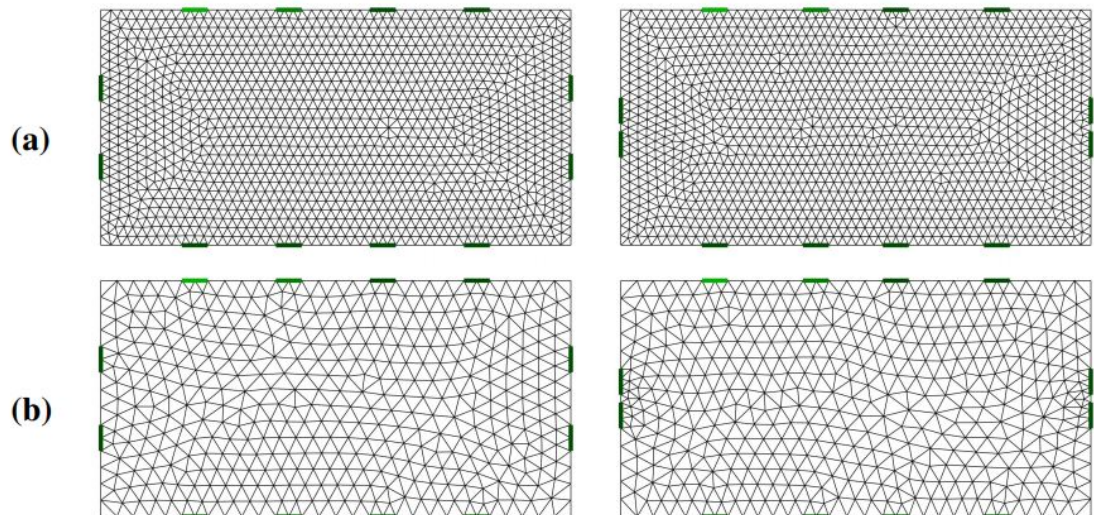


Fig. 1.22: Optimizing the electrode placement with a neural network [54].

Considering the above research projects and outcomes, we prepared optimization with genetic algorithms to resolve the boundary inaccuracies, ensure a precise electrode placement, and compute the initial conductivity before the actual reconstruction.

1.11 Algorithm parallelization

The parallel processing of algorithms embodies a most important field of interest within EIT inverse imaging. Various reconstruction algorithms are contained in EIDORS library, which has frequently been used as the reference to compare diverse results and is characterized in subsection 1.7 hereabove. The library has also constituted a basis for creating sets of parallel processing algorithms. One of the instruments in this group is SuperSolver, an algorithm comprising preconditions and enabling effective computation. A precondition denotes a transformation or relates to including special conditions in a given problem to simplify the calculations executed through numerical methods. The increasing mesh complexity and rising amounts of elements make users employ a sparse matrix format to reduce the memory requirements. In a parallel computation of the Jacobian, PARDISO library can prove useful, yielding a considerable speed increase via graphical processor units [55, 56, 57, 58].

A further algorithm to perform parallel EIT image reconstruction is PEITS (Parallel EIT Software). This instrument stems from the Dune, a C++ based tool for solving partial differential equations; the Dune ensures mesh discretization to execute parallel processing. Besides PEITS, options such as PETSc are available for the processing; PETSc, by definition, is a set of algorithm extensions containing preconditioning and transformations [59].

Domain discretization-based parallel processing consists in dividing the mesh into elements, of which each has its own nodes. The elements comprise an item on the border and another one on the boundary; this means that, for N elements, N nodes and N boundaries are created in the unified diagram, delivering the requirements for the parallel processing. Assigning weights to each element guarantees that an overall stability of the solution is gradually achieved [57, 59].

To curb the computational intensity in EIT image reconstruction, users often rely on transformations, such as the transformation into a multilayer network. Here, two main options stand out: a geometrical and an algebraic multilayer network. The former alternative needs a uniform mesh to produce the solution; this prerequisite, however, is unavailable in many deformations and irregular shapes. Compared to a geometrical network, the algebraic type allows calculation also with irregular meshes [57, 59].

1.12 Instrumentation and devices

This subsection outlines the general structure of an EIT system, introducing the main components through the block diagram in Fig. 1.23 and the related explanation. Incorporated in the discussion is also an insight into presently available data acquisition units that facilitate a fundamental portion of EIT processes [60, 61].

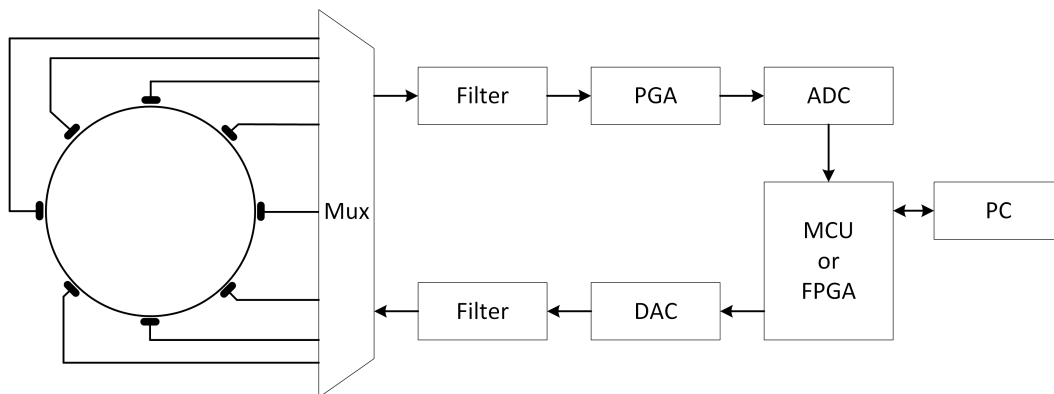


Fig. 1.23: The elements forming an EIT data acquisition system.

An EIT system is generally constructed around a microcontroller or an FPGA, whose central task rests in communicating with a PC, generating an injection signal, and collecting data from an ADC. The feeding segment comprises a DDS and a DAC, both usually connected to a voltage to current controlled source (VCCS). The VCCS delivers a constant AC current, injecting it to the tomograph electrodes through a filter. The output of the AC source is limited by the measured impedance, which is expected to correspond to the current amplitude and power supply of the analog circuit. The measuring segment contains a high-pass filter, and a low-noise programmable-gain amplifier (PGA) to offset the large difference between the measured voltages on the paired electrodes. Further, the amplified output is connected to an ADC, where the signal is sampled with a pre-defined precision and resolution to be sent to the microcontroller or FPGA. The feeding and sensing segments are interconnected with a tomograph via a multiplexer. The requirements on the multiplexer include, above all, the following factors: (a) low resistance and small parasitic capacitance to minimize the amplitude and the phase shift errors, respectively, and (b) fast switching [60, 61].

Some of the major EIT systems marketed since 2005 are surveyed in Tab. 1.4, exposing the most important parameters and information, such as the name of the system, number of electrodes, injection current range, source specification (single (SFEIT) or multiple-frequency (MFEIT)), controller type, frequency range, ADC resolution, year of completion, and original reference [60, 61].

Tab. 1.4: The most widely favored EIT systems/devices.

System/device name	Electrodes	Injection current	Source	Controller	Frequency range	ADC	Year	Ref.
FIC	16	Max. 30 mA	2ch.	4x DSP	10 kHz - 500 kHz	12 bits	2005	[62]
UCLH Mk 2.5	64	0.3 mA	Single	DSP	20 Hz - 1 MHz	-	2006	[63]
KIT 4	80	0 - 5 mA	16 ch.	NI-PXI 6713	1 kHz - 120 kHz	14 bits	2008	[64]
OXBACT-5	64	0.4 mA	16 ch.	FPGA	1 kHz - 100 kHz	14 bits	2008	[65]
-	64	-	16 ch.	DSP + FPGA	10 kHz - 1 MHz	15 bits	2008	[66]
Voltage-applied ERT	16	Max. 320 mA	Single	-	10 kHz	-	2010	[67, 68]
LCT2	16	-	Single	Altera MAX 7000S	Max. 1 MHz	16 bits	2010	[69]
Parallel EIT	16	2.5 mA	Single	FPGA	50 kHz	-	2012	[70]
KHU Mark 2.5 EIT	16	-	4 ch.	DSP + FPGA	10 Hz - 500 kHz	12 bits	2014	[71, 72]
EIT Soc	32	0.1 - 1 mA _{pp}	Single	ASIC	10; 50; 100; 200 kHz	-	2014	[73]
EIT DAQ	16	DC/AC	Single	NI-CompactRIO-9024	-	24 bits	2015	[74]
-	32	Max. 5 mA _{pp}	Single	NI-PXI 1082e	100 Hz - 10 MHz	14 bits	2015	[75]
Z-meter IV	Max. 256	Max. 50 mA	Single	DSP	100 Hz - 200 kHz	12 bits	2016	[76]
Open EIT	32	-	Single	ADuCM350	80 Hz - 75 kHz	16 bits	2018	[77]
Portable EIT	16	0.1 mA	Single	ARM + FPGA	0 - 100 kHz	-	2018	[78]
SWEIT	16	0.1 - 10 mA	5 ch.	FPGA	1 kHz - 1.1 MHz	-	2020	[79]

The table contains devices from various application fields, including biomedical engineering; process, industrial, and geophysical tomographies; and laboratory experimentation.

2 Aims and objectives

The practical section of the thesis contributes to electrical impedance tomography in the following research subdomains, problems, and tasks:

- *Reducing the uncertainty of reconstructed conductivity distribution by optimizing the mathematical model*
 - Designing a precise physical model
 - Creating relevant parametric FEM models
 - Computing the domain parameters, including shape deformation, misplacement of the electrodes, and initial conductivity
 - Analyzing the sensitivity of the mathematical models with respect to the measurement-based inverse imaging
- *Accelerating the data acquisition process relating to unknown conductivities in laboratory and field conditions*
 - Improving the parameters in view of the existing solutions
 - Collecting the open data to be made accessible to the EIT community
- *Optimizing the parameters of the closed and the open domain models*
 - Exploring innapropriately constructed domain borders in the closed and the open domains and examining their impact on the reconstructed conductivity distribution
 - Determining the relationship between mesh density, number of elements, and computational effort
 - Analyzing the convergence error according to the selected regularization approach
- *Decreasing the image reconstruction time via parallelizing the algorithms*
 - Parallelizing the individual image reconstruction steps

3 Experiments

This chapter discusses the contribution and outcomes of the thesis. The first subsection presents an optimization procedure to precisely evaluate the individual domain parameters by using EIDORS. This procedure originates from a laboratory measurement on a tomograph, and its purpose is to demonstrate the impact of the individual parameters. The subsequent subsection, 3.2, describes the designing and properties of a device to facilitate effective data acquisition; this device includes, among other components, a low impedance multiplexer and a data acquisition unit. Part 3.3 outlines the impact of an extended domain (an improved parametric model), evaluates the convergence over the mesh element scale, and classifies the normalized error convergence of the selected regularization methods. The last portion of chapter 3 then characterizes the parallelization of the algorithm, delivering also a comparison of the CPU and GPU processes.

3.1 Optimizing the domain parameters

The sensitivity of the inverse image in terms of setting up the parameters is discussed in subsections 1.9 and 1.10, including the relevant research and available options. This chapter (3.1) outlines a novel approach to optimizing the domain parameters; in this context, we characterize the relevant numerical modeling and simulation, together with the laboratory measurement and applied instrumentation.

Optimizing the geometry of the model, regularity, and electrode placement fundamentally affects the image reconstruction [80]. The actual solution then lies in specifying and determining the parameters that are critical in terms of the accurate results, image artefact reduction, and computational effort. All of the items can be optimized during the inverse task, albeit at the expense of a higher computational intensity; for this reason, we decided to define in advance as many parameters as possible, via pre-calculation before launching the inverse solver [81].

In view of the purpose, the Nelder-Mead algorithm (Fig. 3.1) was employed as the procedure to adjust an imprecise domain setup by means of homogeneous sensing. The designed approach allowed us to verify the physical and the numerical FEM models, delivering a match between the resulting vectors of the simulated and the measured voltages. The heuristically based method facilitated solving nonlinear optimization problems where the derivative of the function is unknown. In such cases, the algorithm computes the relationship between the measured voltages and the properties of the domain. The method was implemented by using EIDORS library and the relevant Matlab optimization toolbox. The procedure had been designed to improve the reconstruction accuracy and to reduce the artefacts in inverse images [81].

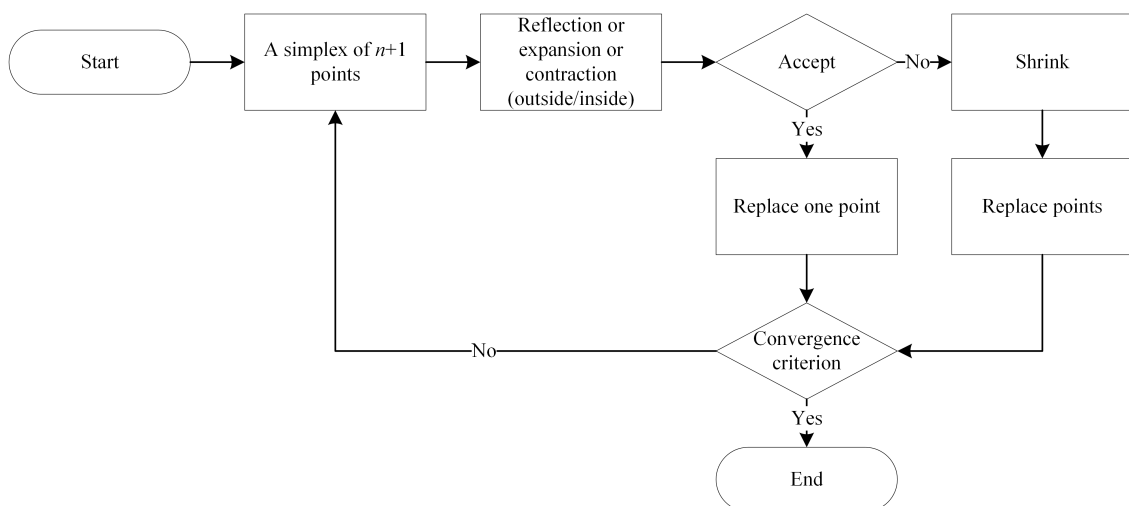


Fig. 3.1: The Nelder-Mead method [81].

The algorithm enables us to solve the listed parameters via the simplex. The simplex is defined as a geometrical shape in an \mathbb{R}^n space with $n + 1$ points; one of these points embodies the origin, and the others specify the direction of the space vector. When we have set the point of origin, the other n points are generated through several operations (reflection, expansion, and outside/inside contraction). Subsequently, the simplex moves and reshapes its geometry with respect to the performed operation, thus transforming itself; then, the worst vertex of the simplex is replaced with a better one after each iteration. Compared to the alternatives, this algorithm features easy implementability, ensuring a highly effective search for the local minimum; the innovative approach therefore finds use especially in adjusting the domain parameters [82, 83].

Principally, the algorithm relies on transforming the simplex. At the initial stage, we select the first point, on which an n -dimensional topology is formed. Next, the individual vertices, x_1 to x_{n+1} , are sorted with respect to the optimization function gradient, $f(x_1)$ being the best point and $f(x_{n+1})$ its worst counterpart. The iteration then results in generating a new point to substitute for the worst item. If the shrink operation launches, the substitution of n new points, except for x_1 , is performed and computed as the input to the subsequent iteration [82, 83, 84]. To facilitate the optimization, we defined the minimization function of the Nelder-Mead algorithm, yielding

$$f(p) = \frac{1}{2} \|\mathbf{U}_M - \mathbf{U}_{\text{FEM}}(p)\|^2, \quad (3.1)$$

where $f(p)$ is the minimization term of the least squares method, \mathbf{U}_M represents the vector of the voltage measured on the physical model of the laboratory tomograph, and $\mathbf{U}_{\text{FEM}}(p)$ stands for the voltage on the electrodes, computed via the forward task. The relevant domain is parametrized by p [81].

To visualize the implementation of the procedure, we can employ the diagram in Fig. 3.2. As indicated therein, the input comprises one or more selected parameters, including:

- parametric deformation of the domain boundary (in our case, circular/elliptical deformation);
- evaluation of the initial conductivity;
- electrode location on the border of the domain.

In addition to the input parameter/s, the optimization requires the vector of the measured voltages, which depends on the given current pattern; in this particular experiment, the sequence is measured on the non-excited electrodes. Exploiting the preset parameters and the voltage vector, the process initiates Netgen to generate the parametric FEM model. This model is computed via the forward task by utilizing EIDORS library [22]. The end solution then yields the voltage vector of the

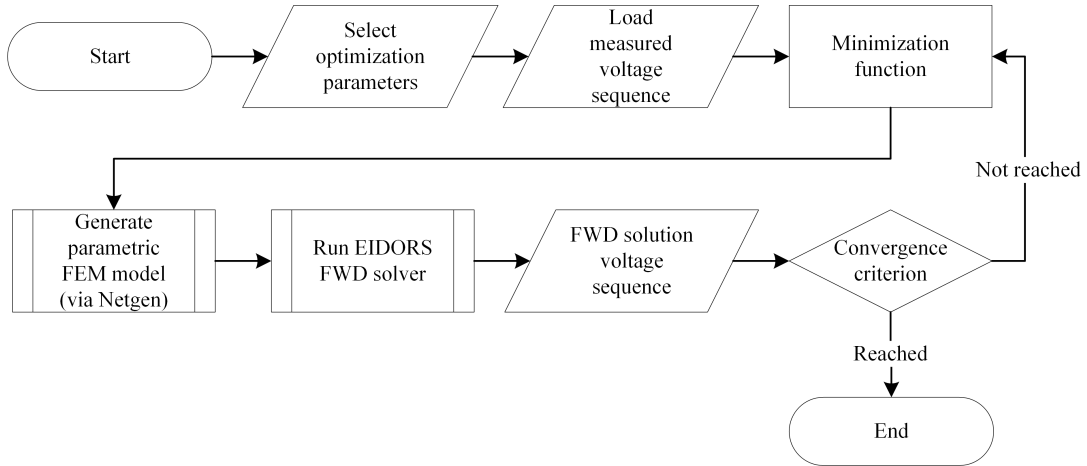


Fig. 3.2: The flowchart of the optimization procedure based on the measured dataset and selected parameters [81].

simulated numerical model, and the vector is evaluated by means of the optimization. If the sum of the squares reaches the convergence criterion, the optimization stops, and the return value of the function indicates the nearest possible value of the parameter preset by the user within the selected tolerance; otherwise, a new FEM model is generated and calculated via the forward task [81].

Where the procedure handles multiple unknown parameters p simultaneously, the computational time becomes longer, and the algorithm may not find a correct solution. To validate the functionality of the optimization, we employed a laboratory model with an inserted homogeneous medium; this step allowed us to verify the results physically. In addition to estimating the listed optimization parameters, the procedure has a potential to approximate the contact impedance by evaluating the sensing on the current-carrying electrodes. The actual impact of the parameters is demonstrated on inverse images that include inhomogeneities [81].

In the experiment, we used a laboratory tomograph and a corresponding numerical model (Fig. 3.3). The height and the diameter of the tomograph equaled 35.5 and 19 cm, respectively. The physical model also contained electrodes equidistantly distributed along its perimeter. The individual levels were located at 13.6, 21.6, and 29.6 cm above the bottom plane of the vessel; each stage involved 16 electrodes (stainless steel bolts) with the diameter of 9 mm and the height of 6 mm [81].

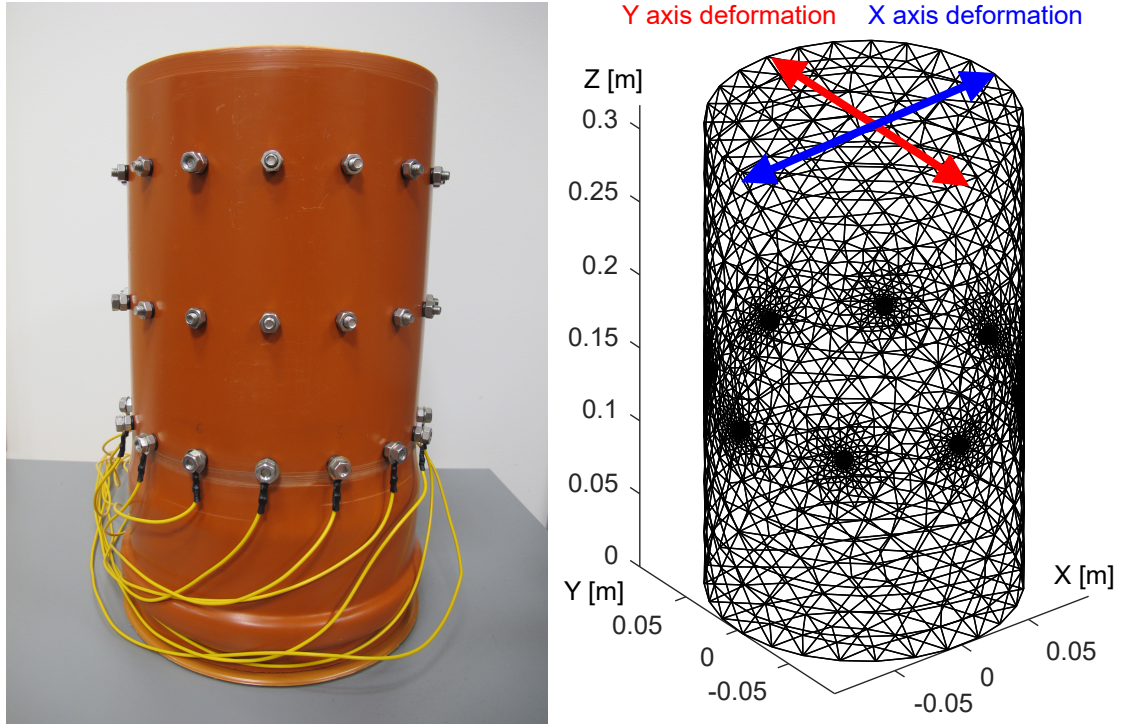


Fig. 3.3: The tomograph and the related Netgen-based numerical model [81].

To demonstrate the impact of the individual parameters on the inverse imaging, we set up an 8-electrode configuration. For the purposes of the optimization, we then prepared a corresponding, FEM-based model containing approximately 15,000 elements. The unused electrodes allowed us to form an irregular placement pattern on the domain boundary [81].

Initial conductivity

An optimal initial conductivity value to facilitate the image reconstruction constitutes a factor that potentially simplifies the convergency of the inverse solution and reduces the computational intensity. We employed potable water as the medium to optimize the initial conductivity. The input data were embodied in a vector of voltages measured via two current patterns (adjacent and opposite) and in two tomograph shapes (a regular circle and an elliptic deformation of approximately 2 %). The initial model to enable the optimization was designed with respect to the real dimensions, namely, the height and the regular diameter of 0.316 m (water level) and 0.19 m, respectively; the axis diameters of $X = 0.186$ m and $Y = 0.194$ m, capturing the elliptic deformation; the electrode placement level of 0.296 m above the bottom; and the contact impedance of $10 \text{ m}\Omega$, equaling the EIDORS default value. The sensing on the non-excited electrodes was accompanied by a small cur-

rent and thus a low voltage drop, leading to the conclusion that the impact of the contact impedance is, in general terms, almost negligible. The injected current was 2.002 mA at the frequency of 1,007 Hz. To start the optimization, we employed a TDS (total dissolved solids) conductometer, obtaining the initial conductivity value of 47.2 mS/m. The setup to acquire the data is shown in Fig. 3.4 [81].

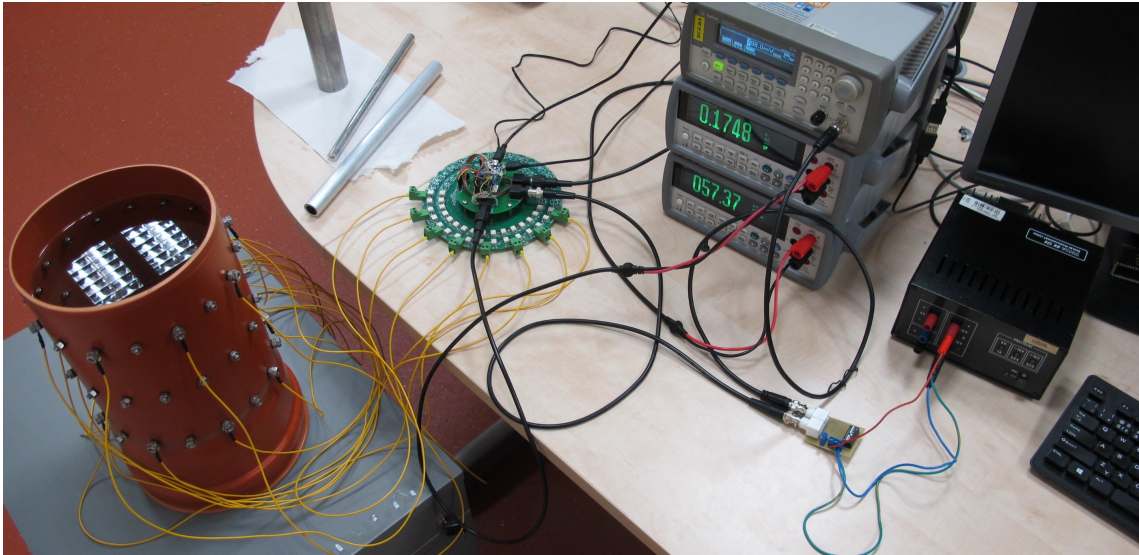


Fig. 3.4: The data acquisition setup [81].

The overall information is completed with the images below, which indicate a) the minimization function; b) the course of the conductivity value.

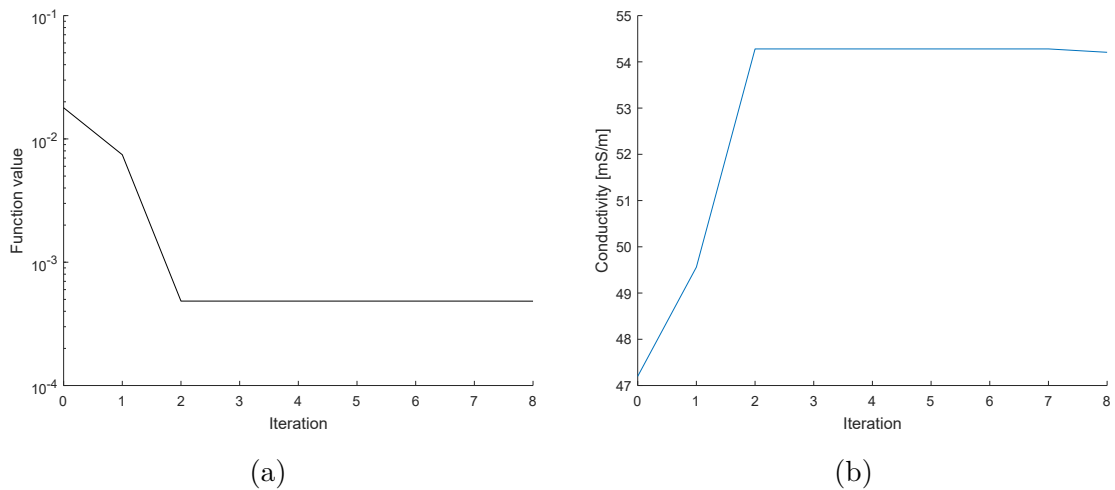


Fig. 3.5: The variation of the (a) minimization function, and (b) conductivity value during the optimization [81].

The variations of the minimization function and the conductivity value in an iteration are visualized in Fig. 3.5, images a) and b), respectively; the conductivity estimation converges very close to the real value in the 3rd iteration. In this state, the optimization generated new simplexes, which did not outperform the best result, and the algorithm stopped the process. The outcomes of the initial conductivity optimization, related to the stimulation patterns and domain shapes, are presented in the table below [81].

Tab. 3.1: Comparing the stimulation patterns in terms of the actual parameters and current injection values [81].

Current pattern	Domain shape	Conductivity [mS/m]
Adjacent	Circular	54.4
Adjacent	Elliptic	53.7
Opposite	Circular	54.9
Opposite	Elliptic	54.2

$$I = 2.002 \text{ mA}; f = 1,007 \text{ Hz.}$$

As indicated in Tab. 3.1, the optimization delivers the initial conductivity values associated with the current patterns and domain shapes. The variation of the values can be caused by the measurement uncertainty, noise, or limitations stemming from the FEM model deformation. The computational intensity of the optimization reached 7 s at the maximum, while the generation of the FEM model took 3.5 s [81].

Shape deformation

As already emphasized in subsection 1.9, the shape deformation influences the quality of the inverse imaging in all of the current patterns. To resolve this problem, we redesigned and extended the applied procedure; in addition, we prepared the same setup as that employed in optimizing the conductivity. The procedure enabled us to evaluate the shape deformation in the diameters X, Y. Within the initial step to run the optimization, we assigned the value of 19 cm (in each axis), thus starting with a circular shape. The variation of the diameters during the process is displayed in Fig. 3.6, together with the inhomogeneous reconstruction setup [81].

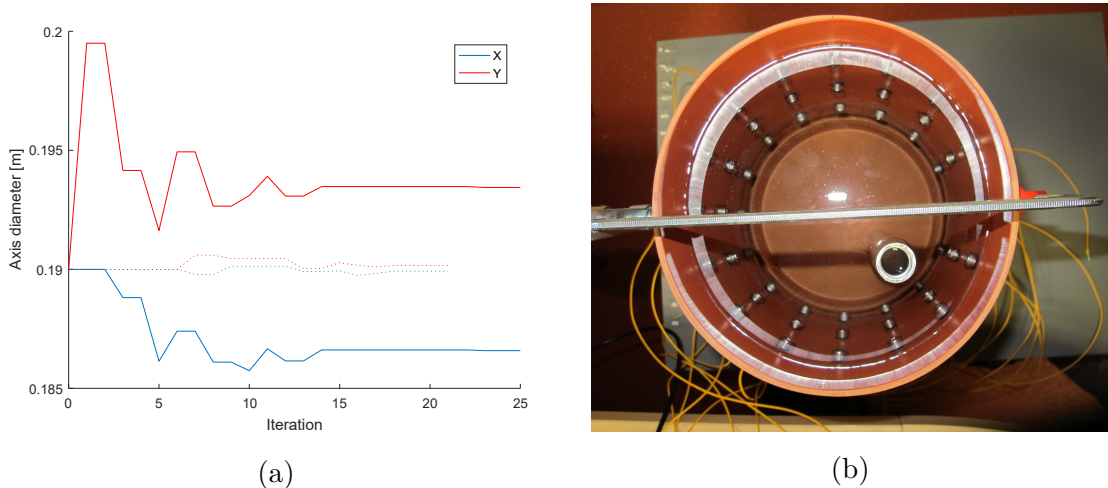


Fig. 3.6: (a) The variation of the diameters on the axes X and Y, relating to the OSP in the non-optimized (solid lines) and optimized (dotted lines) scenarios, and (b) the tomograph containing water and an inserted aluminum pipe [81].

In Fig. 3.6a, we characterize two different optimization scenarios: A non-optimized model, where the algorithm has found the diameters of the elliptic deformation (solid lines) of the circle, and an optimization of the original, or true, setup (dotted lines) to demonstrate the convergence ability and to specify the error of the algorithm. Based on the outputs of the homogeneous measurement, which were compared with the resulting vector of simulated voltages produced by the forward task, we calculated the shape deformation. The estimates of the optimized axis diameter equaled $X = 18.62$ cm, $Y = 19.35$ cm in the adjacent and $X = 18.66$ cm, $Y = 19.35$ cm in the opposite driving options. The values are very close to the real dimensions [18.6; 19.4]. The outcomes delivered by the opposite pattern show that the algorithm exhibits very good robustness. The error of the diameter values attained 0.1 %, corresponding to 0.2 mm on the absolute scale. The inaccuracy of the results may have arisen from insufficient precision in measuring the diameter or the voltage uncertainty. The deformation took between 205 and 250 s to optimize. The resulting diameters were employed as the inputs to perform the image reconstruction by means of a laboratory measurement of the potable water with an inserted aluminium object (Fig. 3.6b) [81].

To demonstrate the impact of an inaccurate domain boundary, we reconstructed the invalid and the true models, applying the adjacent and the opposite patterns (Fig. 3.7). The initial conductivity had been selected from within Tab. 3.1, with the regularization parameter set to 0.001 [81].

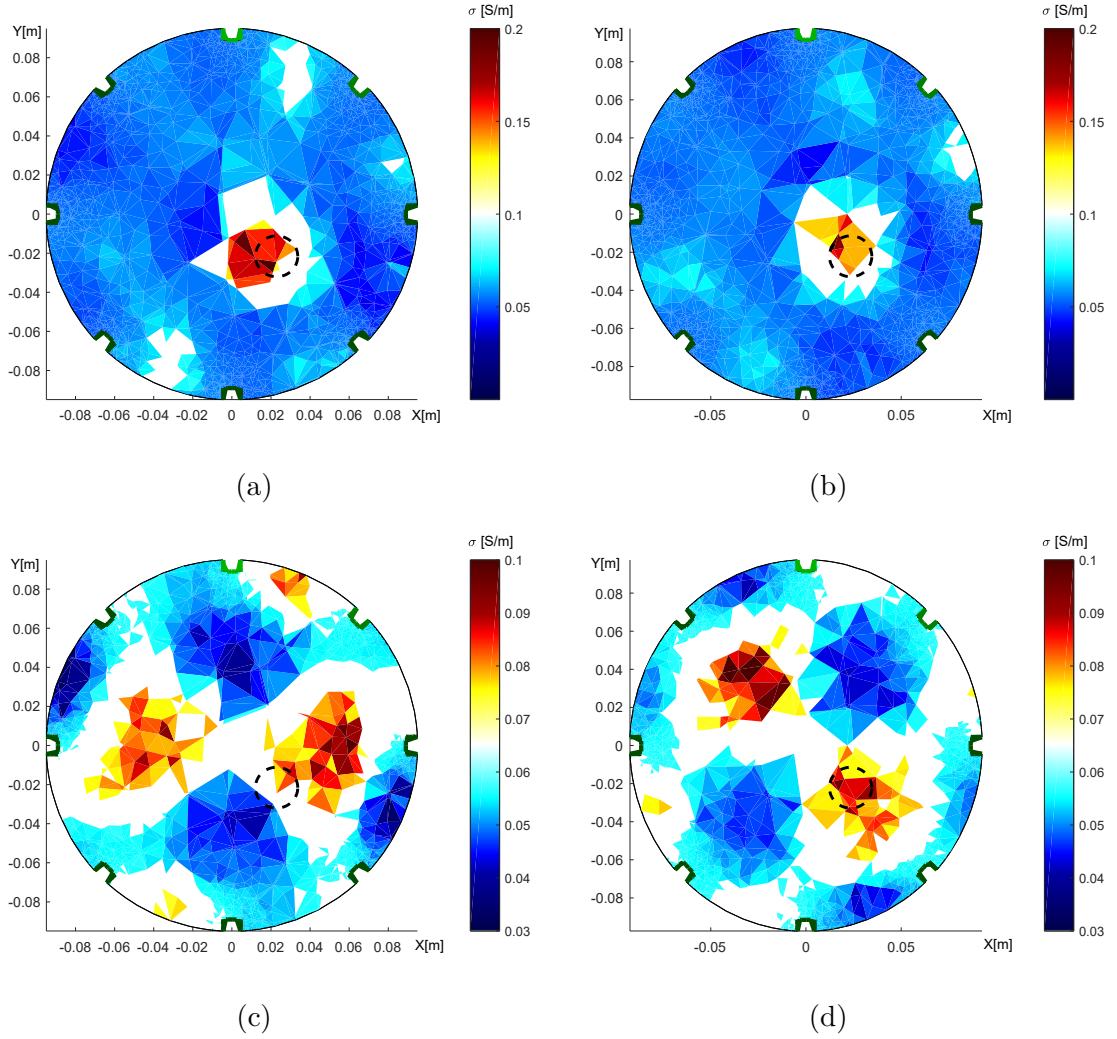


Fig. 3.7: The conductivity distribution in the water with an inserted aluminum object, obtained through the ASP (top) and the OSP (bottom). The tomograph's axial dimensions equal $X = 18.6$ cm and $Y = 19.4$ cm; (a,c) wrongly selected circular shapes, and (b,d) the true model of the elliptic domain [81].

The reconstructed images show the effect of the original domain model, where the imprecise domain boundary led to an incorrect localization of the inhomogeneity (Fig. 3.7a). By comparison, the optimized model (Fig. 3.7b) localized the aluminium object better but still did not deliver a flawless result. This problem could be eliminated by a more parametrizable model, namely, one conveniently deformable in multiple dimensions and shapes [81].

The conductivity images obtained via opposite feeding and sensing provided a higher sensitivity to the shape deformation. The imprecise boundary diameters (Fig. 3.7c) caused the inhomogeneous areas to rotate, unlike the conditions in the optimized model (Fig. 3.7d). Further, the inverse image exposed two higher con-

ductivity regions, and these corresponded to the original object and artefact. The mirroring of the object had been induced by the selected sensing configuration, with each of the paired electrodes measured twice to yield the same value at different polarities. The same effect had been recognized and described in references [85, 86]. The object mirroring is preventable via either an additional measurement to complement the opposite sensing pattern or another measuring configuration [81].

Misplaced electrodes

Together with the boundary deformation, misplaced electrodes embody a major source of artefacts and inverse imaging errors in our experiment. To analyze the problem, we set the tomograph in such a manner that the 6th electrode was shifted one step nearer the 7th one (Fig. 3.8a). Before running the optimization, we decided to utilize both homogeneous water to find the position of the electrode and a heterogeneous medium to demonstrate the impact exerted by the misplacement on the reconstructed image (Fig. 3.8b). The experiment was conducted identically to that used in optimizing the initial conductivity [81].

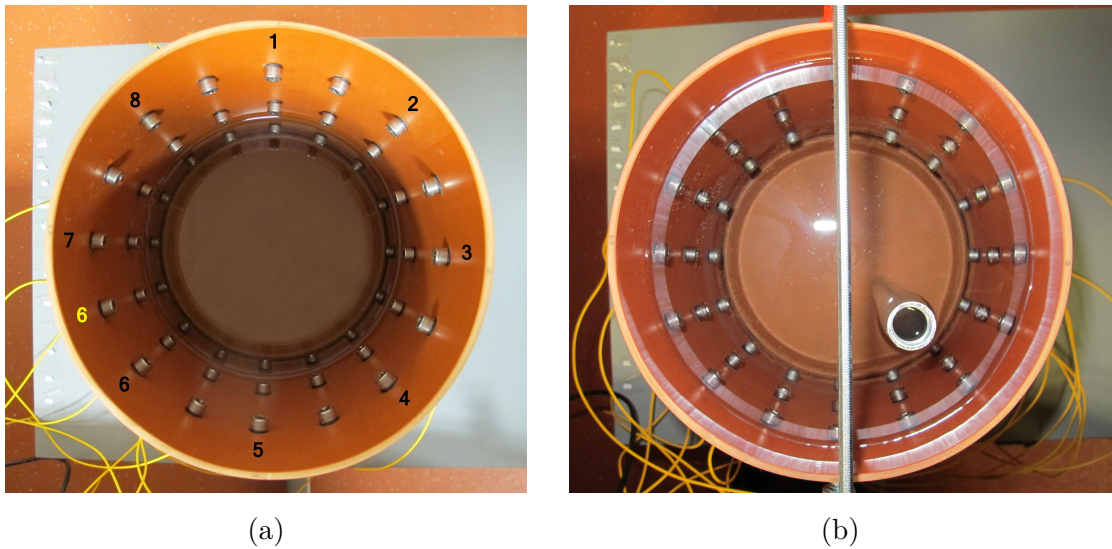


Fig. 3.8: (a) The setup including the shifted 6th electrode (highlighted in yellow); (b) the circular tomograph filled with water, comprising an aluminum object [81].

The variation of the minimization function error value over the individual optimization iterations and the changing position of the electrode related to the function count obtained via the simplex are shown in Fig. 3.9a, 3.9b [81].

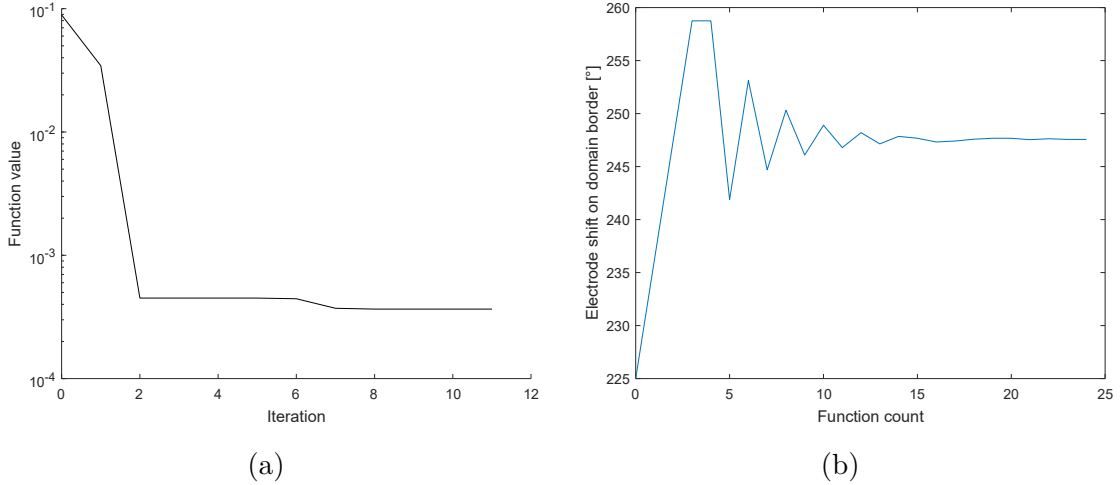


Fig. 3.9: Optimizing the electrode misplacement: (a) the error associated with the minimization function, varying with iteration; (b) the function count [81].

As regards the graphical representation above, Fig. 3.9a characterizes the variation of the optimization error over multiple iterations with respect to the location of the electrode and shows that the true electrode position is almost found in the 3rd iteration. Fig. 3.9b then visualizes the electrode shift, correspondingly to the changing value of the angle on the domain perimeter during the count of the optimization operations (Each optimizing iteration contains several steps, as explained at the beginning of this subchapter). The electrode moves along the domain boundary within the range of $225^\circ - 260^\circ$ and converges to 247.6° . The discussed procedure took between 90 and 110 s. The results of optimizing the electrode positions via adjacent driving are presented in Fig. 3.10 [81].

The images in the figure offer a top view of the domain models, featuring both the circular and the elliptic shapes. Each of the models was solved successfully, with the 6th electrode shifted in the same manner as in the original model (Fig. 3.8), where the misplaced electrode is highlighted with a yellow number. In addition to optimizing the position of the electrode through the adjacent pattern, we performed the experiment also by means of opposite sensing; the outcomes relevant to this latter option are shown in Fig. 3.11 [81].

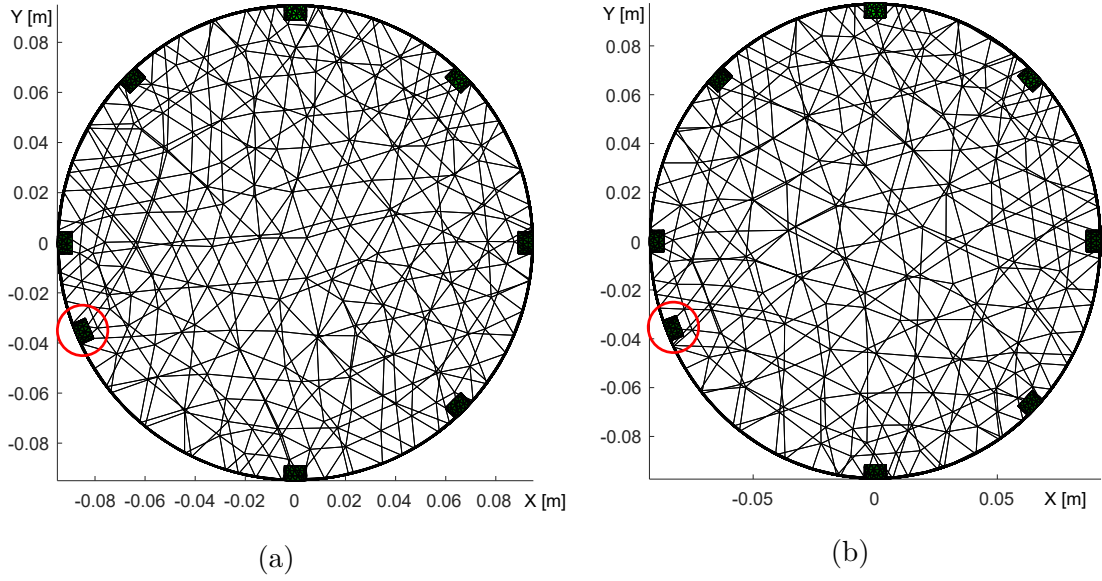


Fig. 3.10: A top view of the optimized domain meshes, focusing on the electrode shift in the (a) circular and (b) elliptic shapes [81].

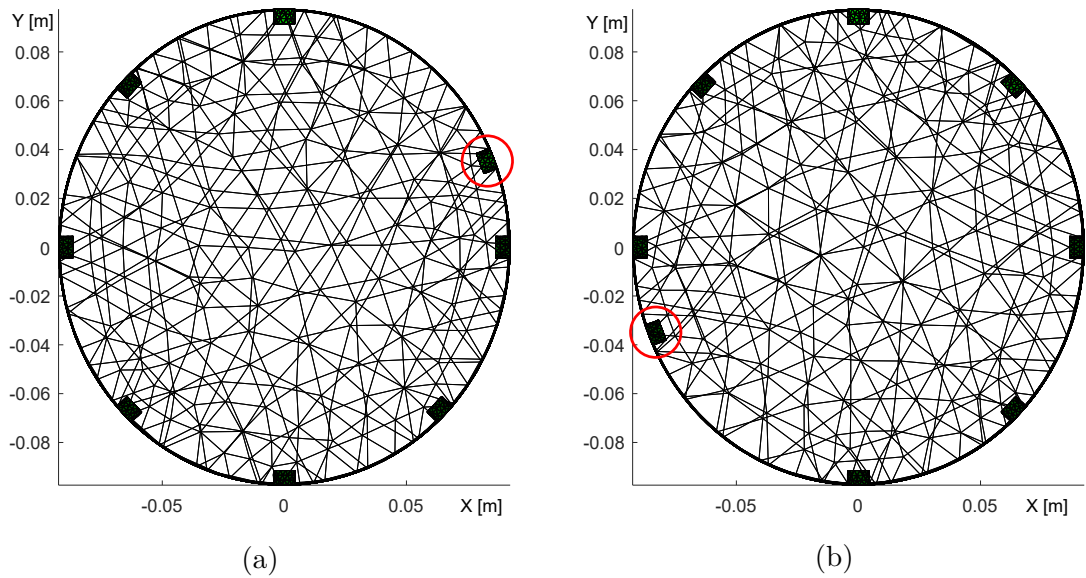


Fig. 3.11: A top view of the opposite sensing-optimized models, focusing on the electrode misplacement. The images display a duality of the solution, with either (a) the 2nd or (b) the 6th electrode shifted [81].

In the referenced figure, the drawings represent two comparable optimization results, which, although equal in terms of the vector of measured voltages, differ in correctness. The mesh on the left-hand side (Fig. 3.11a) contains the 2nd electrode evaluated at the angle of 68° with respect to the 1st electrode. The other mesh (Fig. 3.11b), by comparison, shifts the 6th electrode to 248° , the initial value

being 225° . Both of the FEM models are verified via the forward task, and the simulated voltages exhibit almost identical values. The detected duality meant that the optimization procedure had not yielded an acceptable result. Eventually, we found opposite sensing inconvenient for evaluating the electrode misplacement; the impact of such imprecise electrode positioning was thus reconstructed only with adjacent driving (Fig. 3.12) [81].

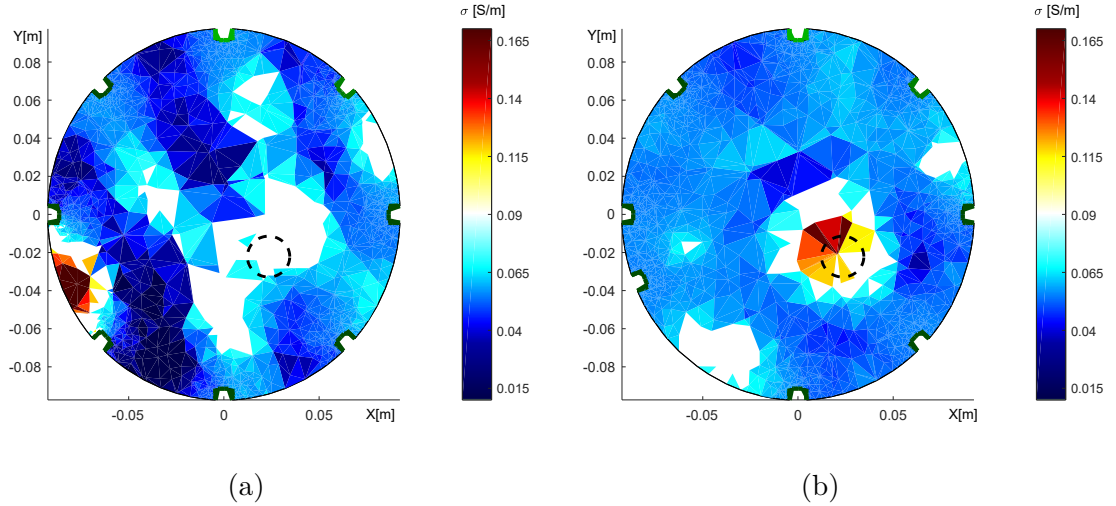


Fig. 3.12: The reconstructed conductivity distributions in the (a) inaccurate regular electrode setup and (b) correct placement of the 6th electrode [81].

An incorrect placement of the electrode is presented in Fig. 3.12a, together with the resulting inverse image. The reconstructed inhomogeneity was recognized wrongly, near the boundary between the 6th and the 7th electrodes. Compared to the imprecise model, the correct domain (Fig. 3.12b) includes the conductivity at the presumed position, localizing it satisfactorily. The randomly distorted conductivity areas in the reconstructed images could arise from an insufficient image resolution, limited by the number of active electrodes [81].

Error evaluation

To evaluate in the reconstructed images the conductivity distributions with respect to the original setup, we sampled the images at the resolution of 256×256 pixels. The accuracy was calculated via the relative root mean square error, by using the following equation [87]:

$$RRMSE(\sigma) = \sqrt{\frac{\sum_{i=1}^{px} (\sigma(i) - \sigma_{\text{orig}}(i))^2}{\sum_{i=1}^{px} (\sigma_{\text{orig}}(i))^2}} \cdot 100, \quad (3.2)$$

where $RRMSE(\sigma)$ denotes the total error in the sampled inverse image; px characterizes the number of pixels; $\sigma(i)$ stands for the reconstructed conductivity in a pixel; and $\sigma_{\text{orig}}(i)$ is the original conductivity of the FEM model, corresponding to the real measurement setup [81].

The area of the inhomogeneous object was evaluated through comparing the FEM model that represented the setup of the experiment with the one expressing the reconstructed conductivity distribution. To estimate the space of the object, we preset the experimentally established threshold to 66 % of the maximum conductivity, thus obtaining the mask to effectively separate the background from the inhomogeneity. This allowed us to compare the individual inhomogeneity areas, calculated via the equation

$$IAR_{0.66} = \frac{\sum_{i=1}^{px} (\sigma_{\text{Inv}}(i))}{\sum_{i=1}^{px} (\sigma_{\text{Fwd}}(i))}, \quad (3.3)$$

where $IAR_{0.66}$ is the area ratio between the original and the reconstructed conductivity regions of the inhomogeneity in the cross-sectional image, $\sigma_{\text{Inv}}(i)$ denotes the conductivity in the reconstructed image, and $\sigma_{\text{Fwd}}(i)$ represents the conductivity distribution in the FEM model that corresponds to the real laboratory setup [81].

The above equations enabled us to classify the actual impacts on the domain shape optimization process as regards the computed conductivity distribution. The outcome of the procedure is summarized in Tab. 3.2 [81].

Tab. 3.2: The image errors in the boundary deformations [81].

Current pattern	Domain shape	$RRMSE(\sigma)$ [%]	$IAR_{0.66}$ [-]
Adjacent	Circular	34.59	0.658/2.542
Adjacent	Elliptic	28.43	0.768/1.905
Opposite	Circular	51.99	0.274/5.947
Opposite	Elliptic	40.41	0.763/3.504

The measurement was performed on the elliptically deformed domain.

The $RRMSE(\sigma)$ values show decreasing error rates, with a drop of 6.16 % and 11.58 % in adjacent and opposite driving, respectively; in the former, the decrease

stemmed from a more accurate position of the inhomogeneity, while in the latter we had excluded the mirrored object as a systematic error due to the method and suppressed the deformation-induced rotation of the inverse image. The adjacent driving option brought an enhanced inhomogeneity area ratio of the complete domain model and a better match of the original object position, the relevant improvement rates being 0.637 and 0.11, respectively. The other technique then produced a (significant) drop by 2.443 in the complete image, with the inhomogeneity, by contrast, rising from 0.274 to 0.763. Based on these results, we can then conclude that the opposite feeding and sensing approach was more sensitive to the shape deformations. The outcomes relating to the impact of an incorrectly placed electrode are outlined in Tab. 3.3 [81].

Tab. 3.3: The image errors and electrode positioning [81].

Electrode position	$RRMSE(\sigma)$ [%]	$IAR_{0.66}$ [-]
Equidistant	52.73	0.000/1.483
6 th shifted	40.04	0.667/3.124

The measurement was performed by applying adjacent driving in the elliptically deformed domain, utilizing the non-equidistant electrode setup (shifted 6th electrode).

In the given context, the table also presents the values characterizing the overall error of the inverse image (Fig. 3.12). The optimized model reduced the relative error by 12.69 %, while the inhomogeneity area ratio of the whole domain increased by 1.641, and the presumed space of the object rose from 0 to 0.667 in the shifted 6th electrode. Regarding the equidistant setup, the inhomogeneity did not match with the correct position [81].

Summary

The initial conductivity was optimized with potable water, yielding between 53.7 and 54.9 mS/m in dependence on the actual combination of the current pattern and domain deformation (Tab. 3.1). The task converged very fast (Fig. 3.5), and the evaluation of the procedure took 7 s at the maximum [81].

In addition, the optimizing process evaluated the boundary deformation of the circular domain in terms of the variation of the diameter on the axes X and Y. To verify the designed procedure with real data, we had employed a clamp in the laboratory model to obtain a deformation of 2 %. The estimated modified diameters of the domain shapes equaled $X = 18.62$ cm and $Y = 19.35$ cm in the adjacent driving option and $X = 18.66$ cm and $Y = 19.35$ cm in the opposite pattern. Considering the real axial dimensions {18.6; 19.4} of the tomograph, the optimization delivered acceptable results. Evaluating the boundary deformation took 205 to 250 s, with a significant portion of the computational effort allocated to the generation of the meshes. The impact of the imprecise boundary modeling was demonstrated via reconstructing the image from the data measured on the elliptical domain. We performed the experiment on the accurate and the incorrect circular models (Fig. 3.7). The results show an imperfect localization of the inhomogeneity compared to its original position. In both of the driving techniques, the optimized model reduced the overall conductivity distribution errors by 6.16 % and 11.58 %. In the expected region of the object, the inhomogeneity area ratio defined through equation 3.3 increased from 0.658 to 0.768 (11.0 %) in the adjacent driving option and rose from 0.274 to 0.763 (48.9 %) in the opposite pattern, the latter change being especially remarkable. The area of the object in the space of the tomograph was also evaluated by applying the inhomogeneity area ratio, with the inhomogeneity volume in the inverse image diminishing from 2.542 to 1.905 in the adjacent driving approach and falling from 5.947 to 3.504 in the opposite pattern. The outcome of the optimization then lay in that the opposite option was considerably more sensitive to the shape deformations (Tab. 3.2). We also demonstrated the mirroring effect of opposite sensing to propose a solution which requires either complementing the measurement or selecting another sensing strategy [81].

The optimization procedure also facilitated evaluating the electrode misplacement, namely, another important source of errors in the inverse image. For this reason, we prepared the model containing the shifted 6th electrode. Observing the design of the experiment, we measured on an accurate (shifted) and an incorrect (regular, or equidistant) electrode setup of the model, via both adjacent and opposite driving. The optimization had to be supported by the dataset of the homogeneous conductivity measurement; taking into account the means available, the adjacent pattern proved convenient because, unlike opposite sensing, it does not de-

liver unacceptable duality. In this context, the duality means that the two different optimization products (the shifted 2nd and 6th electrodes) provide identical voltage values, which are interchangeable in the forward task (Fig. 3.11). Based on such an outcome, we decided to exclude the opposite pattern from the optimization of the electrode misplacement. We demonstrated the impact of an inaccurate electrode location via reconstructing the conductivity distribution with the adjacent pattern. The relationship between the recognition of the object and changes in the position of the electrode is exposed in the inverse images above. The relative root mean square error dropped by 12.69 %, and the inhomogeneity localization improved significantly, from a zero match to the similarity of 0.667 (in Tab. 3.3). The time required to compute the electrode misplacement ranged between 90 and 110 s [81].

The entire procedure was implemented by using the Matlab optimization toolbox, EIDORS tool, and Netgen mesh generator; the last of these softwares allowed us to generate the three-dimensional models. The designed scheme is suitable for adjusting the unknown parameters of the real laboratory model to create a corresponding numerical model for a precise image reconstruction. At present, the optimization solves only one parameter per run, this being one of the deficiencies; the other limitation consists in that the computational intensity grows with an increasing number of the degrees of freedom, which are computed simultaneously. The optimization concept is universal, bringing a potential to include another parameter, such as contact impedance; this capability is important in analyzing the current-carrying electrodes and multisource strategies. The procedure is independent of the applied mesh generator and can utilize multiparameter models compatible with the EIDORS tool [81].

Hardware and software

The experiment exploited the following devices and software [81]:

- CPU: Intel Core i3-6098P (3.6 GHz); 16 GB RAM;
operating system: Windows 10 (x64);
- Matlab R2016b (x64); EIDORS version 3.9;
- Keysight 34450A multimeter; Agilent DSO-X 3014A oscilloscope;
- PLI EIT system version 0.1.

3.2 Hardware for the tomographic measurement

This section presents the hardware design options relating to the experimental EIT measurement. More concretely in this respect, the focus is on a current source, a multiplexer, and a data acquisition unit; the devices (with the sole exception of the unit) then facilitated both the experimental imaging and the optimization process.

Specifications of the measurement system

To perform an appropriate tomographic measurement, we assembled and set up convenient hardware equipment. Based on the information outlined above in section 1.12, a prototype Precise Low-Impedance (PLI) system [81, 88] was designed, with a structure as follows:

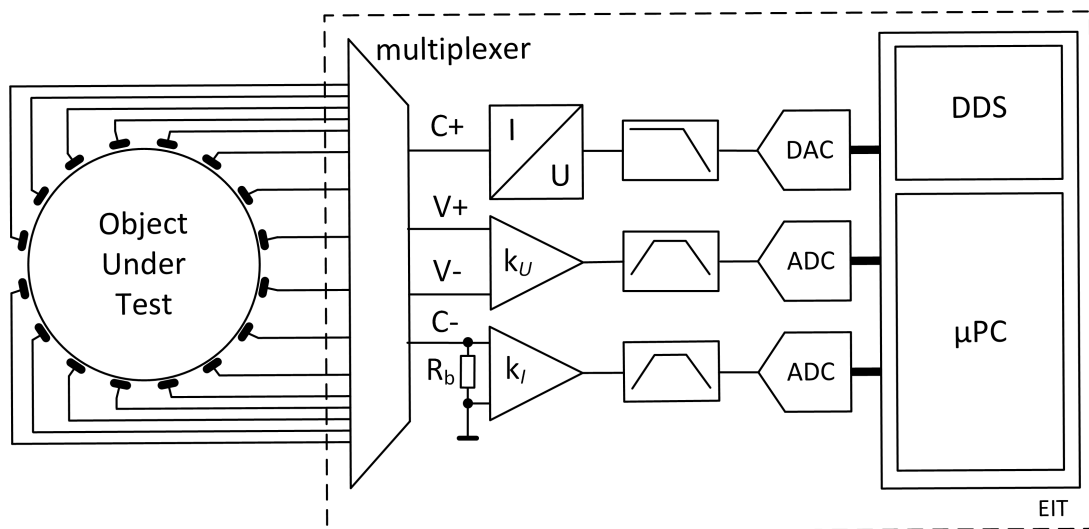


Fig. 3.13: The PLI EIT system [88].

As indicated in Fig. 3.13, the electrodes are connected to the multiplexer, which also wires them to the current source and the differential amplifiers as desired. In our case, the source was voltage-controlled and completed with a grounded shunt to measure the voltage gap by using another differential amplifier. The voltage gap on the shunt enabled us to control the AC current amplitude and to evaluate the frequency and phase shift of the signals. The other amplifier monitored the voltage on the electrodes of the tomograph [88].

Additionally, in the scheme being discussed, bandpass filters are installed behind the amplifiers to prevent voltage drifts and instability; the filters also suppress aliasing. The filtered signal passes to an ADC. The feeding part, by extension, comprises a low-pass filter and a DAC. The circuit is controlled by a microprocessor

including a digital generator (DDS) to precisely produce a harmonic signal to feed the tomograph [88].

The actual hardware is made up of three main items:

- a current source;
- a multiplexer;
- a measuring unit.

As regards the parameters of the components, the most important specifications are summarized in the table below.

Tab. 3.4: The ideal parameters of the equipment.

Parameter	Range
Frequency	10 Hz - 400 kHz
Phase shift resolution	1°
Measured voltage range	1 mV - 10 V*
Switching voltage	± 30 V
Multiplexer on-state resistance	< 10 Ω
Switching points per plane	16*
Injection current	0 - 3 mA _{pp}

The symbol * indicates parameters in which further expansion is desirable.

Based on the above knowledge, we specified the limit values of the individual desired parameters (Tab. 3.4). The current source was to be designed to operate at the frequency range between 10 Hz and 400 kHz, exhibiting the peak to peak value of 3 mA_{pp} for the load of 20 kΩ; the corresponding voltage supply was supposed to equal ± 30 V. Presumably, these parameters should enable us to measure soils in the laboratory tomograph. Further, from the overall perspective, the requirements on the multiplexer involve 16 electrodes per plane; easy extendability; very low on-state resistance (smaller than 10 Ω); switching voltage of ± 30 V at the minimum; and suitable cost. A low on-state resistance decreases the load of the current source, which could otherwise affect the measurement of the low impedance medium. The measuring unit is expected to operate at frequencies up to 400 kHz and voltages of 1 mV to 10 V; such parameters should allow the device to evaluate, at a precision of 1°, the phase shift of the harmonic signal between the current supply and the voltage sensing electrodes. All of the components ought to be selected with respect to easy assembly and repairs in a flat package. The measuring system will be connectable to standard laboratory instruments, such as a multimeter or an oscilloscope, and will also facilitate data acquisition by the assembled processor.

Current source

The first major requirement on the current source(s) is a high precision and stability over the frequency range. An ideal EIT current source should provide an infinite output impedance and be frequency-independent. Such prerequisites, however, are unrealistic due to the frequency-dependent characteristics of the individual components, stray capacitances, wide bandwidth, tolerance, and other aspects. The demands placed on a current source differ in terms of the target application: In various traditional industrial sectors, for example, the goal is to process and monitor the material, while fields such as biomedicine involve also additional safety issues [89].

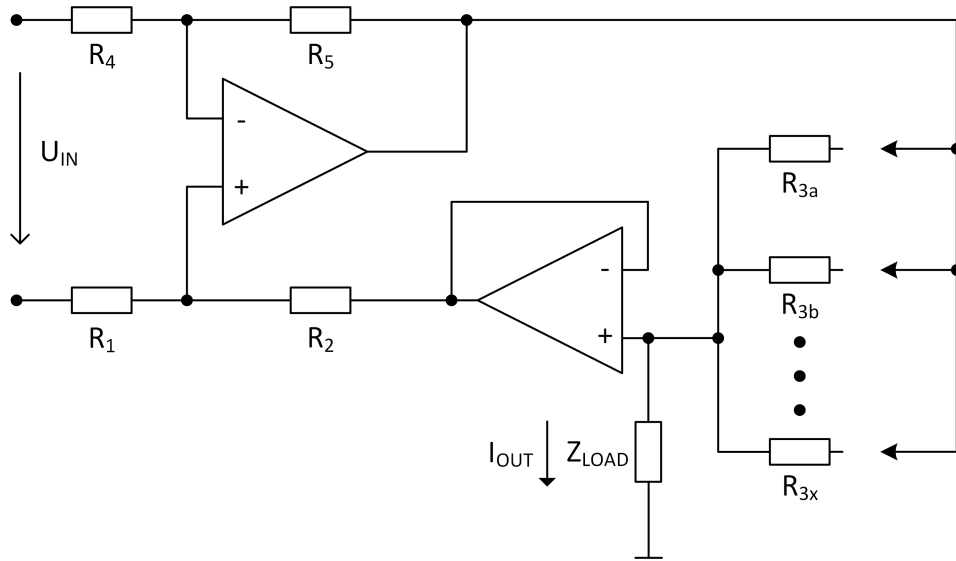


Fig. 3.14: The dual op-amp Howland current source.

For the soil monitoring purposes, we employed a Howland current pump including two amplifiers (Fig. 3.14). This circuit provides many advantages: Compared to the basic Howland current source, the dual op-amp pump ensures a low power consumption and a higher output swing. Moreover, when confronted with an improved Howland current pump, the selected circuit delivers a higher output impedance and a wider frequency range. Considering the amplifiers, one operates as a basic Howland source, and the other is connected as a voltage follower [89]. The correct functioning of this voltage-to-current converter is necessary to ensure the following resistor ratio equality condition:

$$\frac{R_1}{R_2} = \frac{R_4}{R_5}. \quad (3.4)$$

Here, the output current is given by the difference of the voltage between the inputs and resistor R_3 , via the relationship

$$I_{\text{OUT}} = \frac{U_{\text{IN}}}{R_3}. \quad (3.5)$$

The above equation shows that the output current amplitude can be set by changing the value of resistor R_3 or applying a different amplitude of input voltage U_{IN} . This circuit enables us to increase the output current amplitude in the lower load impedances at the same input voltage. A brief comparison of the amplifiers is outlined in Tab. 3.5.

Tab. 3.5: Some of the amplifiers for the dual op-amp Howland current source.

Name	CMRR	Bandwidth	Slew rate	Supply	max I_{OUT}	I_{LOAD}^*
ADA-4700	108 dB	3.5 MHz	20 V/ μ s	$\pm 5 - 50$ V	30 mA	2.5 mA
LT6018	124 dB	15 MHz	30 V/ μ s	$\pm 3 - 15$ V	50 mA	0.9 mA
LM7301	88 dB	4 MHz	1.25 V/ μ s	$\pm 2.2 - 16$ V	20 mA	1.0 mA
OP285	106 dB	9 MHz	22 V/ μ s	$\pm 4.5 - 22$ V	30 mA	1.5 mA

I_{LOAD}^* specifies the estimated currents up to the load of 20 k Ω .

The presented table characterizes the ADA-4700 amplifier as the best candidate in terms of the specified requirements. The selected amplifier provides a good CMRR, slew rate, and output current; thus, despite having the lowest bandwidth, the ADA-4700 appears to be fully sufficient for our purposes. The power supply exhibits a relatively high range ($\pm 5 - 50$ V), allowing us to increase the current injected into the high load impedance.

Multiplexer

The multiplexer constitutes another major component of the analog design to facilitate data acquisition in EIT. The requirements include, above all, switchability between the 16 electrodes at ± 30 V, and the smallest possible on-state resistance. A brief overview of currently marketed multiplexers is proposed in Tab. 3.9 [88, 90].

Tab. 3.6: Selected multiplexers and their parameters.

Name	Configuration	Resistance	Voltage supply	Package
ADG1406	16:1	9.5 Ω	$\pm 5 - 15$ V	TSSOP/LFCSP
ADG706	16:1	2.5 Ω	± 2.5 V	TSSOP
MUX506	16:1	125 Ω	$\pm 5 - 18$ V	TSSOP/SOIC
CD4067B	16:1	125 Ω	$\pm 2.5 - 10$ V	TSSOP/SOIC

As is shown in the table, all of the multiplexers have narrow operating ranges, limited by the voltage supply. For this reason, we decided to create a discrete multiplexer from single, galvanically separated switches. We applied a TLP3545A

photorelay, which enabled us to switch 60 V and also provided a very low on-state resistance (40 m Ω) in the DIP-6 package. The switching logic was controlled by an HV5530PG-G shift register (32 channels at 12 V). We opted for this component to yield the possibility of easily extending the multiplexer via chain connection. The configuration of the switching photorelays is represented in Fig. 3.15 [88, 90].

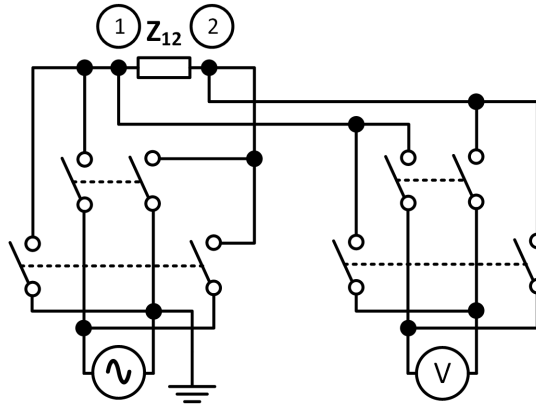


Fig. 3.15: The photorelay switching of the current source and the voltmeter [88].

The actual design is presented in Fig. 3.15, where Z_{12} stands for the impedance of the medium in the tomograph between two electrodes (1 and 2). To connect the current source and a voltmeter or an ADC, eight analog switches are required; the complete 16-electrode multiplexer thus contains 128 photorelays.

Measuring unit

Another two operations to be executed by the data acquisition unit consist in the actual measurement and the data conversion. An ideal measuring unit is expected to contain a programmable gain amplifier, an ADC, and a hysteresis comparator; all of the components should be galvanically separated from the controller. The requirements placed on the design were specified above, Tab. 3.4. To ensure the desired parameters, Tabs. 3.7, 3.8, and 3.9 summarize the most convenient options available in designing the individual parts.

Tab. 3.7: A selection of suitable amplifiers.

Name	CMRR	Bandwidth	Slew rate	Supply	Gain	Package
AD8253	100 dB	550 kHz*	12 V/ μ s*	\pm 5 - 15 V	1 - 1,000	MSOP
AD8221	80 dB	100 kHz*	2 V/ μ s*	\pm 2.3 - 18 V	1 - 1,000	MSOP
AD8231	80 dB	7 MHz \dagger	1.1 V/ μ s \dagger	\pm 1.5 - 2.5 V	1 - 128	LFCSP
AD620	100 dB	120 kHz*	1.2 V/ μ s*	\pm 2.3 - 18 V	1 - 10,000	DIP

* Gain = 100; \dagger Gain = 128.

As regards the amplifier that best satisfied our needs, we selected the AD8253, which generally provides a good common-mode rejection ratio (100 dB), together with a sufficient bandwidth (550 kHz) and slew rate (12 V/ μ s) at a hundred-fold amplification of the input signal. The integrated circuit can be supplied with a maximum of ± 15 V and features variable gain, from 1 to 1,000 by decade; furthermore, the MSOP package facilitates simple assembly and reworking of the component. Compared to the other products, the AD8253 appears to embody the truly optimal choice.

Tab. 3.8: A selection of suitable ADCs.

Name	Bandwidth	Sampling rate	U_{IN} range	Resolution	Package
AD7322	22 MHz	1 MSPS	± 10 V	13 bit	TSSOP
AD7825	10 MHz	2 MSPS	0 - 2.5 V _{pp}	8 bit	TSSOP
AD7922	8.5 MHz	1 MSPS	0 - 5.25 V	12 bit	MSOP
AD7091R-2	1.5 MHz	1 MSPS	0 - 5.25 V	12 bit	LFCSP
ADS8920B	23 MHz	1 MSPS	± 5 V	16 bit	VQFN
ADS8861	30 MHz	1 MSPS	± 5 V	16 bit	VSSOP

The list in Tab. 3.8 comprises ADCs that conveniently satisfy the design criteria. To equip the measuring unit, we chose the AD7322: This model has the widest input voltage range, compatible with the output of the amplifier; delivers a good sampling rate (1 MSPS) with respect to the frequency range requirements (400 kHz); ensures a sufficient resolution to evaluate the voltage on the electrodes; and operates within an ample bandwidth. The other options, by comparison, offer lower input voltage ranges or no-lead packages (and such packages are not easily reworkable).

Tab. 3.9: A selection of convenient comparators.

Name	U_{IN} range	U_{IN} offset	Time response	Package
LM211	30 V	0.7 mV	115/165 ns	SOIC-8
LM397	30 V	2 mV	900/940 ns	SOT-23
LM339	30 V	2 mV	1300/300 ns	SOIC, SSOP
LM393	36 V	1 mV	1300 ns	SOIC, DSBGA

In Tab. 3.9, we evaluate applicable comparators to measure the phase shift in harmonic signals between the feeding and the sensing branches (wings). The most advantageous parameters, i.e., the lowest input voltage offset and the shortest time response, are guaranteed by the LM211 as the item of our choice.

The figure below characterizes the design of the measuring unit including the above-described integrated circuits. In the diagram, only one sensing wing is visualized because the other has the same structure.

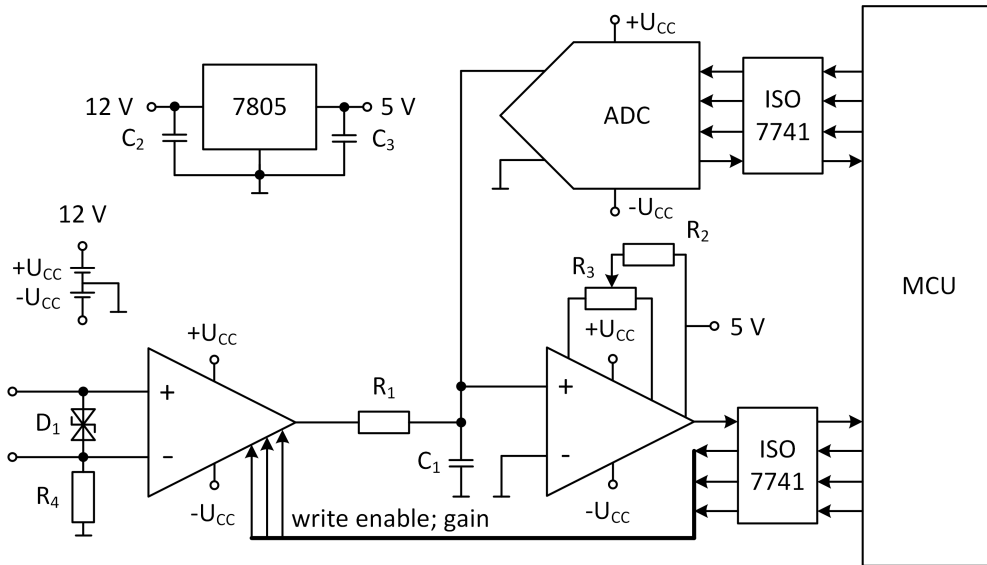


Fig. 3.16: The measuring branch containing a programmable gain amplifier, a filter, an ADC, and a hysteresis comparator.

The measuring unit relies on two supply values: 12 V to feed the PGA, ADC, and hysteresis comparator, and 5 V for the comparator reference. The inputs of the amplifier are directly connected to the outputs of the multiplexer; between the amplifier inputs, a TVS diode is placed to prevent damage to the circuit. The indicated resistor R_4 forms the DC feedback of the amplifier inputs with respect to the power supply. Behind the amplifier, we inserted an RC filter as an aliasing filter having a bandwidth adjusted to approximately 440 kHz. The output of the filter is connected in parallel to the ADC and the hysteresis comparator. The comparator facilitates detecting the frequency, and also the phase shift of the signal (however, the device has to cooperate with another, identical circuitry to monitor the injected current). Of the remaining resistors, R_2 and R_3 enable us to set the value of the voltage hysteresis to avoid noise-induced oscillations. Based on evaluating the frequency and using the ADC, the applied MCU determines precisely the time to read the signal at the amplitude. The ADC then measures the amplitude multiple times, and the final voltage value is specified as the mean of the individual measurements in the pre-defined time frame. The communication between the PGA, ADC, and comparator is expected to be galvanically separated by ISO7741 digital isolators. The microcontroller (STM32F103RCT6) handles the gain of the instrumentation amplifier, reads the digitized information of the voltage value, and evaluates the frequency and the zero cross time to compute the phase shift of the signals. The power supply is supposed to exploit isolated DC/DC converters to avoid ground loops, with an inserted LC filter on the output to suppress ripple and noise; alternatively, the

device can be battery-powered. The circuit design is expected to include test points to interconnect with laboratory devices such as a voltmeter or an oscilloscope, the purpose being functionality verification.

In general terms, the measuring unit will enable us to evaluate the required signal conditions, which are described at the beginning of this section. The combination of PGA gain and ADC resolution will facilitate processing low-level signals (1 mV), together with their amplification (1 V) and digitizing at the step of 0.24 mV (correspondingly to 12-bit conversion). The phase shift of the signals is to be evaluated at a precision of 1° . The only drawback of the design rests in that the voltage reading uncertainty depends also on the quality of the frequency evaluation given by the hysteresis comparator and the integrated microcontroller counter.

Results

The device is still being developed at present; thus, this section discusses only a partially assembled prototype of the Precise Low-Impedance EIT system (PLI EIT, Fig. 3.17).

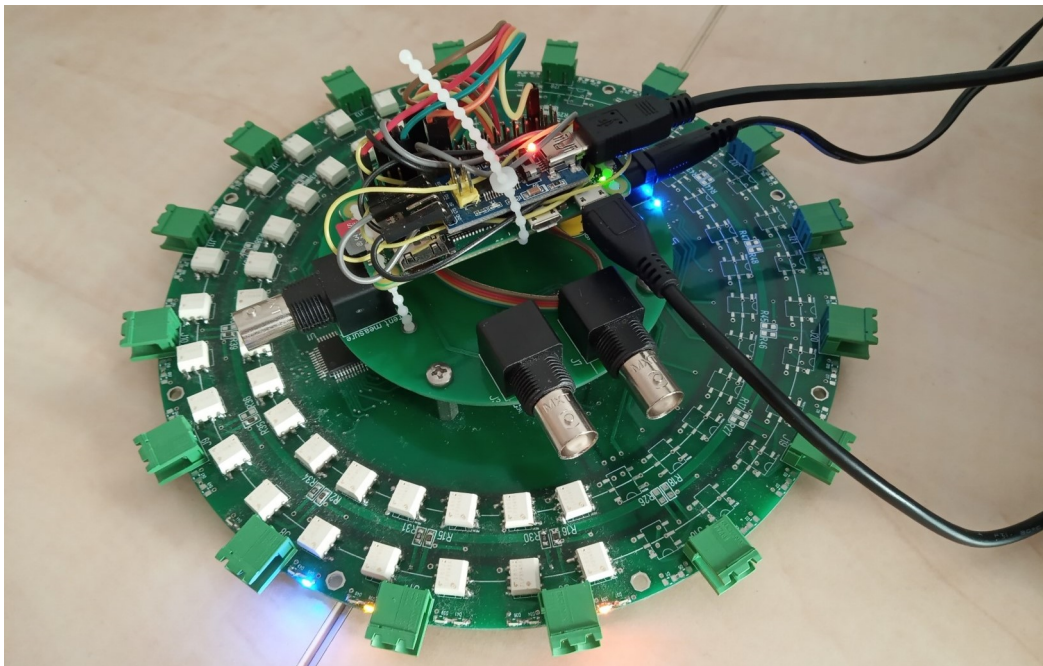


Fig. 3.17: The PLI EIT prototype [88].

As outlined in the previous chapter, the prototype contains a low impedance multiplexer; a shunt resistance; a microcontroller that manages pairs of switching electrodes through commands generated by a LabView-based software; and an external VCCS. The resistance of the multiplexer was verified via brief impedance measurement over two channels connected in series (Fig. 3.18).

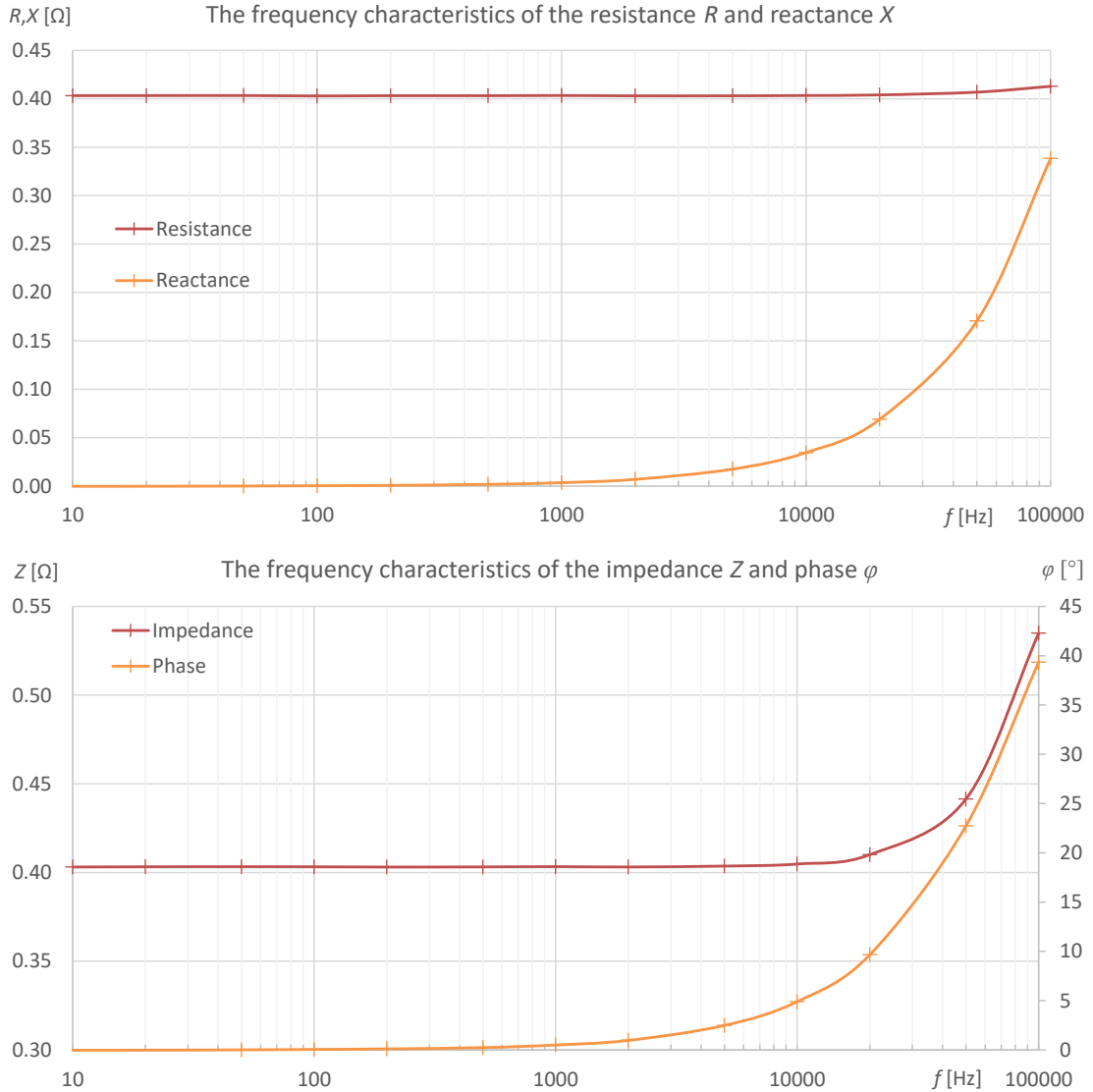


Fig. 3.18: The frequency characteristics of the multiplexer’s resistance, reactance, impedance, and phase.

The measurement of the multiplexer’s parasitic parameters indicates a very low resistance and reactance in the monitored range. The first characteristics show that the reactance starts to grow at 1 kHz, rising gradually and then steeply up to about 0.35 Ω at 100 kHz. The bottom image in Fig. 3.18 represents the impedance and phase shift variations with respect to the frequency; as is obvious, the impedance begins to increase at 10 kHz and rises from 0.40 Ω to 0.54 Ω at 100 kHz. The phase of the impedance then jumps from 0 to 40 degrees between 1 and 100 kHz. The multiplexer’s impedance can be considered very low (smaller than 1 Ω), and the relevant parasitic impact on the measured values is almost negligible [88, 90].

Experimental reconstruction using the PLI EIT prototype

To launch the reconstruction procedure, we employed a tomograph and the above-discussed PLI EIT prototype (the VCCS and multiplexer), which was supported by applicable laboratory devices (a function generator, digital multimeters, and an oscilloscope). The images display a diagram of the voltage and phase shift measurement circuit and visualize the setup for customizing the inhomogeneous conductivity distribution.

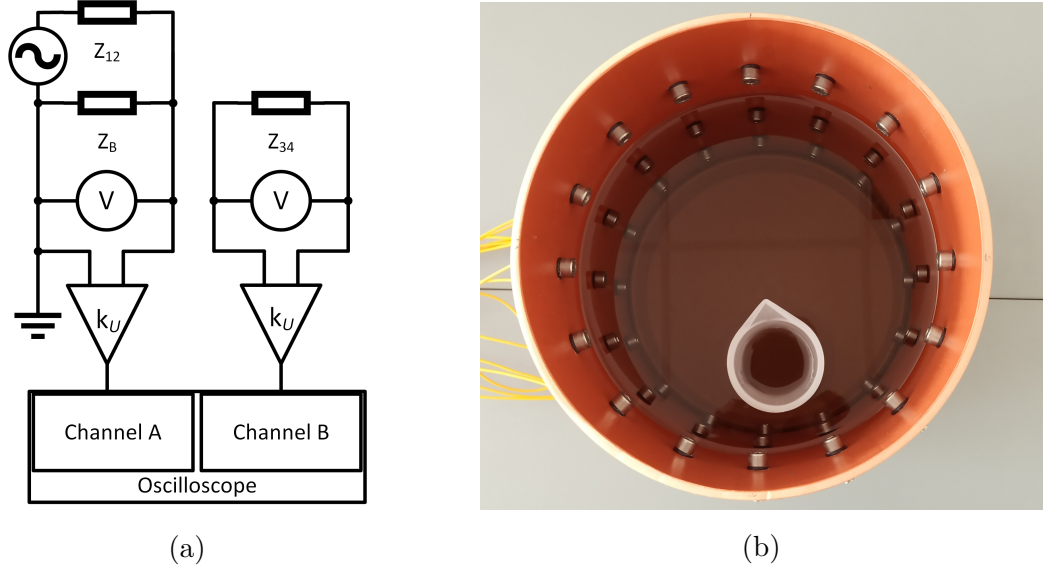


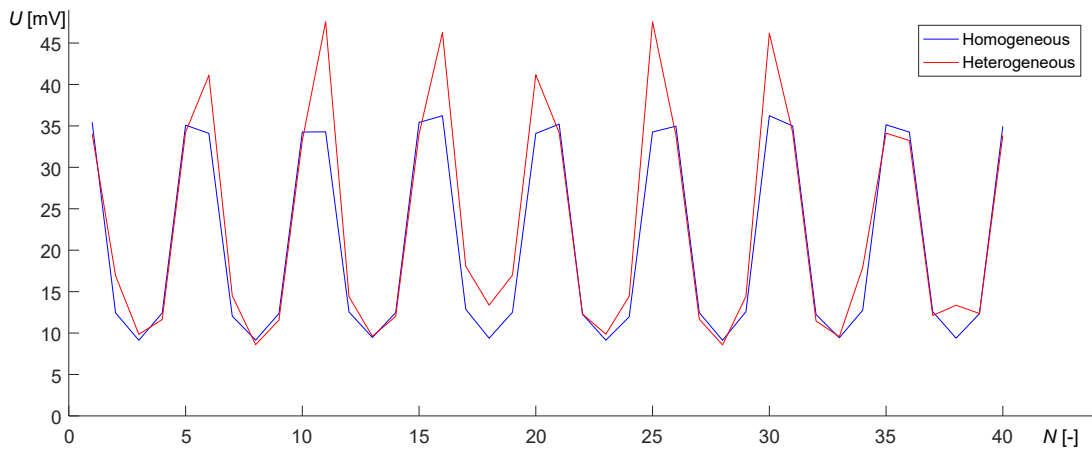
Fig. 3.19: (a) A diagram characterizing the voltage and phase shift measurement circuit; (b) the tomograph with an inserted graduated cylinder [91].

In Fig. 3.19a, we introduce the feeding and sensing wings, which are galvanically separated. The symbols Z_{12} and Z_{34} represent the impedances between electrodes 1-2 and 3-4. The feeding part of the circuit comprises an AC source including a function generator, and a VCCS as a voltage-to-current converter. To conduct the experiment, the AC source output was connected with the excitation electrodes of the tomograph through a shunt resistance ($Z_B = 10 \Omega$), to which we wired the voltmeter, differential amplifier, and one channel of the oscilloscope. The voltmeter enabled us to evaluate, verify, and control the amplitude of the injection current. Combining the amplifier and the oscilloscope then ensured the measurement of the phase shift between the feeding current and the voltage measured in the second branch [91].

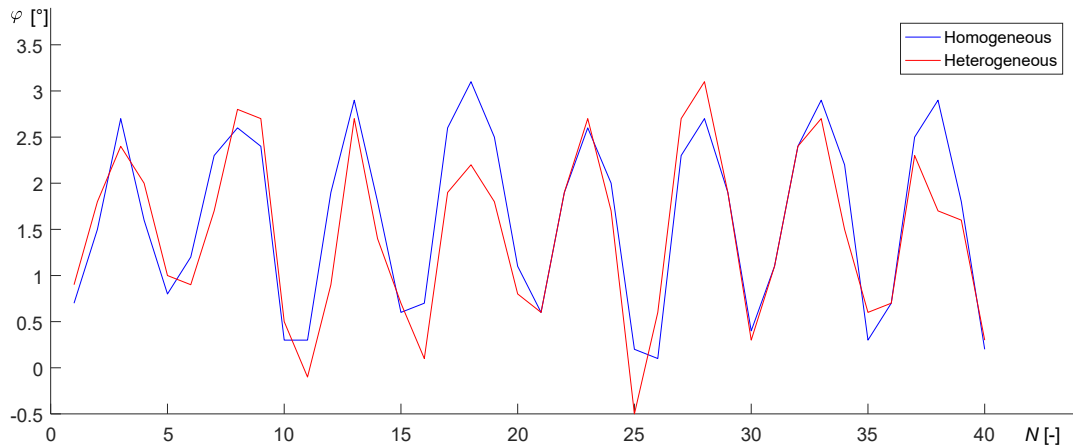
The measuring wing of the circuit contained the above impedance Z_{34} , where the voltmeter indicated the voltage between a concrete pair of electrodes. Furthermore, the differential amplifier and the oscilloscope channel B, interconnected in series, were wired in parallel to the impedance; thus, we scanned the harmonic signal to measure the phase shift for the purposes of admittivity evaluation [91].

The setup of the experiment is depicted in Fig. 3.19b, with the images showing the water-filled tomograph and the graduated cylinder inserted to generate an inhomogeneity having a pre-defined shape [91].

In the experiment, we utilized 8 electrodes arranged on a single level. The injection and sensing pattern relied on the ASP; this configuration allowed us to carry out 40 measurements. The injected current (I_B) equaled 2.008 mA at 1,007 Hz, and the excitation current was measured on the shunt resistance (Z_B). By extension, we measured the sequences of the voltage and the phase shift of the signals monitored under homogeneous and inhomogeneous conductivity distributions (Fig. 3.20) [91].



(a)



(b)

Fig. 3.20: The sequences of (a) the voltage and (b) the phase shift of the signals between the pairs of excitation and measuring electrodes. The sensing of the homogeneous and the inhomogeneous media is illustrated by the blue and the red teeth, respectively [91].

The voltage and the phase shift measured in the water-filled tomograph are characterized by the blue teeth in Fig. 3.20a and 3.20b. The variation of the voltage values (which is most apparent at the local maxima) could be caused by an imprecise placement of the electrodes or the contact impedances between an electrode and the measured medium. The patterns of the values obtained on the perimeter correspond to the assumption, namely, that the voltage loss will decrease with increasing distance. The phase shift between the injected and the measured signals rose with increasing distance to reach 2.6° - 3.2° . The variation had likely originated from the magnitude of the voltage, this being approximately 10 mV; the oscilloscope, however, offers a resolution of only 1 mV [91].

The follow-up measurement was performed with the graduated cylinder inserted in the tomograph. The relevant voltage sequence displayed by the red tooth exhibited an inhomogeneity between the 3rd and the 6th electrodes. Compared to the homogeneous state, the discussed region showed a step increase of the voltage values in the range from 40 mV to 47 mV. Changes in the voltage values were clearly observed also in some of the other electrodes, where, for example, the shape of the voltage pattern did not correspond to the exponential form (the 38th value). The measured phase shifts of the signals (Fig. 3.20b) did not differ markedly from those of the homogeneous sequence. In both cases, the phase shift values ranged between 0° and 3° , probably due to the phase noise and measurement uncertainty. The measuring procedure exposed that the non-conductive object inside the tomograph had increased the voltage values on the closest electrodes, and it also revealed a negligible drop in the phase shift between the feeding and the sensing signals [91].

When reconstructing the image, we employed Netgen to prepare a mesh including 17,708 elements. In the FEM model, the mesh was refined near the electrodes and boundaries, allowing us to compute the admittivity distribution more accurately. The actual reconstruction accuracy was given by the fineness of the electric field values and the mesh resolution in the vicinity of the electrodes. The reconstruction was performed via a difference inverse algorithm utilizing the objective function, and this algorithm involved the Gauss-Newton method complemented with a Tikhonov regularization term. The reconstructed admittivity components are visualized in Fig. 3.21 [91].

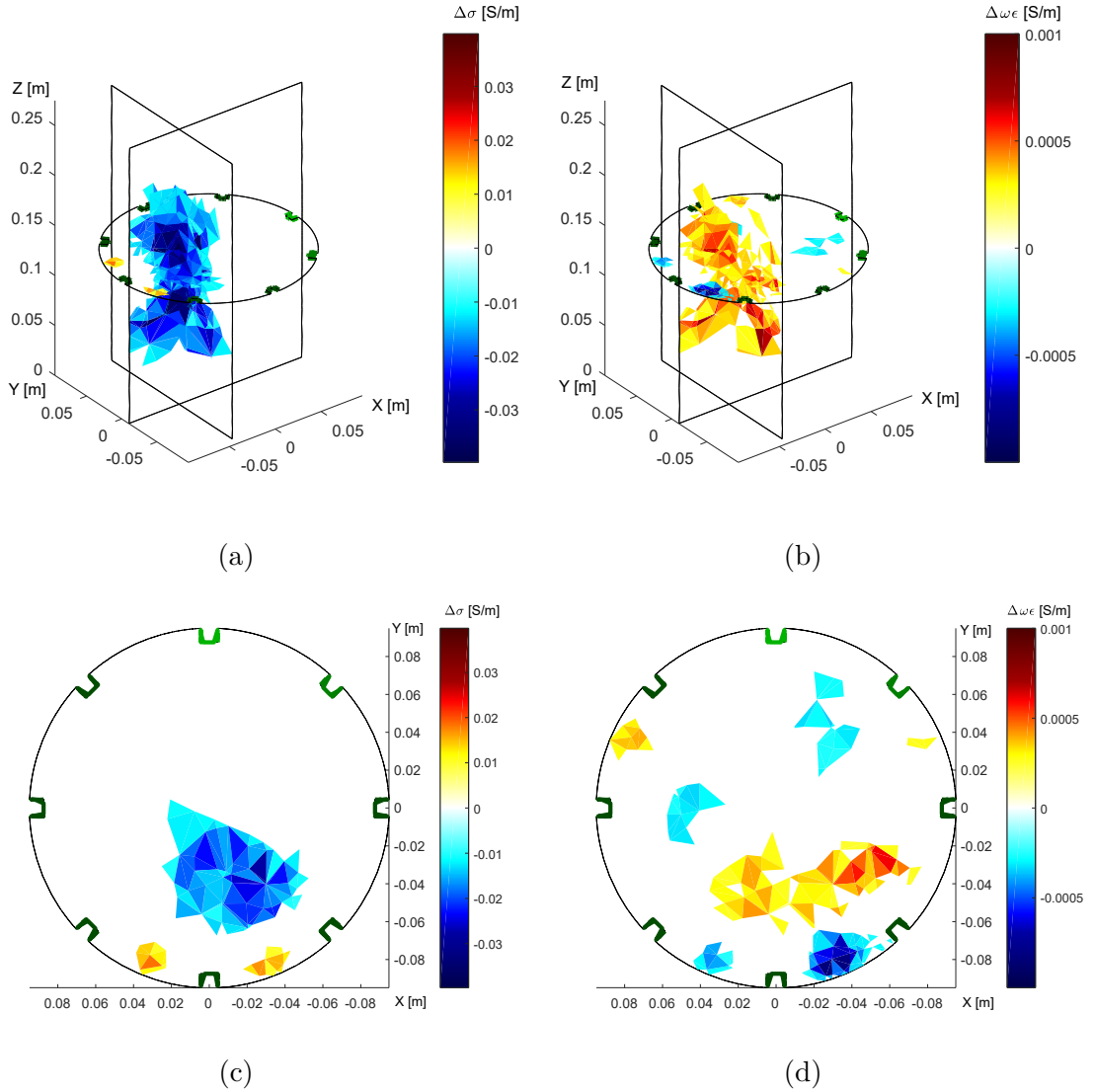


Fig. 3.21: The reconstructed difference in the admittivity distribution: three-dimensional cross-sectional images (top), and two-dimensional cross-sections at the electrode level (bottom) [91].

The cross-sectional images (Fig. 3.21a, 3.21c) of the conductivity indicate an inhomogeneity region around the coordinates $[-0.01; -0.04]$. Unlike the conductive water (46.4 mS/m, measured with a TDS conductometer), the reconstructed inhomogeneity was non-conductive. The three-dimensional cross-section comprises the vertical expansion; this effect was expectable, as the 3D reconstruction process utilizes only one level of electrodes, and the object then extends beyond the scanning plane [91].

The imaginary part of the admittivity is represented in Fig. 3.21b and 3.21d, where the three-dimensional cross-section resembles that characterizing the conductivity. Thus, the imaginary component too exhibits a major vertical expansion,

mainly due to the actual concept of the experiment. In view of the reconstruction results, the object can be described as weakly capacitive (see the red band). The cross-section at the electrode level (Fig. 3.21d) contains weakly inductive areas represented by blue patterns; these elements arise from the measurement error. In addition, the resulting cross-section includes a randomly distributed capacitive area near the original position of the object; generally, this capacitive region appears to be shapeless, meaning that its form does not entirely match that of the inserted cylinder. Such an error is most probably caused by the small phase difference between the measured phase values of the homogeneous and the inhomogeneous states on the one hand and the character of the graduated cylinder, which acts as an insulator, on the other. Another factor probably rests in the non-shielded cables that connected the tomograph and multiplexer [91].

The reconstructed cross-sectional images were defined at the electrode level and then evaluated by using the Jaccard index and the mean absolute value. The Jaccard index characterized the location of the inhomogeneity. In the specific conductivity, the values of the index and the mean square error equaled 0.8498 and 1902.5, respectively, while those of the imaginary component corresponded to 0.5837; 8994.7 [91].

The experiment showed that the PLI system is suitable for data acquisition in EIT. Despite such an outcome, the device can still be improved in terms of, for example, the shielded cables and active electrodes. Furthermore, the overall results also revealed that the conductivity has a major impact on determining the position and approximate size of the object. By comparison, the imaginary component does not possess such a capability, meaning that it cannot provide enough position-related information; this deficiency stems from several factors, including but not limited to the amplitude and frequency of the excitation current and the different electrical properties of the medium and the inserted cylinder. Such factors cause the phase between the injected current and the measured voltage to be almost unmeasurable, making the reconstruction of the imaginary part very problematic [91].

The sensing sequence, involving 40 voltage values, took approximately 90 seconds. The most time-consuming activity lay in the measurement performed with the applied laboratory devices (2 seconds per value). In the 16-electrode configuration, which we had not used practically, the assumed data acquisition time reached approximately 500 - 550 s. Thus, by contrast to the manual cycle characterized within the Preliminary results, chapter A, the time to obtain the data was theoretically reduced from 3 hours to less than 10 minutes, improving the process significantly.

To enable the discussed experiment, we utilized the following hardware:

- PLI EIT version 0.1 (multiplexer, VCCS);
- Agilent 33220A function waveform generator;
 - voltage range: 10 mV_{pp} to 10 V_{pp};
 - voltage uncertainty: $\pm 1\%$ of range + 1 mV_{pp};
 - frequency resolution: 1 μ Hz;
 - frequency range: 1 μ Hz to 20 MHz;
- Keysight 34450A 5½digit multimeter;
 - input impedance 1 M Ω \pm 2 % + 100 pF;
 - frequency measurement range: 20 Hz to 100 kHz;
 - AC measurement accuracy of 0.2 % from the measured value + 0.1 % of the range;
- Agilent DSO-X 3014A four channel oscilloscope;
 - sampling frequency 4 GSa/s;
 - cut-off frequency 100 MHz;
 - horizontal resolution 2.5 ps;
 - measurement accuracy (2 % + 0.5 %) of the range;
 - input impedance 1 M Ω \pm 1 % + 14 pF.

3.3 Error exploration in the open and closed domains

A correct mesh model is of fundamental importance in EIT imaging because all the calculations are performed via the FEM. The main challenge lies in selecting elements sufficiently small to recover the original conductivity but not excessively tiny to rapidly increase the computational cost. The error estimation over the mesh element size constitutes, together with the computational time, a major factor in designing the domain and the imaging procedures. For this reason, we evaluated the *a posteriori* convergence of the imaging algorithms; the mesh element size; and the computational effort for the open and the closed domains.

This section explores the convergence of the measurement error with respect to the mesh scale to obtain the limits where the additional mesh did not compensate for the time spent. The relevant analysis was performed by using EIDORS, which comprises the Gauss-Newton algorithm and regularizations. The error was evaluated via a minimum mean square error, a sum squared error, and the Jaccard distance [92].

To carry out the analysis, we used an original and a reconstructed images, quantizing the original image into an unstructured “fine” mesh to obtain an accurate forward solution. To avoid an *inverse crime* (section 1.5), we conducted the reconstruction on an unstructured “coarse” mesh refined near the electrodes and boundaries. The “fine” and “coarse” meshes were quantized into a regular mesh by means of standard interpolation methods to prepare the same data structure for evaluation through the selected error methodology. The convergence was examined in both the closed domains, where the electrodes had been placed equidistantly on the domain boundaries (Fig. 3.22), and the open ones, with the electrode placement similarly regular but the boundaries extended to infinity; the latter arrangement is found in, e. g., geophysical or subsurface exploration (Fig. 3.23) [92, 93].

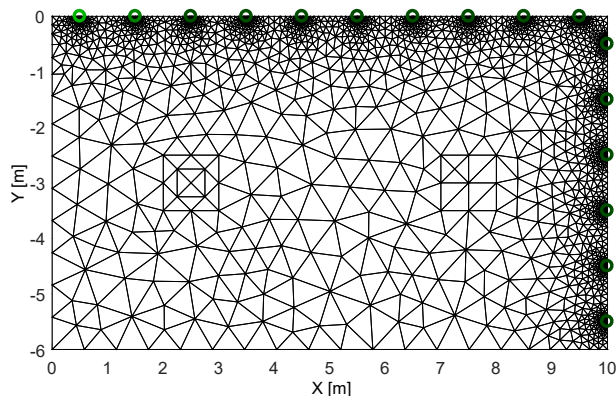


Fig. 3.22: The unstructured mesh for the closed domain, including the point electrodes and two square subspaces to accommodate the inhomogeneities [92, 93].

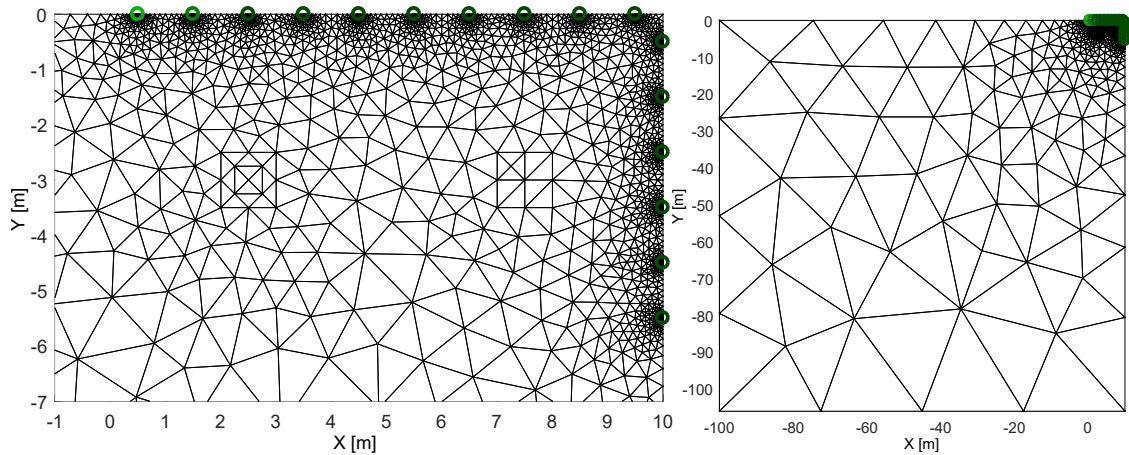


Fig. 3.23: The unstructured open domain mesh. The left-hand image shows a detail of the domain; this detail corresponds to the closed domain. On the right-hand side, we display a domain extension with the side length 10 times greater than in the closed domain [92, 93].

Generally, the EIT imaging procedure comprises several sources of errors, such as the measurement process and the definition of the model. More concretely, the errors occur in the discretization of the space generated by the selected mesh or during the computation; in the latter case, the error arises from the methods of the non-linear forward and inverse tasks. An example of the discretization error is shown in Fig. 3.24 [92].

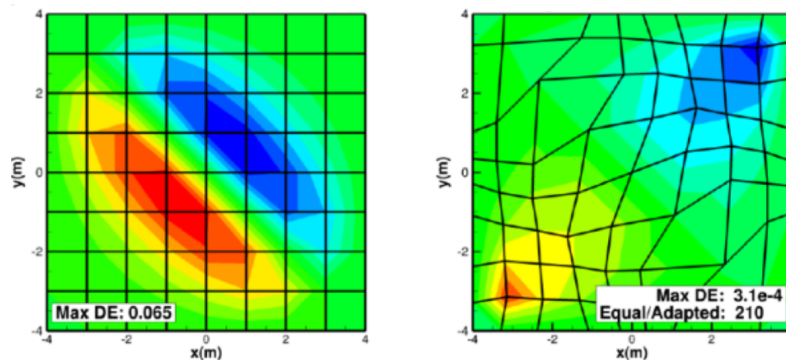


Fig. 3.24: An example of the discretization error differences between a regular and an "ugly" optimized adaptive mesh [94].

The mesh quality affects the convergence and stability, which determine the simulation error in the forward solution. Another relevant factor then consists in comparing the real problem data with the simulation results (Fig. 3.24). In the two images above, the main difference is between a regular square mesh and a deformed mesh with an adaptive algorithm. In the former case, the discretization error was

higher than in the latter one [94]. Based on this example, it is possible to claim that the quality of the mesh cannot be evaluated only from the geometry, and the following factors have to be considered:

- overlapping the volumes and surfaces;
- sizes of the elements and their comparison;
- element surfaces on the borders of the explored domain;
- critical parts of the mesh, such as sharp corners;
- similarity between the surfaces of the mesh and the tested domain.

To evaluate the convergence error, we designed the procedure in Fig. 3.25, with the domains generated by using EIDORS and a compatible GMSH tool [92].

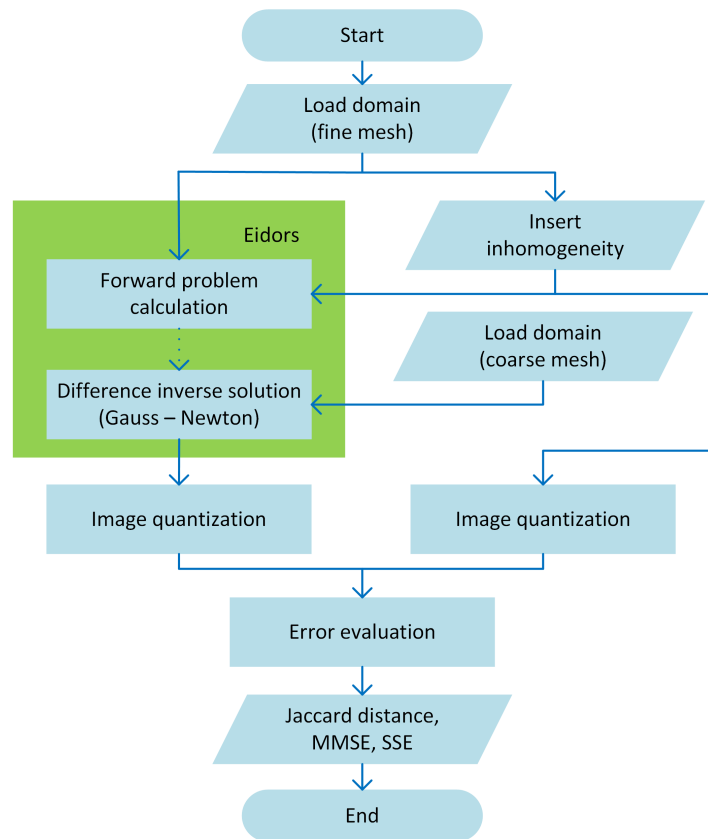


Fig. 3.25: The individual stages in evaluating the domains [92].

In the initial phase, we generated an unstructured fine mesh to constitute the original domain. This domain was processed via the forward task to obtain the data of the homogeneous medium. After completing the computation, we inserted an inhomogeneity into the original domain and calculated the inhomogeneous data. These operations were performed separately because we employed a difference inverse solver to carry out the reconstruction. To avoid an inverse crime, we prepared a coarse mesh. The models were then adapted to the requirements of the

EIDORS tool, which allowed us to apply the Gauss-Newton method expanded with the Laplace, NOSER, and Tikhonov regularizations; thus, we obtained the results that facilitated a comparison of the algorithms. The reconstructed and the original domains were quantized and saved as an image having a regular grid. The results were evaluated by means of the selected error functions, namely, the Jaccard distance, the sum of squared errors (SSE), and the minimum mean square error (MMSE). This error methodology had been employed to compare the algorithms in the experiment [92].

Before the simulation, we fixed the forward solver and random noise for all the domains and methods to ensure comparable results. This step enabled us to yield from the forward solution one and the same sequence of voltage values. The closed domain mesh covered the range of 62 to 20,408 elements, and the open domain encompassed 160 to 19,958 elements. Examples of the closed and the open domain designs with inserted inhomogeneities and reconstructed conductivities are shown in Fig. 3.26 [92].

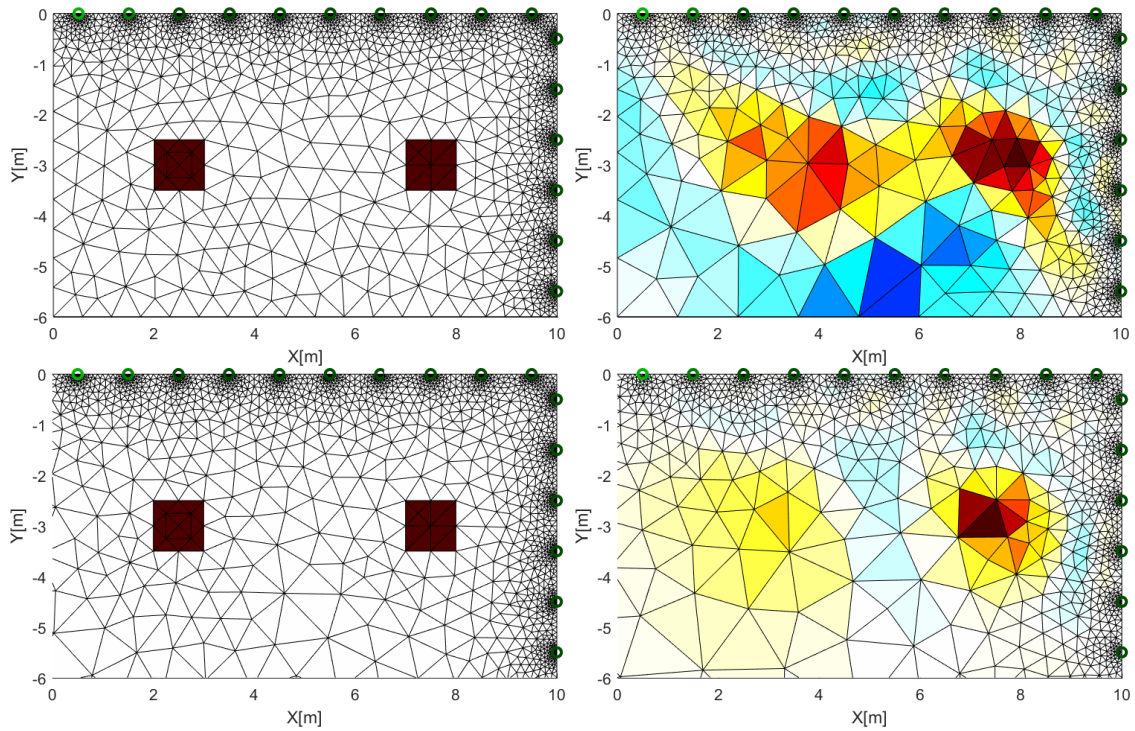


Fig. 3.26: The reconstruction in the closed (top) and the open (bottom; zoomed to detail at the regions of interest) domains, executed via the Gauss-Newton method including the Tikhonov penalty. The left-hand column shows the original closed and open domains (4,463 and 4,734 elements) with inserted inhomogeneities; the right-hand column then presents an inverse image computed on a mesh of 3,433 and 2,712 items relating to the closed and the open domains, respectively [92].

The relationship between the computational time and the mesh element scale with respect to the Gauss-Newton method and the different regularizations, observed in both the open and the closed domains, is illustrated in Fig. 3.27.

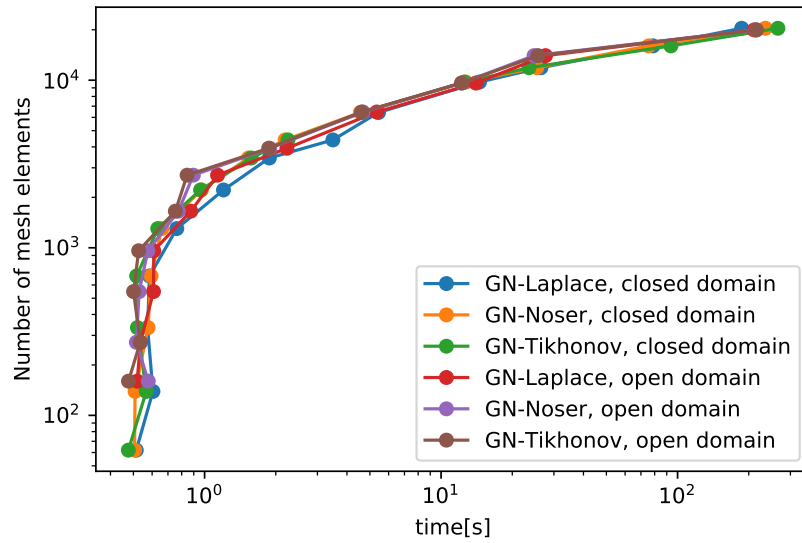


Fig. 3.27: The relationship between the number of mesh elements and the computational time in the selected reconstruction methods [92].

As is shown in Fig. 3.27, the applied regularization technique does not have a significant impact on the computational intensity. The difference between the open and the closed domain models was almost negligible. Based on these results, the selected regularization and the mesh design appear to be stable for the purposes of the Gauss-Newton inversion. By extension, the image above also relates the convergence behavior of the inversion to the increasing number of elements and mesh complexity given by the specific hardware. The actual convergence estimation normalized into the range of 0 to 1 is shown in Fig. 3.28. The detailed absolute values of the individual error metrics are presented in Tab. 3.10 [92].

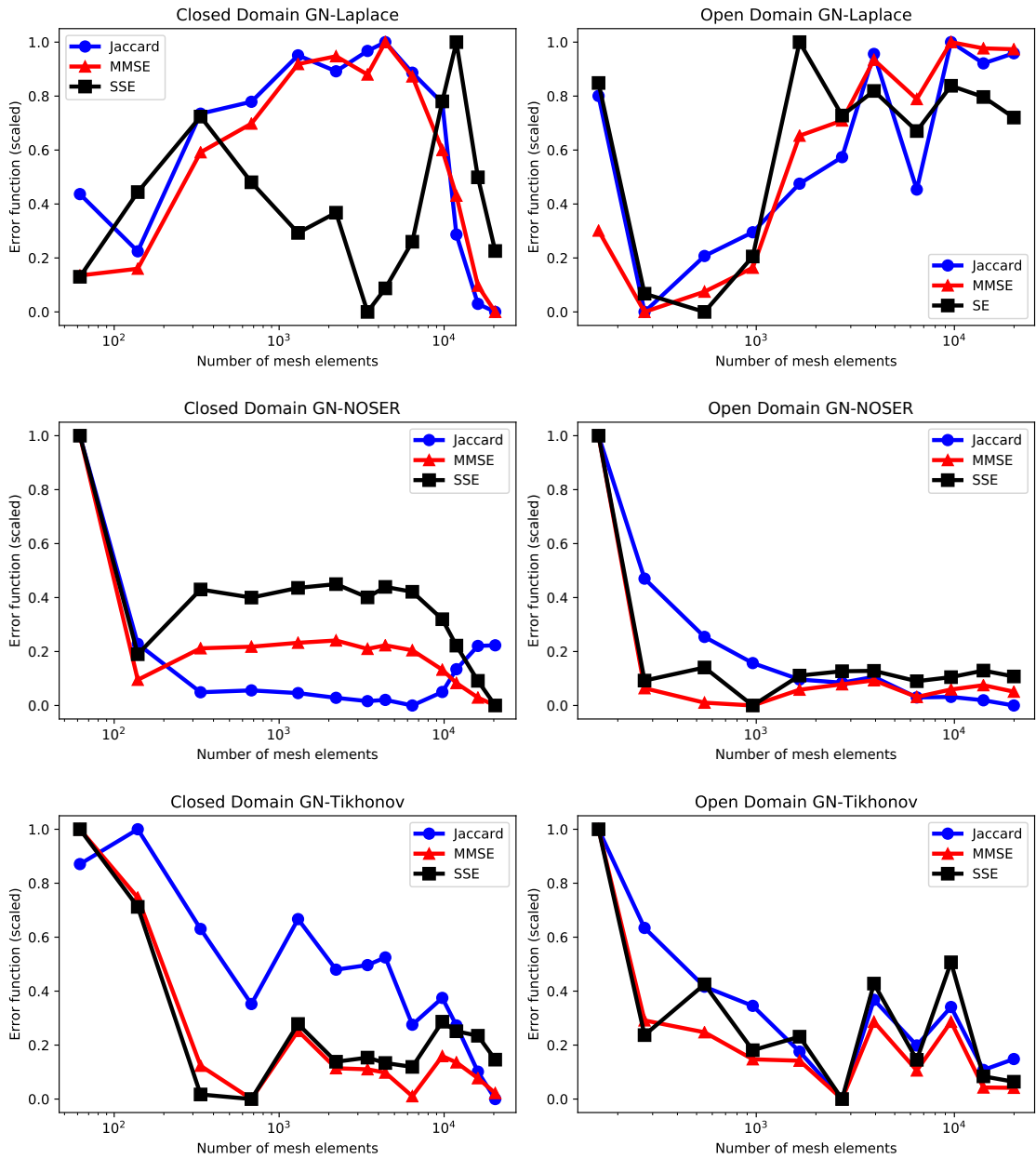


Fig. 3.28: The error convergence estimates normalized in the range of 0 to 1, characterizing the closed (left-hand column) and the open (right-hand column) domains and considering the numbers of mesh elements and regularizations [92].

Tab. 3.10: The Jaccard distance, MMSE, and SSE: The values over the mesh element scale provided by the selected regularization methods [92].

Closed domain									
Elements	Tikhonov			NOSER			Laplace		
N	Jacc	MMSE	SSE	Jacc	MMSE	SSE	Jacc	MMSE	SSE
62	0.463	0.113	658.97	0.596	0.160	768.53	0.625	0.230	1046.84
139	0.489	0.092	542.65	0.478	0.067	465.75	0.607	0.232	1080.25
334	0.415	0.040	261.70	0.451	0.079	555.48	0.650	0.259	1110.02
679	0.358	0.029	254.81	0.452	0.080	544.24	0.654	0.265	1084.12
1302	0.422	0.050	367.28	0.450	0.081	557.67	0.668	0.279	1064.15
2213	0.384	0.039	310.75	0.447	0.082	562.88	0.663	0.281	1072.11
3433	0.387	0.038	316.86	0.446	0.079	544.52	0.670	0.276	1032.98
4401	0.393	0.037	308.84	0.446	0.080	559.04	0.672	0.284	1042.27
6417	0.343	0.030	302.96	0.443	0.078	552.26	0.663	0.276	1060.65
9750	0.363	0.043	370.67	0.451	0.071	514.26	0.653	0.259	1116.03
11871	0.342	0.041	356.35	0.464	0.066	477.68	0.612	0.249	1139.40
16026	0.307	0.036	349.64	0.477	0.060	428.87	0.591	0.228	1086.07
20408	0.287	0.031	313.84	0.477	0.057	394.73	0.588	0.222	1057.01
Open domain									
Elements	Tikhonov			NOSER			Laplace		
N	Jacc	MMSE	SSE	Jacc	MMSE	SSE	Jacc	MMSE	SSE
160	0.511	0.1277	746.31	0.538	0.1361	835.74	0.616	0.216	1023.85
273	0.429	0.0581	444.93	0.493	0.0854	602.63	0.589	0.192	947.74
548	0.380	0.0538	519.32	0.474	0.0825	615.08	0.596	0.198	941.17
960	0.364	0.0439	422.84	0.466	0.0819	578.91	0.599	0.205	961.19
1654	0.325	0.0434	442.59	0.461	0.0851	607.38	0.605	0.244	1038.60
2712	0.286	0.0294	351.31	0.460	0.0862	611.53	0.609	0.248	1012.10
3926	0.369	0.0576	520.35	0.462	0.0870	611.87	0.622	0.266	1020.97
6460	0.330	0.0398	408.75	0.455	0.0836	602.03	0.605	0.254	1006.50
9616	0.363	0.0576	551.52	0.455	0.0851	605.90	0.623	0.271	1022.84
14012	0.310	0.0336	384.59	0.454	0.0860	612.13	0.620	0.269	1018.79
19958	0.319	0.0335	376.65	0.453	0.0847	606.54	0.622	0.269	1011.36

Closed domain: Jaccard

The pattern of the Jaccard distance over the mesh element scale in the closed domain secured the best stability for NOSER. The Jaccard distance increased slightly with the rising number of elements. Compared to NOSER, the Tikhonov method exhibited the smallest absolute value of the Jaccard distance; the dispersion was nevertheless higher. The Jaccard distance decreased over the generated set of meshes. The Laplace regularization yielded the smallest similarity of the images, meaning that the Jaccard distance produced the highest one. All of these methods then exhibited markedly higher error rates at low numbers of elements, due to an insufficient amount of the elements and, thus, their excessive sizes. The methods delivered a satisfactory stability over the mesh scale [92].

Closed domain: MMSE

The variation of the MMSE over the mesh element scale in a normalized manner is shown in Fig. 3.28, and the absolute value of the error is presented in Tab. 3.10. According to the results, the MMSE decreased significantly in Tikhonov and NOSER but remained stable in Laplace. With NOSER, we obtained the best stability over the tested meshes. The Tikhonov method exhibited a relatively high error variation over the mesh element scale, performing somewhat worse than NOSER in stability terms. The Tikhonov regularization gave the smallest absolute error value in the explored range, but the error rate markedly depended on the mesh. The Laplace technique showed a stable growth of the MMSE up to the limit of 8,000 elements; after that, the rate decreased sharply [92].

Closed domain: SSE

The last technique employed in evaluating the closed domain was sum squared error (SSE). As indicated in Tab. 3.10, the SSE value decreased rapidly when the limit of 500 elements had been reached in the Tikhonov and the NOSER options. By comparison, the Laplace grew slightly. The NOSER tool provided a good stability between 500 to 8,000 elements; beyond the latter limit, the error started to decrease. In the Tikhonov regularization, the computed SSE was relatively unstable, involving significant variation; within the given range (500 to 8,000), however, the absolute value was smaller than that delivered by NOSER. The Laplace procedure exhibited the highest absolute SSE value, ensuring a stability inferior to that obtained from the Tikhonov method [92].

Open domain: Jaccard

The pattern of the Jaccard distance over the mesh element scale in the open domain is shown in Fig. 3.28 (the right-hand column). During the initial phase, the

Jaccard distance decreased in all of the methods. At the limit of 200 elements, the Jaccard distance began to increase in a stable manner, while Tikhonov and NOSER remained low. The smallest absolute value was determined in Tikhonov; the stability nevertheless worsened gradually in the band beyond 4,000 elements. By comparison, NOSER decreased slightly, from 0.5 to 0.45. The Laplace regularization delivered the highest Jaccard distance value. The best stability over the mesh element scale was then observed in NOSER [92].

Open domain: MMSE

In all of the methods, the MMSE exhibited a significant decrease with the rising amounts of elements, starting from the bottom limit of 160. At 300 items, the Laplace method began to grow in an irregular manner, eventually reaching 0.27 (Tab. 3.10); NOSER remained stable at around 0.08; and Tikhonov, while falling lower than NOSER, brought a comparatively volatile error value [92].

Open domain: SSE

The Tikhonov method exhibited the smallest SSE value but, similarly to the MMSE, was not sufficiently stable; by comparison, NOSER delivered a slightly higher SSE rate but ensured a very good stability. The Laplace regularization produced the highest error value and sharp variations. Each of the verified methods contained a peak at approx. 200 elements, probably due to the discretization [92].

Summary

In the closed domains, the optimum range to enable the Tikhonov inversion was identified between 500 and 1,000 elements; here, the Jaccard distance, MMSE, and SSE achieved the best results in terms of the computational intensity. Generally, in the same context, NOSER proved to be more stable and suitable for a wider range of mesh element scales, albeit only at the cost of a decreased quality of the inverse image. The Laplace regularization then delivered the worst results. As regards the open domain, the most convenient method was Tikhonov, especially if employed in the area of 2,700 elements, where it ensured acceptable computational intensity. A good compromise lay with NOSER: This algorithm offered a stability markedly better than Tikhonov's and operated in a wider range of selected meshes, but the inversion accuracy did not match the results delivered by Tikhonov in this respect. In the Laplace method, we observed a high variation of the normalized error scale, and, by extension, the highest absolute value [92].

The discussed experiment was calculated on a standard computer with an Intel Core i3-6089P 3.60 GHz processor and 4 GB RAM. The software, i.e., the EIDORS tool and GMSH mesh generator, ran on OS Win 10 x64, under Matlab R2016a [92].

3.4 Parallelization

One of the most prominent challenges in EIT imaging lies in reducing the computational intensity of the final solution. This task can be accomplished with, for example, the approaches for shortening the reconstruction time that were discussed in the theoretical part. At the beginning of this chapter, we characterize the CPU-based processing of the inverse problem by using Tikhonov regularization. The relevant algorithm was designed by Vauhkonen in Matlab [95], and its flowchart is graphically presented below.

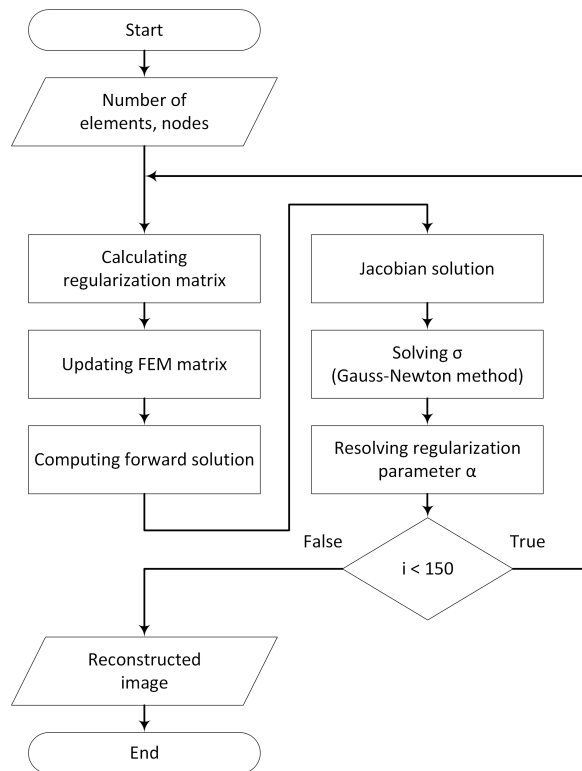


Fig. 3.29: The flowchart of the forward and the inverse tasks [96].

Fig. 3.29 characterizes the individual functional software blocks that allow us to reconstruct the original image. The introductory stage of the computation involves a data input derived from the characteristics of the domain mesh; the relevant parameters include the coordinates, the number of elements, and the count of nodes. When the mesh parameters have been specified, we set the initial conductivity and select the elements that determine the inhomogeneity. After that, the conductivity and voltage values are computed via the forward solution supported by the FEM. In addition to the forward task, we calculate the Tikhonov regularization matrix. The Update FEM matrix function processes the boundary voltage values on the electrodes to produce the vector $U_{\text{FEM}}(\sigma)$ representing the conductivity values at the

nodes of the mesh. Subsequently, we compute the Jacobian, which is then substituted in the Gauss-Newton method. This entire step yields the conductivity vector for the given iteration of the procedure. At the end of the cycle, the regularization parameter α is reduced. The actual computation is limited to 150 iterations [96].

In our case, the first procedural phase involved computing the Jacobian, a precondition for running the Gauss-Newton iteration method; the reason rested in that the Jacobian generally embodies the most time-consuming part of the calculation. At the next stage, we replaced the sequential CPU code in the parallel solution via the CUDA function, which was then processed by the GPU. The difference between the full and the partial implementations of the CPU and the GPU, respectively, is shown in Fig. 3.30 [96].

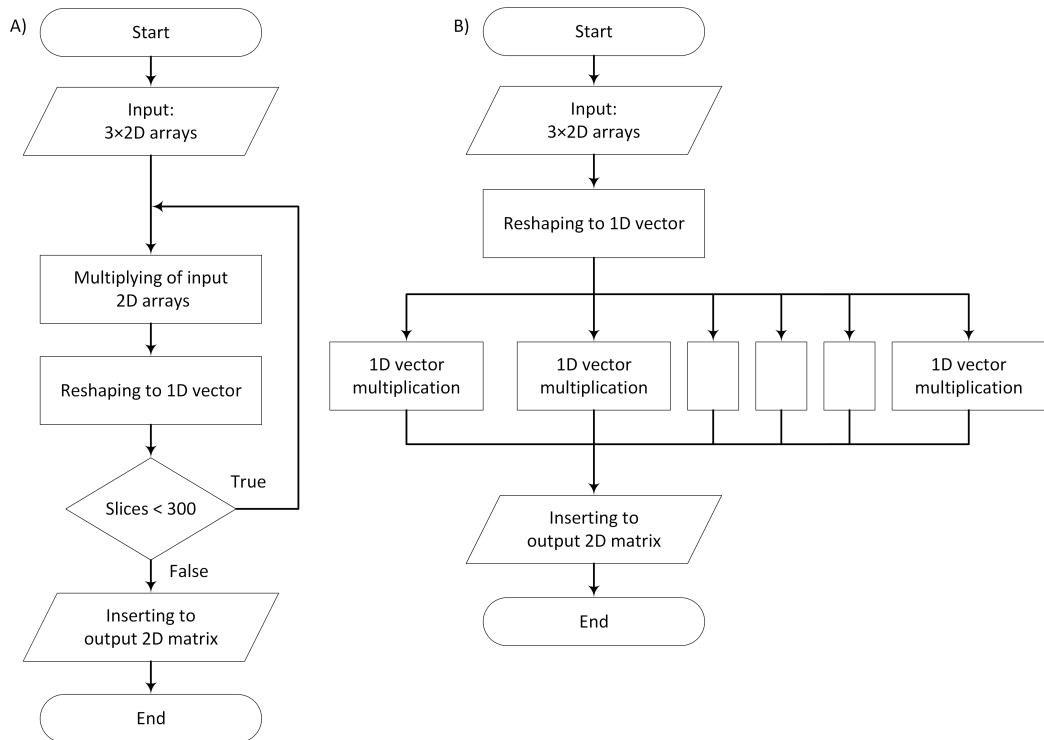


Fig. 3.30: The flowcharts of the A) sequential and B) the parallel implementations of the Jacobian [96].

As is indicated, the input data of the Jacobian consist of three matrices; their original embodiments are computed vectorally and sequentially in Matlab. All of the matrix multiplications were implemented in a for-loop, whose properties had followed from the sizes of the matrices. Compared to the sequential approach, the novel parallelized technique relies on separating the matrix into vectors; these vectors are then multiplied in parallel via 300 threads in the GPU. The resulting matrix is concatenated from the individual threads to form the original dimension of 240×300 elements. Thus, we obtain a matrix identical with that solved in the

sequential processing. The relevant computational time intensity rates are compared in Tab. 3.11. The resulting values show that the parallel processing is approximately twenty times faster than the sequential approach [96].

Tab. 3.11: Comparing the Jacobian computing procedures [96].

Hardware	Time [ms]
CPU: Intel Core i5-4460 (3.2 GHz; x64; 8 GB RAM)	5
GPU: NVIDIA GTX 970 (1.215 GHz; memory 4 GB)	0.25

Based on the results specified above, we decided to run the whole EIT image reconstruction process on a CUDA platform to reduce the time cost. In the inverse task, multiple computations of the forward task are invariably required. The most time-consuming stage of the image reconstruction then lies in evaluating the Jacobian, a step that we successfully implemented in the previous phase, for which we had selected the well-known Gauss-Newton approach including the Tikhonov penalty. The CPU and GPU-based options are visualized in Fig. 3.31 [97].

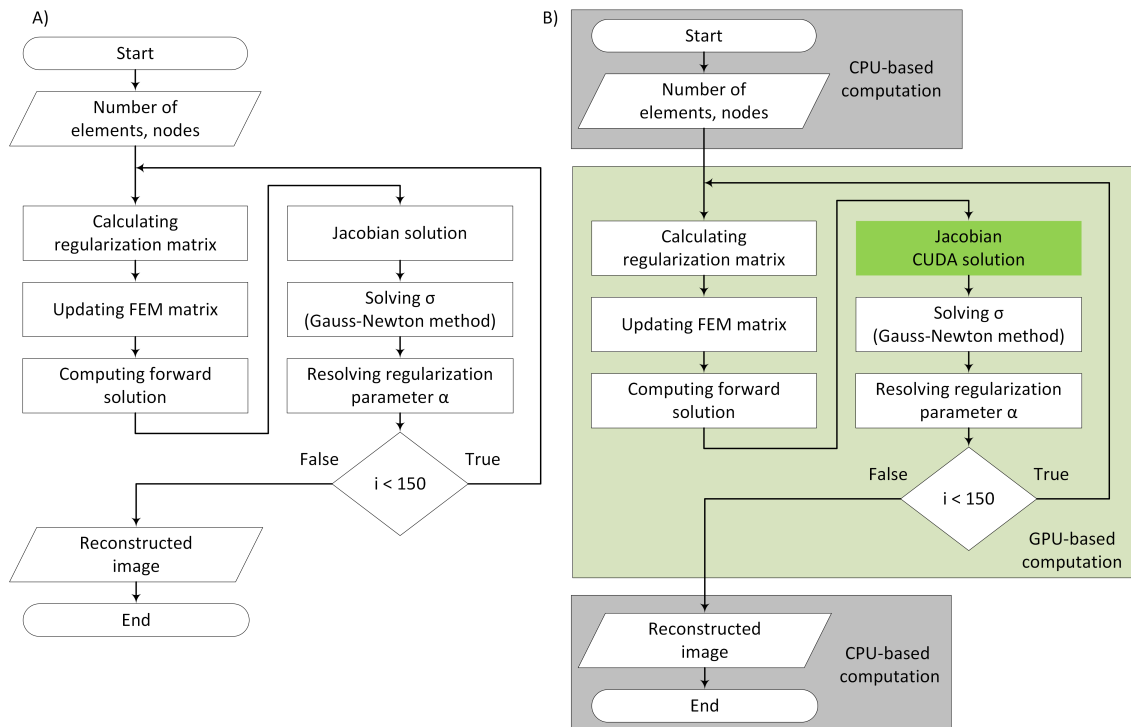


Fig. 3.31: The flowcharts of the differently processed forward and inverse tasks [97].

The images in the same figure also visualize the GPU-based implementation of the inner computation loop. This loop comprises the following procedures: *calculating the regularization matrix; updating the FEM matrix; computing the forward solution; calculating the Jacobian; solving the conductivity via the Gauss-Newton*

method; and resolving the regularization parameter α . In our experiments, this type of implementation required the initialization to be corrected where the data had been relocated between the RAM and the VRAM [97].

The parallelized code contains the whole process, except for the *symamd* function; this function computes a symmetric definite matrix. Disadvantageously in this context, however, Matlab does not have an equivalent feature utilizing GPU support. The additional data transfer between the RAM and the VRAM increases the time intensity, as determined through relevant testing and evaluated for each part of the algorithm. The actual intensity values are compared in Tab. 3.12 [97].

Tab. 3.12: The computational times in the individual reconstruction steps: the CPU- and GPU-based procedures [97].

Process	CPU time [ms]	GPU time [ms]
Calculating the regularization matrix	1.6	1.3
Updating the FEM matrix	4.3	0.9
Forward solution	0.7	6.0
Computing the Jacobian	20.6	0.1
Solving σ with the Gauss-Newton method	1.6	7.5
Total time per iteration	28.8	15.8

As indicated, the GPU option is superior in terms of the total time per iteration. The properties, performances, and impacts of the processes can then be characterized in the following manner: *calculating the regularization matrix* slightly reduced the overall time consumption by multiplying the one-dimensional vector and the regularization matrix; *updating the FEM matrix* proved to be faster, and greater differences are assumable at increasing numbers of elements; *forward solution* significantly slowed down in the parallel processing, the reason being the RAM - VRAM data transfer, whose speed was hampered by the *symamd* function running; the CUDA-based code of the *Jacobian* was computed very effectively, at a pace almost two hundred times quicker than that of the original CPU processing; and *solving σ with the Gauss-Newton method* significantly increased the computational intensity, due to the matrix division to compute the system of linear equations $\mathbf{Ax} = \mathbf{b}$. The sequential behavior of the system of linear equations embodied the factor that had most prominently decelerated the GPU-based implementation [97].

The hardware and software components included an Intel Core i5-4460 CPU (3.2 GHz; x64; 8 GB RAM), an NVIDIA GTX 970 GPU (1.215 GHz; memory 4 GB), Windows 10 (version x64), and Matlab R2016a.

Discussion

Preliminary results

The preliminary results outlined in the Appendix capture the experimental measurement and reconstruction of the two material combinations, clay \times sand and water \times glass. The conductivity distribution images were obtained via the Gauss-Newton method including the Tikhonov penalty term. In the case of the soil sample, the clay was located slightly below the center, Fig. A.1b. The other type of measurement, namely, the arrangement with water encompassing a glass cylinder, showed that the conductivity distribution reflects the original position of the object better than the reconstructed permittivity. A similar experiment, utilizing modified electrical impedance spectrometry [98], was performed by means of a Z-meter [76]. The researchers employed the common two-wire connection approach to the feeding and sensing, and the presented outcomes are thus affected by error due to the contact impedance between the electrodes and the analyzed material. Moreover, the resulting conductivity maps were created only via simple graphical representation of the measured cross-electrode impedance values, exploiting the Surfer 8 software, and the authors did not solve the inverse task to estimate the conductivity maps as accurately as possible. The outcomes were used to predict the positions of unknown objects in the heterogeneous environments. The actual data collection was performed within project FAST/FEKT-J-18-5385 [99, 100].

Optimization

The applied optimization procedure can reduce the image reconstruction uncertainty in three different ways, depending on the choice. The first step rests in evaluating the initial conductivity from the sequence of measured voltages. For this reason, we prepared a corresponding cylindrical FEM model containing approximately 15,000 elements and 8 electrodes. The initial conductivity value reached between 53.7 and 54.9 mS/m. The designed procedure converges very fast and, with the computer and experiment employed in this thesis [81], takes 7 s at the maximum.

In addition, the proposed approach also facilitates calculating the boundary deformation of the elliptical domain, considering the dimensions of the $\{X, Y\}$ axes. The designed procedure was verified on real data acquired from a laboratory tomograph deformed with a clamp. By optimizing the shape deformation, we yielded the centimeter lengths of $\{18.62, 19.35\}$ and $\{18.66, 19.35\}$ in adjacent and opposite driving, respectively. In the real axial dimensions of $X = 18.6$ cm and $Y = 19.4$ cm, our approach delivered acceptable results (the relative axis value errors amounted to $\{0.31\%$, -0.25%). The impact of an inaccurately modeled shape was also demonstrated on an image reconstruction involving wrongly constructed circular and true

elliptical domain shapes, where the relative root-mean-square error dropped by 6.2 % and 11.6 % in the adjacent and the opposite current patterns, respectively [81].

The optimization also allowed evaluating the electrode position on the domain boundary. For this reason, we prepared a model containing a shifted 6th electrode, which was then monitored with the adjacent and the opposite patterns. The optimization produced suitable results in the adjacent measurement and a non-acceptable duality in the opposite sensing strategy. The duality had arisen from the two possible electrode placement options (the shifted 2nd and 6th electrodes), where the forward solver provided a sequence with the same, interchangeable voltage values (Fig. 3.11). Thus, we present the impact of an electrode misplacement only on the adjacent pattern, via inverse images (Fig. 3.12) of the inaccurate and the correct models. The optimization reduced the relative root-mean-square error by 12.7 %; the inhomogeneity localization was significantly improved too, from a mismatch to the Dice similarity of 0.667 [81].

The procedure was implemented by using the Matlab Optimization toolbox, the EIDORS tool, and the Netgen mesh generator. Overall, the approach is suitable for adjusting the unknown parameters of the real laboratory model to create a corresponding numerical model that will enable precise image reconstruction. The current limitations rest in that only one parameter is solvable per run and that the computational intensity markedly increases due to the rising number of degrees of freedom being computed simultaneously. The optimization design is universal and yields a potential to include another parameter, such as contact impedance [81].

Newly proposed system

Accelerating the data acquisition process in laboratory and other in- and out-door conditions is based on identifying and exploring a device for automatized data collection. The first step to reach this goal lies in specifying the key parameters of such a device. To reduce the time to obtain the tomographic data of the laboratory model, we proposed a setup comprising a multiplexer, a voltage-controlled current source, and a microcontroller-regulated circuit to operate the feeding and the sensing branches. The multiplexer was materialized in a discrete manner, utilizing a shift register connected into a combination of photorelays with a low on-state resistance (lower than 1 Ω). The VCCS was built on a multirange Howland current pump. This design enabled us to control the injection current either through the amplitude of the input voltage or manually, by switching the resistors placed before the voltage follower. The presented multiplexer and VCCS were verified via an experimental measurement on a laboratory tomograph that allowed the actual image reconstruction. The results showed that the assembled device is suitable for obtaining EIT imaging data. The setup facilitated research into the optimization procedure and

reduced the time required to obtain the tomographic data from hours to minutes. The device for effective data acquisition in EIT (a precise, low impedance EIT system) is being refined within diverse Bachelor's projects supervised by the author of this thesis [88, 90, 91].

Error exploration in the open and the closed domains

The experiment centered on designing the open and the closed domains was performed by using EIDORS library, which contained different regularizations, namely, Tikhonov, NOSER, and Laplace. To explore the errors, we generated domain meshes consisting of 62 to 20,408 elements. The computational time for the specified mesh element scale remained stable (0.4 s - 0.5 s) between 60 and 1,000 elements but then began to rise (0.5 s to 300 s), with a gradual increase in the number of elements from 1,000 to 20,000 [92].

The reconstructions for the domains were performed by utilizing the results of the *a priori* calculated forward solution and the fixed random seed facilitating the noise data generation. The Jaccard distance, minimum mean square error, and sum squared error were selected to evaluate the inverse images. The results of the designed simulation process relating to the above-mentioned regularization approaches are summarized in Tab. 3.13.

Tab. 3.13: The regularization approaches compared in terms of the Jaccard distance, MMSE, and SSE over the mesh element scale.

Regularization	Jaccard distance	MMSE	SSE	Mesh element range
Tikhonov	0.30 - 0.40	0.03 - 0.06	300 - 550	2,000 - 16,000
NOSER	0.44 - 0.48	0.06 - 0.09	400 - 600	500 - 20,000
Laplace	0.60 - 0.65	0.19 - 0.28	950 - 1,150	60 - 20,000

The table presents the Tikhonov method as the one with the smallest values of the error metrics; the stability, however, was not perfect. A good alternative to the Tikhonov option was found in NOSER, whose capabilities ensured an enhanced stability at a wider scale of mesh elements. This tool nevertheless also produced a slightly higher error than the Tikhonov procedure. Considering the selected techniques, the worst results were delivered by the Laplace term; the reason apparently lies in that the output depends on the *a priori* conductivity information, which had not been involved in the experiment. Such conditions then yielded amplified noise and decreasing solution stability in the Laplace regularization [92].

In terms of the computational effort (approximately 0.5 s), the best area for the image reconstruction involving the close domains was identified in the vicinity of 800 elements. The open domain model provided the best results in the range of

2,600 to 3,000 elements, considering the inverse image quality and time consumption (between 1 s and 2 s). The experiment was performed on a standard personal computer, described in detail at the end of section 3.3 [92].

Parallelizing the algorithms

The parallelization of the algorithm created by Vauhkonen [95] indicates that the GPU-based implementation is positively faster than the original sequential Matlab code. To compare these two options, we employed a FEM model containing 300 elements, 167 nodes, and 16 electrodes. The experiment was carried out by applying trigonometric driving and the injection current of 1 mA. The final computational time reached 28.8 s and 15.8 s in the CPU and the GPU-based variants, respectively. The most significant improvement in the inverse task processing was eventually achieved in the Jacobian, with the time intensity falling from 20.6 s to 0.1 s. The individual procedural steps had comprised functions not supported by the GPU processing, and these slowed down the computation. In the given context, the forward solution proved to be hampered by the data transfer between the RAM and the VRAM, namely, the unsupported *symamd* function, and solving the conductivity of the Gauss-Newton iteration appeared problematic due to the matrix division performed during the solution of the system of linear equations. Further exploration generated the possibility of another decrease in the computational effort; the potential to reduce this factor lies in the GPU implementation of the unsupported *symamd* function [96, 97].

Conclusion

The results outlined in the thesis, the Discussion chapter in particular, contribute significantly to EIT research worldwide, especially by

- **decreasing the uncertainty of the reconstructed conductivity distribution via optimizing the mathematical model through a set of laboratory measurements [80, 81];**
- **accelerating the data acquisition in laboratory and other in- and outdoor conditions [88, 90, 91];**
- **optimizing the parameters of the closed and the open domain models (mesh density, computational effort, and analysis of the convergence error) [92, 93];**
- **improving the time intensity of the image reconstruction via parallelizing the individual algorithm steps [93, 96, 97].**

The central target fields and activities comprise, above all, multidisciplinary provinces such as geophysical mapping and exploration, laboratory equipment design and testing, and the optimization or analysis of multiparametric models to reduce the uncertainty in reconstructed conductivities. The newly obtained concepts are applicable in automating data acquisition tasks and conducting diverse laboratory practicals at technical universities, inclusive of the specialized measurement and electromagnetic field modeling courses delivered at the Faculty of Electrical Engineering and Communication, Brno University of Technology.

The outcomes presented herein relate back to the author's internship at Netrix (NetArt) S.A. Research and Development Center, Lublin, Poland, and his participation in science seminars at University of Economics and Innovation in Lublin and at Warsaw University of Technology. By extension, the thesis contains the products of a project (junior grant FAST/FEKT-J-18-5385) executed in cooperation with the Department of Water Structures, Faculty of Civil Engineering, Brno University of Technology. The relevant research involved experimental measurement of inhomogeneities inserted in water and soil, and the findings were published in [99, 100].

The future efforts will be pursued in collaboration with the above-specified institutions, the target fields and activities being effective data sensing, exploration of the open domain models, application of neural networks to the EIT problem, and improvement of the existing optimization procedure to include the contact impedance parameter and a multiparametric model with irregular boundaries.

The results of the experiments were published in the MDPI Sensors journal (impact factor 3.275 (Q2) [81]), Elektrotechnik peer-reviewed journal [100], and international and national conference proceedings (Eureka [80, 90, 99], ICUMT [88], Mechatronika [91], IIPhDW [92, 97], EEICT [93], PIERS [96]).

Bibliography

- [1] LIONHEART, B. EIT for beginners [online]. 2014, 38. Available at: <http://www2.compute.dtu.dk/~pcha/HDtomo/DTUEIT.pdf>
- [2] HOLDER, D. S. *Electrical Impedance Tomography: Methods, History and Applications*. B.m.: CRC Press, 2004. ISBN 978-1-4200-3446-2.
- [3] BOVERMAN, G., T.-J. KAO, X. WANG, J. M. ASHE, D. M. DAVENPORT, and B. C. AMM. Detection of small bleeds in the brain with electrical impedance tomography. *Physiological Measurement* [online]. 2016, **37**(6), 727–750. ISSN 0967-3334. Available at: doi:10.1088/0967-3334/37/6/727
- [4] FRERICHS, I., Z. ZHAO, T. BECHER, P. ZABEL, N. WEILER, and B. VOGT. Regional lung function determined by electrical impedance tomography during bronchodilator reversibility testing in patients with asthma. *Physiological Measurement* [online]. 2016, **37**(6), 698–712. ISSN 0967-3334. Available at: doi:10.1088/0967-3334/37/6/698
- [5] HALLAJI, M., A. SEPPÄNEN, and M. POUR-GHAZ. Electrical impedance tomography-based sensing skin for quantitative imaging of damage in concrete. *Smart Materials and Structures* [online]. 2014, **23**(8), 085001. ISSN 0964-1726. Available at: doi:10.1088/0964-1726/23/8/085001
- [6] KOURUNEN, J., R. KÄYHKÖ, J. MATULA, J. KÄYHKÖ, M. VAUHKONEN, and L. M. HEIKKINEN. Imaging of mixing of two miscible liquids using electrical impedance tomography and linear impedance sensor. *Flow Measurement and Instrumentation* [online]. 2008, **19**(6), 391–396. ISSN 0955-5986. Available at: doi:10.1016/j.flowmeasinst.2008.07.002
- [7] RYMARCZYK, T., and P. ADAMKIEWICZ. Monitoring damage and dampness in flood embankment by electrical impedance tomography. *Informatyka, Automatyka, Pomiar w Gospodarce i Ochronie Środowiska* [online]. 2017, **7**(1), 59–62. ISSN 2391-6761. Available at: doi:10.5604/01.3001.0010.4584
- [8] LESPARRE, N., B. GRYCHTOL, D. GIBERT, J.-Ch. KOMOROWSKI, and A. ADLER. Cross-section electrical resistance tomography of La Soufrière of Guadeloupe lava dome. *Geophysical Journal International* [online]. 2014, **197**(3), 1516–1526. ISSN 0956-540X. Available at: doi:10.1093/gji/ggu104
- [9] BORCEA, L. Electrical impedance tomography. *Inverse Problems* [online]. 2002, **18**(6), R99–R136. ISSN 0266-5611. Available at: doi:10.1088/0266-5611/18/6/201

- [10] KŘÍŽ, T. *New optimization algorithms for a digital image reconstruction in EIT* [online]. 2015, 73. Doctor of Philosophy. Brno University of Technology. Available at: https://www.vutbr.cz/www_base/zav_prace_soubor_verejne.php?file_id=113762.
- [11] DĚDKOVÁ, J. *Image reconstruction methods based on electrical impedance tomography*. VUTIUM, 2007. Profesor. Brno University of Technology. ISBN 978-80-214-3384-7.
- [12] BORSIĆ, A. *Regularisation Methods for Imaging from Electrical Measurements* [online]. 2002. Doctor of Philosophy. School of Engineering Oxford Brookes University. Available at: <https://radar.brookes.ac.uk/radar/file/4837c97a-d3ff-4521-a1df-f32a378534d2/1/borsic2002regularisationRADAR.pdf>.
- [13] BOYLE, A. J. S. *Geophysical Applications of Electrical Impedance Tomography* [online]. B.m., 2016. Doctor of Philosophy. Carleton University. Available at: <https://curve.carleton.ca/8ba36b23-acc0-4ea6-bd6d-b1f98a1b462a>
- [14] POLYDORIDES, N. *Image reconstruction algorithms for soft-field tomography* [online]. 2002, 262. Doctor of Philosophy. University of Manchester Institute of Science and Technology. Available at: <http://vummath.ma.man.ac.uk/~b1/theses/npolydorides/thesnick.pdf>.
- [15] DĚDEK, L., and J. DĚDKOVÁ. *Elektromagnetismus*. Brno: VUTIUM, 2000. ISBN 978-80-214-1548-5.
- [16] SILVESTER, P.P., and R.L. FERRARI. *Finite elements for electrical engineers*. 2nd ed. Cambridge: Cambridge University Press, 1990. ISBN 05-213-7219-4.
- [17] DALÍK, J. *Numerické metody* [online]. 2013. Brno University of Technology. Available at: https://math.fce.vutbr.cz/vyuka/podpora/NMII_2013.pdf
- [18] BAHRANI, N. 2½D Finite Element Method for Electrical Impedance Tomography Considering the Complete Electrode Model [online]. 2012. Master of Applied Science. Carleton University. Available at: <http://citeseerx.ist.psu.edu/viewdoc/download?doi=10.1.1.718.5235&rep=rep1&type=pdf>.
- [19] KHAN, T. A., and S. H. LING. Review on Electrical Impedance Tomography: Artificial Intelligence Methods and its Applications. *Algorithms* [online]. 2019, **12**(5), 88. Available at: doi:10.3390/a12050088

- [20] NISSINEN, A. *Modelling Errors in Electrical Impedance Tomography* [online]. Kuopio, 2011, 79. Doctor of Philosophy. University of Eastern Finland. ISBN 978-952-61-0428-7. Available at: https://erepo.uef.fi/bitstream/handle/123456789/10060/urn_isbn_978-952-61-0428-7.pdf.
- [21] CHENEY, M., D. ISAACSON, and J. NEWELL. Electrical impedance tomography. *Society for Industrial and Applied Mathematics* [online]. SIAM, 1999, **41**(1), 85-101. Available at: <http://homepages.rpi.edu/~newelj/sirev.pdf>
- [22] ADLER, A., and W. R. B. LIONHEART. Uses and abuses of EIDORS: an extensible software base for EIT. *Physiological Measurement* [online]. 2006, **27**(5), S25–S42. ISSN 0967-3334, 1361-6579. Available at: doi:10.1088/0967-3334/27/5/S03
- [23] TTAYAGARAJAN, T., M. PONNAVAIKKO, J. SHANMUGAM, R.C. PANDA, and Pg. RAO. Artificial neural networks: principle and application to model based control of drying systems - a review. *Drying Technology* [online]. 1998, **16**(6), 931–966. ISSN 0737-3937, 1532-2300. Available at: doi:10.1080/07373939808917449
- [24] GRAUPE, D. *Principles of artificial neural networks*. 3rd edition. New Jersey: World Scientific, 2013. Advanced series on circuits and systems, volume 7. ISBN 978-981-4522-73-1.
- [25] MARTIN, S., and Ch T. M. CHOI. Nonlinear Electrical Impedance Tomography Reconstruction Using Artificial Neural Networks and Particle Swarm Optimization. *IEEE Transactions on Magnetics* [online]. 2016, **52**(3), 1–4. ISSN 1941-0069. Available at: doi:10.1109/TMAG.2015.2488901
- [26] BARBOSA, V. A. F., R. R. RIBEIRO, A. R. S. FEITOSA, V. L. B. A. SILVA, A. D. D. ROCHA, R. C. FREITAS, R. E. SOUZA, and W. P. SANTOS. Reconstruction of Electrical Impedance Tomography Using Fish School Search, Non-Blind Search, and Genetic Algorithm. *International Journal of Swarm Intelligence Research (IJSIR)* [online]. 2017, **8**(2), 17–33. ISSN 1947-9263. Available at: doi:10.4018/IJSIR.2017040102
- [27] MICHALIKOVA, M., R. ABED, M. PRAUZEK, and J. KOZIOREK. Image reconstruction in electrical impedance tomography using neural network. In: *2014 Cairo International Biomedical Engineering Conference (CIBEC)* [online]. 2014, 39–42. ISSN 2156-6100. Available at: doi:10.1109/CIBEC.2014.7020959

- [28] ACHARJYA, D. P., and V. SANTHI, ed. *Bio-inspired computing for image and video processing*. Boca Raton: CRC Press, 2017. ISBN 978-1-4987-6592-3.
- [29] NERI, F., and V. TIRRONEN. Recent advances in differential evolution: a survey and experimental analysis. *Artificial Intelligence Review* [online]. 2010, **33**(1–2), 61–106. ISSN 0269-2821, 1573-7462. Available at: doi:10.1007/s10462-009-9137-2
- [30] RIBEIRO, R. R., A. R. S. FEITOSA, R. E. DE SOUZA, and W. P. DOS SANTOS. A modified differential evolution algorithm for the reconstruction of electrical impedance tomography images. In: *5th ISSNIP-IEEE Biosignals and Biorobotics Conference (2014): Biosignals and Robotics for Better and Safer Living (BRC)* [online]. 2014, 1–6. ISSN 2326-7844. Available at: doi:10.1109/BRC.2014.6880982
- [31] RIBEIRO, R. R., A. R. S. FEITOSA, R. E. DE SOUZA, and W. P. DOS SANTOS. Reconstruction of electrical impedance tomography images using chaotic self-adaptive ring-topology differential evolution and genetic algorithms. In: *2014 IEEE International Conference on Systems, Man, and Cybernetics (SMC)* [online]. 2014, 2605–2610. ISSN 1062-922X. Available at: doi:10.1109/SMC.2014.6974320
- [32] KING, I. ed. *Neural information processing: 13th international conference, ICONIP 2006, Hong Kong, China, October 3-6, 2006: proceedings*. Berlin; New York: Springer, 2006. Lecture notes in computer science, 4232–4234. ISBN 978-3-540-46479-2.
- [33] COLTON, D., and R. KRESS. *Inverse Acoustic and Electromagnetic Scattering Theory* [online]. ed. 2. Berlin Heidelberg: Springer-Verlag, 1998. Applied Mathematical Sciences. ISBN 978-3-662-03537-5. Available at: doi:10.1007/978-3-662-03537-5
- [34] LIONHEART, W. R. B. EIT reconstruction algorithms: pitfalls, challenges and recent developments. *Physiological Measurement* [online]. 2004, **25**(1), 125–142. ISSN 0967-3334, 1361-6579. Available at: doi:10.1088/0967-3334/25/1/021
- [35] BROWN, B. H., and A. D. SEAGAR. The Sheffield data collection system. *Clinical Physics and Physiological Measurement* [online]. 1987, **8**(4A), 91–97. ISSN 0143-0815. Available at: doi:10.1088/0143-0815/8/4A/012
- [36] COOK, R.D., G.J. SAULNIER, D.G. GISSER, J.C. GOBLE, J.C. NEWELL, and D. ISAACSON. ACT3: a high-speed, high-precision electrical impedance

- tomograph. *IEEE Transactions on Biomedical Engineering* [online]. 1994, **41**(8), 713–722. ISSN 00189294. Available at: doi:10.1109/10.310086
- [37] BERA, T. K., and J. NAGARAJU. Studying the resistivity imaging of chicken tissue phantoms with different current patterns in Electrical Impedance Tomography (EIT). *Measurement* [online]. 2012, **45**(4), 663–682. ISSN 0263-2241. Available at: doi:10.1016/j.measurement.2012.01.002
- [38] LOKE, M. H. Electrical imaging surveys for environmental and engineering studies. *A practical guide to 2-D and 3-D surveys* [online]. 1999. Available at: <http://pages.mtu.edu/~ctyoung/LOKENOTE.PDF>
- [39] POLYDORIDES, N., and W. R. B. LIONHEART. A Matlab toolkit for three-dimensional electrical impedance tomography: a contribution to the Electrical Impedance and Diffuse Optical Reconstruction Software project. *Measurement Science and Technology* [online]. 2002, **13**(12), 1871–1883. ISSN 0957-0233. Available at: doi:10.1088/0957-0233/13/12/310
- [40] LESPARRE, N., A. BOYLE, B. GRYCHTOL, J. CABRERA, J. MARTEAU, and A. ADLER. Electrical resistivity imaging in transmission between surface and underground tunnel for fault characterization. *Journal of Applied Geophysics* [online]. 2016, 128, 163–178. ISSN 0926-9851. Available at: doi:10.1016/j.jappgeo.2016.03.004
- [41] ADLER, A., and W. R. B. LIONHEART. Minimizing EIT image artefacts from mesh variability in finite element models. *Physiological Measurement* [online]. 2011, **32**(7), 823–834. ISSN 0967-3334. Available at: doi:10.1088/0967-3334/32/7/S07
- [42] KOLEHMAINEN, V., M. VAUHKONEN, P. KARJALAINEN, and J. KAIPIO. Assessment of errors in static electrical impedance tomography with adjacent and trigonometric current patterns. *Physiological measurement* [online]. 1997, **18**, 289–303. Available at: doi:10.1088/0967-3334/18/4/003
- [43] LIU, K., Y. WU, S. WANG, H. WANG, H. CHEN, B. CHEN, and J. YAO. Artificial Sensitive Skin for Robotics Based on Electrical Impedance Tomography. *Intelligent Systems* [online]. 2020, 1–13. Available at: doi:10.1002/aisy.201900161
- [44] WOO, E. J., P HUA, J. WEBSTER, W. TOMPKINS, and R. PALLAS-ARENY. Skin impedance measurements using simple and compound electrodes. *Medical & biological engineering & computing* [online]. 1992, **30**, 97–102. Available at: doi:10.1007/BF02446200

- [45] VILHUNEN, T., J. P. KAIPIO, P. J. VAUHKONEN, T. SAVOLAINEN, and M. VAUHKONEN. Simultaneous reconstruction of electrode contact impedances and internal electrical properties: I. Theory. *Measurement Science and Technology* [online]. 2002, **13**(12), 1848–1854. ISSN 0957-0233. Available at: doi:10.1088/0957-0233/13/12/307
- [46] HEIKKINEN, L. M., T. VILHUNEN, R. M. WEST, and M. VAUHKONEN. Simultaneous reconstruction of electrode contact impedances and internal electrical properties: II. Laboratory experiments. *Measurement Science and Technology* [online]. 2002, **13**(12), 1855–1861. ISSN 0957-0233. Available at: doi:10.1088/0957-0233/13/12/308
- [47] KOLEHMAINEN, V., M. LASSAS, and P. OLA. Electrical Impedance Tomography Problem With Inaccurately Known Boundary and Contact Impedances. *IEEE transactions on medical imaging* [online]. 2008, **27**, 1404–14. Available at: doi:10.1109/TMI.2008.920600
- [48] BOVERMAN, G., D. ISAACSON, G. SAULNIER, and J. NEWELL. Methods for Compensating for Variable Electrode Contact in EIT. *IEEE transactions on bio-medical engineering* [online]. 2009, **56**, 2762–72. Available at: doi:10.1109/TBME.2009.2027129
- [49] NISSINEN, A., V. KOLEHMAINEN, and J. KAIPIO. Compensation of Modelling Errors Due to Unknown Domain Boundary in Electrical Impedance Tomography. *IEEE transactions on medical imaging* [online]. 2011, **30**, 231–42. Available at: doi:10.1109/TMI.2010.2073716
- [50] DARDÉ, J., H. HAKULA, N. HYVÖNEN, and S. STABOULIS. Fine-tuning electrode information in electrical impedance tomography. *Inverse Problems and Imaging* [online]. 2012, **6**. Available at: doi:10.3934/ipi.2012.6.399
- [51] DEMIDENKO, E., A. BORSIC, Y. WAN, R. HALTER, and A. HARTOV. Statistical Estimation of EIT Electrode Contact Impedance Using a Magic Toeplitz Matrix. *IEEE Transactions on Biomedical Engineering* [online]. 2011, **58**, 2194–2201. Available at: doi:10.1109/TBME.2011.2125790
- [52] HYVÖNEN, N., A. SEPPÄNEN, and S. STABOULIS. Optimizing Electrode Positions in Electrical Impedance Tomography. *SIAM Journal on Applied Mathematics* [online]. 2014, **74**. Available at: doi:10.1137/140966174
- [53] BOVERMAN, G., D. ISAACSON, J. C. NEWELL, G. J. SAULNIER, T.-J. KAO, B. C. AMM, X. WANG, D. M. DAVENPORT, D. H. CHONG, R.

- SAHNI a J. M. ASHE. Efficient Simultaneous Reconstruction of Time-Varying Images and Electrode Contact Impedances in Electrical Impedance Tomography. *IEEE Transactions on Biomedical Engineering* [online]. 2017, **64**(4), 795–806. ISSN 1558-2531. Available at: doi:10.1109/TBME.2016.2578646
- [54] SMYL, D., and D. LIU. Optimizing Electrode Positions in 2-D Electrical Impedance Tomography Using Deep Learning. *IEEE Transactions on Instrumentation and Measurement* [online]. 2020, **69**(9), 6030–6044. ISSN 1557-9662. Available at: doi:10.1109/TIM.2020.2970371
- [55] HORESH, L., M. SCHWEIGER, M. BOLLHÖFER, A. DOUIRI, D. HOLDER, and S.R. ARRIDGE. Multilevel preconditioning for 3D large-scale soft-field medical applications modelling. *International Journal of Information and Systems Sciences*. 2006, 2, 532–556.
- [56] BORSIC, A., R. HALTER, Y. WAN, A. HARTOV, and K. D. PAULSEN. Electrical impedance tomography reconstruction for three-dimensional imaging of the prostate. *Physiological Measurement* [online]. 2010, **31**(8), S1–S16. ISSN 0967-3334. Available at: doi:10.1088/0967-3334/31/8/S01
- [57] SOLEIMANI, M., C.E. POWELL, and N. POLYDORIDES. Improving the forward solver for the complete electrode model in EIT using algebraic multigrid. *IEEE Transactions on Medical Imaging* [online]. 2005, **24**(5), 577–583. ISSN 1558-254X. Available at: doi:10.1109/TMI.2005.843741
- [58] BORSIC, A., E. A. ATTARDO, and R. J. HALTER. Multi-GPU Jacobian accelerated computing for soft-field tomography. *Physiological Measurement* [online]. 2012, **33**(10), 1703–1715. ISSN 0967-3334. Available at: doi:10.1088/0967-3334/33/10/1703
- [59] JEHL, M., A. DEDNER, T. BETCKE, K. ARISTOVICH, R. KLÖFKORN, and D. HOLDER. A Fast Parallel Solver for the Forward Problem in Electrical Impedance Tomography. *IEEE Transactions on Biomedical Engineering* [online]. 2015, **62**(1), 126–137. ISSN 1558-2531. Available at: doi:10.1109/TBME.2014.2342280
- [60] ZONG, Z., Y. WANG, and Z. WEI. A Review of Algorithms and Hardware Implementations in Electrical Impedance Tomography (Invited). *Progress In Electromagnetics Research* [online]. 2020, **169**, 59–71. ISSN 1070-4698. Available at: doi:10.2528/PIER20120401

- [61] PADILHA LEITZKE, J., and H. ZANGL. A Review on Electrical Impedance Tomography Spectroscopy. *Sensors* [online]. 2020, **20**(18), 5160. Available at: doi:10.3390/s20185160
- [62] WANG, M., Y. MA, N. HOLLIDAY, Y. DAI, R.A. WILLIAMS, and G. LUCAS. A high-performance EIT system. *IEEE Sensors Journal* [online]. 2005, **5**(2), 289–299. ISSN 1558-1748. Available at: doi:10.1109/JSEN.2005.843904
- [63] MCEWAN, A., A. ROMSAUEROVA, R. YERWORTH, L. HORESH, R. BAYFORD, and D. HOLDER. Design and calibration of a compact multi-frequency EIT system for acute stroke imaging. *Physiological Measurement* [online]. 2006, **27**(5), S199–S210. ISSN 0967-3334, 1361-6579. Available at: doi:10.1088/0967-3334/27/5/S17
- [64] KOURUNEN, J., T. SAVOLAINEN, A. LEHIKONEN, M. VAUHKONEN, and L. M. HEIKKINEN. Suitability of a PXI platform for an electrical impedance tomography system. *Measurement Science and Technology* [online]. 2008, **20**(1), 015503. ISSN 0957-0233. Available at: doi:10.1088/0957-0233/20/1/015503
- [65] YUE, X., and Ch. MCLEOD. FPGA design and implementation for EIT data acquisition. *Physiological Measurement* [online]. 2008, **29**(10), 1233–1246. ISSN 0967-3334, 1361-6579. Available at: doi:10.1088/0967-3334/29/10/007
- [66] HALTER, R. J., A. HARTOV, and K. D. PAULSEN. A Broadband High-Frequency Electrical Impedance Tomography System for Breast Imaging. *IEEE Transactions on Biomedical Engineering* [online]. 2008, **55**(2), 650–659. ISSN 1558-2531. Available at: doi:10.1109/TBME.2007.903516
- [67] JIA, J., M. WANG, H. I. SCHLABERG, and H. LI. A novel tomographic sensing system for high electrically conductive multiphase flow measurement. *Flow Measurement and Instrumentation* [online]. 2010, **21**(3), Special Issue: Validation and Data Fusion for Process Tomographic Flow Measurements, 184–190. ISSN 0955-5986. Available at: doi:10.1016/j.flowmeasinst.2009.12.002
- [68] WANG, M. *Industrial Tomography: Systems and Applications*. B.m.: Elsevier, 2015. ISBN 978-1-78242-123-8.
- [69] GRIEVE, B.D., S. MURPHY, A. BURNETT-THOMPSON, and T.A. YORK. An accessible electrical impedance tomograph for 3D imaging. *Transactions of the Institute of Measurement and Control* [online]. 2010, **32**(1), 31–50. ISSN 0142-3312. Available at: doi:10.1177/0142331208100108

- [70] DONG, F., C. XU, Z. ZHANG, and S. REN. Design of Parallel Electrical Resistance Tomography System for Measuring Multiphase Flow. *Chinese Journal of Chemical Engineering* [online]. 2012, **20**(2), 368–379. ISSN 1004-9541. Available at: doi:10.1016/S1004-9541(12)60400-5
- [71] OH, T. I., H. WI, D. Y. KIM, P. J. YOO, and E. J. WOO. A fully parallel multi-frequency EIT system with flexible electrode configuration: KHU Mark2. *Physiological Measurement* [online]. 2011, **32**(7), 835–849. ISSN 0967-3334, 1361-6579. Available at: doi:10.1088/0967-3334/32/7/S08
- [72] WI, H., H. SOHAL, A. L. MCEWAN, E. J. WOO, and T. I. OH. Multi-Frequency Electrical Impedance Tomography System With Automatic Self-Calibration for Long-Term Monitoring. *IEEE Transactions on Biomedical Circuits and Systems* [online]. 2014, **8**(1), 119–128. ISSN 1940-9990. Available at: doi:10.1109/TBCAS.2013.2256785
- [73] HONG, S., J. LEE, J. BAE, and H.-J. YOO. A 10.4 mW electrical impedance tomography SoC for portable real-time lung ventilation monitoring system. In: *2014 IEEE Asian Solid-State Circuits Conference (A-SSCC)* [online]. 2014, 193–196. Available at: doi:10.1109/ASSCC.2014.7008893
- [74] HUANG, S.-K., and K. J. LOH. Development of a portable electrical impedance tomography data acquisition system for near-real-time spatial sensing. In: *Sensors and Smart Structures Technologies for Civil, Mechanical, and Aerospace Systems 2015* [online]. B.m.: International Society for Optics and Photonics, 2015, 94350E. Available at: doi:10.1117/12.2083946
- [75] KHAN, S., P. MANWARING, A. BORSIC, and R. HALTER. FPGA-Based Voltage and Current Dual Drive System for High Frame Rate Electrical Impedance Tomography. *IEEE Transactions on Medical Imaging* [online]. 2015, **34**(4), 888–901. ISSN 1558-254X. Available at: doi:10.1109/TMI.2014.2367315
- [76] PAŘÍLKOVÁ, J., and K. RADKOVSKÝ. *Z-meter IV, user's manual*. 2016, Brno
- [77] RINTOUL, J. Documentation and Tutorials for OpenEIT — OpenEIT 1.0.0 documentation. *OpenEIT* [online]. 2018. Available at: <https://openeit.github.io/docs/html/index.html>
- [78] XU, Z., J. YAO, Z. WANG, Y. LIU, H. WANG, B. CHEN, and H. WU. Development of a Portable Electrical Impedance Tomography System for Biomedical

- Applications. *IEEE Sensors Journal* [online]. 2018, **18**(19), 8117–8124. ISSN 1558-1748. Available at: doi:10.1109/JSEN.2018.2864539
- [79] TAN, C., S. LIU, J. JIA, and F. DONG. A Wideband Electrical Impedance Tomography System Based on Sensitive Bioimpedance Spectrum Bandwidth. *IEEE Transactions on Instrumentation and Measurement* [online]. 2020, **69**(1), 144–154. ISSN 1557-9662. Available at: doi:10.1109/TIM.2019.2895929
- [80] DUŠEK, J., J. MIKULKA, Z. MŮNSTEROVÁ, and J. PAŘÍLKOVÁ. The Effect of Cylindrical Tank Deformation on Forward Solution in Electrical Impedance Tomography. *EUREKA 2020*. EUREKA. Brno: VUTIUUM, Brno University of Technology, 2020. 60-63. ISBN: 978-80-214-5862-8. ISSN: 2464-4595.
- [81] DUŠEK, J., and J. MIKULKA. Measurement-Based Domain Parameter Optimization in Electrical Impedance Tomography Imaging. *Sensors* [online]. 2021, **21**(7), 2507. Available at: doi:10.3390/s21072507
- [82] LAGARIAS, J., J. REEDS, M. WRIGHT, and P. WRIGHT. Convergence Properties of the Nelder–Mead Simplex Method in Low Dimensions. *SIAM Journal on Optimization* [online]. 1998, **9**, 112–147. Available at: doi:10.1137/S1052623496303470
- [83] LASHEEN, A., A. EL-GARHY, E. SAAD, and S. EID. Using hybrid genetic and Nelder-Mead algorithm for decoupling of MIMO systems with application on two coupled distillation columns process. *International Journal of Mathematics and Computers in Simulation*. 2009, **3**.
- [84] BOZORG-HADDAD, O., F. HAMED, H. OROUJI, M. PAZOKI, and H. LOAICIGA. A Re-Parameterized and Improved Nonlinear Muskingum Model for Flood Routing. *Water Resources Management* [online]. 2015, **29**. Available at: doi:10.1007/s11269-015-1008-9
- [85] DIMAS, Ch., and P. P. SOTIRIADIS. Electrical impedance tomography image reconstruction for adjacent and opposite strategy using FEMM and EIDORS simulation models. In: *2018 7th International Conference on Modern Circuits and Systems Technologies (MOCASST)* [online]. Thessaloniki: IEEE, 2018, 1–4. ISBN 978-1-5386-4788-2. Available at: doi:10.1109/MOCASST.2018.8376604
- [86] KRČMAŘÍK, D., M. PETRŮ, and J. KOČÍ. Thorax measurement and analysis using electrical impedance tomography. *Vibroengineering PROCEDIA* [online]. 2019, **26**, 68–73. ISSN 2345-0533. Available at: doi:10.21595/vp.2019.20986

- [87] BARA, A., A. SALAMI, K. KOFFI MAWUGNO, A. GUENOUKPATI, O. DJANDJA, and K.-S. BEDJA. Estimation of Soils Electrical Resistivity using Artificial Neural Network Approach. *American Journal of Applied Sciences* [online]. 2019, **16**, 43–58. Available at: doi:10.3844/ajassp.2019.43.58
- [88] DUŠEK, J., J. MIKULKA, M. BALAJKA, J. DĚDKOVÁ, J. PAŘÍLKOVÁ, and Z. MŮNSTEROVÁ. Designing a Cost-Effective Multiplexer for Electrical Impedance Tomography. In: *2019 11th International Congress on Ultra Modern Telecommunications and Control Systems and Workshops (ICUMT)* [online]. 2019, 1–4. ISSN 2157-023X. Available at: doi:10.1109/ICUMT48472.2019.8970696
- [89] GHORBANI, R., and M. NAHVI. Analysis of Performance of Howland AC Current Source for Electrical Impedance Spectro-Tomography. *Sensing and Imaging* [online]. 2019, **20**(1), 28. ISSN 1557-2072. Available at: doi:10.1007/s11220-019-0251-1
- [90] DUŠEK, J., J. MIKULKA, Z. MŮNSTEROVÁ, and J. PAŘÍLKOVÁ. Designing portable multiplexer for electrical impedance tomography. In *EUREKA 2019 - 7th Colloquium and Working Session*. EUREKA. Brno: Brno University of Technology, VUTIUM, 2019. 86-89. ISBN: 978-80-214-5729-4. ISSN: 2464-4595.
- [91] DUŠEK, J., and J. MIKULKA. Electrical Impedance Tomography-Based Spatial Reconstruction of Admittivity in a Cylindrical Object. In: *2020 19th International Conference on Mechatronics - Mechatronika (ME)* [online]. 2020, 1–6. Available at: doi:10.1109/ME49197.2020.9286467
- [92] DUŠEK, J., A. VÉJAR, T. RYMARCZYK, and J. MIKULKA. Convergence error exploration for electrical impedance tomography problems with open and closed domains. In: *2018 International Interdisciplinary PhD Workshop (IIPHDW)* [online]. 2018, 39–44. Available at: doi:10.1109/IIPHDW.2018.8388241
- [93] DUŠEK, J. Acceleration of Electrical Impedance Tomography Algorithm with Open and Closed Domain Model Evaluation. In *Proceedings of the 24th Conference STUDENT EEICT 2018*. Brno: 2018. 508-512. ISBN: 978-80-214-5614-3.
- [94] CHAWNER, J. Accuracy, Convergence and Mesh Quality. *Pointwise* [online]. 2012. Available at: <https://blog.pointwise.com/2012/07/05/accuracy-convergence-and-mesh-quality/>

- [95] VAUHKONEN, M., W. LIONHEART, L. HEIKKINEN, P. VAUHKONEN, and Jari KAIPIO. A matlab package for the EIDORS project to reconstruct two-dimensional EIT images. *Physiological measurement* [online]. 2001, **22**, 107–11. Available at: doi:10.1088/0967-3334/22/1/314
- [96] DUŠEK, J., D. HLADKÝ, and J. MIKULKA. Electrical impedance tomography methods and algorithms processed with a GPU. In: *2017 Progress In Electromagnetics Research Symposium - Spring (PIERS)* [online]. 2017, 1710–1714. Available at: doi:10.1109/PIERS.2017.8262025
- [97] DUŠEK, J., and J. MIKULKA. Using a GPU to Accelerate Electrical Impedance Tomography Algorithms. In *Proceedings of IIPhDW 2017 in Lodz*. Lodz, Polsko: 2017. 59-63. ISBN: 978-83-7283-858-2.
- [98] MŮNSTEROVÁ, Z., J. PAŘÍLKOVÁ, J. DUŠEK, and J. MIKULKA. Electrical impedance reconstruction measured by modified electrical impedance spectrometry. In *EUREKA 2019 - 7th Colloquium and Working Session*. EUREKA. Brno: Brno University of Technology, VUTIUM, 2019. 93-96. ISBN: 978-80-214-5729-4. ISSN: 2464-4595.
- [99] DUŠEK, J., J. MIKULKA, Z. MŮNSTEROVÁ, and J. PAŘÍLKOVÁ. System for conductivity reconstruction of soil sample based on electrical impedance tomography. In *EUREKA 2019 - 7th Colloquium and Working Session*. EUREKA. Brno: Brno University of Technology, VUTIUM, 2019. 90-92. ISBN: 978-80-214-5729-4. ISSN: 2464-4595.
- [100] DUŠEK, J., J. MIKULKA, J. PAŘÍLKOVÁ, and Z. MŮNSTEROVÁ. Reconstruction of the real and imaginary parts of tank model admittance via electrical impedance tomography. *Elektrorevue*. 2019, **21**(2), 1-7. ISSN: 1213-1539. Available at: <http://www.elektrorevue.cz>

Author's publications

DUŠEK, J., and J. MIKULKA. Measurement-Based Domain Parameter Optimization in Electrical Impedance Tomography Imaging. *Sensors* [online]. 2021, **21**(7), 2507. Available at: doi:10.3390/s21072507

DUŠEK, J., and J. MIKULKA. Electrical Impedance Tomography-Based Spatial Reconstruction of Admittivity in a Cylindrical Object. In: *2020 19th International Conference on Mechatronics - Mechatronika (ME)* [online]. 2020, 1–6. Available at: doi:10.1109/ME49197.2020.9286467

DUŠEK, J., J. MIKULKA, Z. MŮNSTEROVÁ, and J. PAŘÍLKOVÁ. The Effect of Cylindrical Tank Deformation on Forward Solution in Electrical Impedance Tomography. *EUREKA 2020*. EUREKA. Brno: VUTIAM, Brno University of Technology, 2020. 60-63. ISBN: 978-80-214-5862-8. ISSN: 2464-4595.

PAŘÍLKOVÁ, J., Z. ZACHOVAL, J. JANDORA, B. GJUNSBURGS, S. KRÁLÍKOVÁ, L. PAŘÍLEK, Z. MŮNSTEROVÁ, J. MIKULKA, J. DUŠEK, and R. ŠEVČÍK. Electrical Impedance Spectrometry for Hydrological Analysis and Koberice Dam Characterization. *EUREKA 2020*. EUREKA. Brno: VUTIAM, Brno University of Technology, 2020. 46-49. ISBN: 978-80-214-5862-8. ISSN: 2464-4595.

PAŘÍLKOVÁ, J., Z. ZACHOVAL, Z. MŮNSTEROVÁ, J. JANDORA, J. MIKULKA, J. DUŠEK, D. JUŘIČKA, T. ZYDRON, A. GRUCHOT, M. GOMBOS, D. PAVELKOVÁ, B. GJUNSBURGS, A. RADZEVICIUS, and R. SKOMINAS. Bode and Nyquist Plots: Assistance in Soil Characterization. *Journal of Marine Technology and Environment*, 2020, **2**, 29-38. ISSN: 1844-6116.

DUŠEK, J., J. MIKULKA, Z. MŮNSTEROVÁ, and J. PAŘÍLKOVÁ. System for conductivity reconstruction of soil sample based on electrical impedance tomography. In *EUREKA 2019 - 7th Colloquium and Working Session*. EUREKA. Brno: Brno University of Technology, VUTIAM, 2019. 90-92. ISBN: 978-80-214-5729-4. ISSN: 2464-4595.

MIKULKA, J., J. DUŠEK, J. DĚDKOVÁ, J. PAŘÍLKOVÁ, and Z. MŮNSTEROVÁ. A Fast and Low-cost Measuring System for Electrical Impedance Tomography. In: *2019 Photonics Electromagnetics Research Symposium - Spring (PIERS-Spring)* [online]. 2019, 3751–3755. ISSN 1559-9450. Available at:

doi:10.1109/PIERS-Spring46901.2019.9017338

DUŠEK, J., J. MIKULKA, M. BALAJKA, J. DĚDKOVÁ, J. PAŘÍLKOVÁ, and Z. MŮNSTEROVÁ. Designing a Cost-Effective Multiplexer for Electrical Impedance Tomography. In: *2019 11th International Congress on Ultra Modern Telecommunications and Control Systems and Workshops (ICUMT)* [online]. 2019, 1–4. ISSN 2157-023X. Available at: doi:10.1109/ICUMT48472.2019.8970696

MŮNSTEROVÁ, Z., J. PAŘÍLKOVÁ, J. DUŠEK, and J. MIKULKA. Electrical impedance reconstruction measured by modified electrical impedance spectrometry. In *EUREKA 2019 - 7th Colloquium and Working Session*. EUREKA. Brno: Brno University of Technology, VUTIUUM, 2019. 93-96. ISBN: 978-80-214-5729-4. ISSN: 2464-4595.

DUŠEK, J., J. MIKULKA, J. PAŘÍLKOVÁ, and Z. MŮNSTEROVÁ. Reconstruction of the real and imaginary parts of tank model admittance via electrical impedance tomography. *Elektrorevue*. 2019, **21**(2), 1-7. ISSN: 1213-1539. Available at: <http://www.elektrorevue.cz>

DUŠEK, J., J. MIKULKA, Z. MŮNSTEROVÁ, and J. PAŘÍLKOVÁ. Designing portable multiplexer for electrical impedance tomography. In *EUREKA 2019 - 7th Colloquium and Working Session*. EUREKA. Brno: Brno University of Technology, VUTIUUM, 2019. 86-89. ISBN: 978-80-214-5729-4. ISSN: 2464-4595.

PAŘÍLKOVÁ, J., Z. MŮNSTEROVÁ, J. MIKULKA, J. DUŠEK, J. NOVOTNÁ, D. JUŘIČKA, B. GJUNSBURGS, M. NEDEV, Y. YANEV, M. GOMBOŠ, D. PAVELKOVÁ, T. ZYDRONĚ, and A. GRUCHOT. Utilization of earth electric impedance mapping in water engineering. *ACTA HYDROLOGICA SLOVACA*, 2018, **19**(2), 287-295. ISSN: 1335-6291.

DUŠEK, J., A. VÉJAR, T. RYMARCZYK, and J. MIKULKA. Convergence error exploration for electrical impedance tomography problems with open and closed domains. In: *2018 International Interdisciplinary PhD Workshop (IIPHDW)* [online]. 2018, 39–44. Available at: doi:10.1109/IIPHDW.2018.8388241

MIKULKA, J., D. HLADKÝ, and J. DUŠEK. Modeling the Propagation of a Modulated Ultrasonic Wave for Parametric Speaker Design. In *8th International Interdisciplinary PhD Workshop*. 2018. 1-4. ISBN: 978-83-7663-250-6.

DUŠEK, J. Acceleration of Electrical Impedance Tomography Algorithm with Open and Closed Domain Model Evaluation. In *Proceedings of the 24th Conference STUDENT EEICT 2018*. Brno: 2018. 508-512. ISBN: 978-80-214-5614-3.

PAŘÍLKOVÁ, J., L. PAŘÍLEK, Z. MŮNSTEROVÁ, J. MIKULKA, J. DUŠEK, and R. ŠEVČÍK. Changes of water content on upstream face of dam Kobeřice. In *EUREKA 2018 6th colloquium and working session*. EUREKA. Brno: Brno University of Technology, VUTIUUM, 2018. 22-25. ISBN: 978-80-214-5646-4. ISSN: 2464-4595.

KŘÍŽ, T., and J. DUŠEK. Electrical impedance tomography in the testing of material defects. In: *2017 Progress In Electromagnetics Research Symposium - Spring (PIERS)* [online]. 2017, 90–94. Available at: doi:10.1109/PIERS.2017.8261712

KŘÍŽ, T., and J. DUŠEK. Highly accurate image reconstruction using electrical impedance tomography. In: *2017 Progress In Electromagnetics Research Symposium - Spring (PIERS)* [online]. 2017, 767–771. Available at: doi:10.1109/PIERS.2017.8261845

MIKULKA, J., D. HLADKÝ, J. DUŠEK, and T. KŘÍŽ. The optimization of electrical tomography algorithms. In: *2017 Progress In Electromagnetics Research Symposium - Spring (PIERS)* [online]. 2017, 763–766. Available at: doi:10.1109/PIERS.2017.8261844

DUŠEK, J., D. HLADKÝ, and J. MIKULKA. Electrical impedance tomography methods and algorithms processed with a GPU. In: *2017 Progress In Electromagnetics Research Symposium - Spring (PIERS)* [online]. 2017, 1710–1714. Available at: doi:10.1109/PIERS.2017.8262025

DUŠEK, J., and J. MIKULKA. Using a GPU to Accelerate Electrical Impedance Tomography Algorithms. In *Proceedings of IIPhDW 2017 in Lodz*. Lodz, Polsko: 2017. 59-63. ISBN: 978-83-7283-858-2.

DUŠEK, J. Reaktivní magnetronové naprašování vrstev oxidu hlinitého. In *Proceedings of the 22nd Conference STUDENT EEICT 2016*. Brno: Brno University of Technology. 2016. 231-233. ISBN: 978-80-214-5350-0.

List of Symbols

∇_a	Gradient operator
$\nabla \cdot \mathbf{A}$	Divergence operator
$\nabla \times \mathbf{A}$	Curl operator
\mathbf{A}^{-1}	Matrix inverse
\mathbf{A}^T	Matrix transpose
\mathbf{A}^\dagger	Moore-Penrose pseudoinverse: $\mathbf{A}^\dagger = (\mathbf{A}^T \mathbf{A})^{-1} \mathbf{A}^T$
\mathbf{A}	System matrix
\mathbf{b}	Right-hand side vector
\mathbf{B}	Magnetic flux density
\mathbf{D}	Electric flux density
D	Model dimension
dS	Surface of the domain Ω
$d\Omega$	Boundary of the domain Ω
\mathbf{E}	Electric field density
e	Randomly generated value
$ E_l $	Surface of the l -th electrode E
f	Frequency
\mathbf{f}	Load vector
$f(p)$	Optimization function including a parameter (initial conductivity, electrode placement, domain shape deformation)
\mathbf{H}	Magnetic field strength
I	Electric current
\mathbf{i}	Vector of injected currents on the boundary through the electrode
I_l	Excitation current on the electrode l

\mathbf{J}	Current density
\mathbf{J}_i	Jacobian
\mathbf{K}	Stiffness matrix
L	Number of electrodes
n	Dimension of space
\mathbf{n}	Boundary normal vector in the domain Ω
px	Number of pixels
R	Electrical resistance
\mathbf{R}	Regularization matrix
TV_β	Regularization term of the total variation method
t	Time
U	Voltage
\mathbf{U}_{FEM}	Vector of voltages computed via the forward task
U_l	Voltage on the electrode l
\mathbf{U}_M	Vector of measured voltages on the boundary of the domain Ω
W	FEM basis function
\mathbf{x}	Vector of an unknown quantity
\mathbf{x}_0	Vector containing the initial value of an unknown quantity
X	Reactance
x_i	Simplex vertex
$\hat{\mathbf{z}}_l$	Contact impedance
Z	Impedance module
α	Regularization parameter
β	Parameter of the total variation characterizing the smoothness of the objective function $\Psi(\sigma)$

$\frac{\partial}{\partial x}$	Partial derivative with respect to x
$\delta\sigma$	Difference between the original and reconstructed conductivities
Δ	Difference of the specified reconstructed quantity given by the difference inverse algorithm
ϵ	Permittivity
μ	Permeability
$\sigma(x)$	Conductivity in the space of domain Ω
φ	Phase shift of signals
$\varphi(x)$	Electrical potential in the space of domain Ω
$\Psi(\sigma)$	Objective function related to the conductivity
ω	Angular frequency
Ω	Domain, the region of interest

List of Abbreviations

2D	Two-Dimensional
3D	Three-Dimensional
ADC	Analog to Digital Converter
ANN	Artificial Neural Network
ASP	Adjacent Stimulation Pattern
CEM	Complete Electrode Model
CPU	Central Processing Unit
CMRR	Common Mode Rejection Ratio
CUDA	Compute Unified Device Architecture
DAC	Digital to Analog Converter
DDS	Direct Digital Synthesis - function generator
DIP	Dual In-line Package
DSBGA	Die-Size Ball Grid Array
EIDORS	Electrical Impedance and Diffuse Optics Reconstruction Software
EIT	Electrical Impedance Tomography
ERT	Electrical Resistive Tomography
FEM	Finite Element Method
FPGA	Field-Programmable Gate Array
GA	Genetic Algorithm
GPU	Graphical Processing Unit
GREIT	Graz consensus Reconstruction algorithm for EIT
IAR	Inhomogeneity Area Ratio - ratio between the original and reconstructed conductivity areas of the inhomogeneity
KIT 4	Kuopio Impedance Tomograph 4

LFCSP	Lead Frame Chip Scale Package
LSM	Least Square Method
MCU	Microcontroller Unit
MFEIT	Multiple Frequency EIT
MMSE	Minimum Mean Square Error
MSOP	Mini Small Outline Package
NOSER	Newton's One Step Error Reconstructor
OSP	Opposite Stimulation Pattern
OXBACT	Oxford Brookes Tomograph
PARDISO	Parallel Sparse Direct Solver
PEITS	Parallel EIT Software
PETSc	Portable, Extensible Toolkit for Scientific Computation
PD-IPM	Primar-Dual Interior-Point-Method
PDE	Partial Differential Equation
PGA	Programmable Gain Amplifier
PLI EIT	Precise, Low Impedance EIT system - measuring unit
RAM	Random Access Memory
RRMSE	Relative Root Mean Square Error
SFEIT	Single Frequency EIT
SNR	Signal to Noise Ratio
SOIC	Small Outline Integrated Circuit
SOT	Small Outline Transistor
SSE	Sum Square Error
SSOP	Shrink Small Outline Package
TDS	Total Dissolved Solids - conductometer

TSSOP	Thin Shrink Small Outline Package
VCCS	Voltage-Controlled Current Source
VSSOP	Very thin Shrink Small Outline Package
VQFN	Very thin Quad-Flat No-leads package
VRAM	Video Random Access Memory

A Preliminary results

This final chapter briefly summarizes the outcomes of an experimental measurement of a soil sample and a glass inserted in water. The data and results were created within project FAST/FEKT-J-18-5385.

Reconstructing the soil sample

The blind reconstruction experiment utilized a sample consisting of sand and clay. The data were collected via adjacent driving, the excitation current being 0.3 mA at 1 kHz. In the image reconstruction, we exploited the Gauss-Newton method adopted from the EIDORS toolbox, relying on Tikhonov regularization as the supporting procedure. The applied tomograph, filled with sand with clay, and the reconstructed conductivity distribution are presented in Fig. A.1 [99].

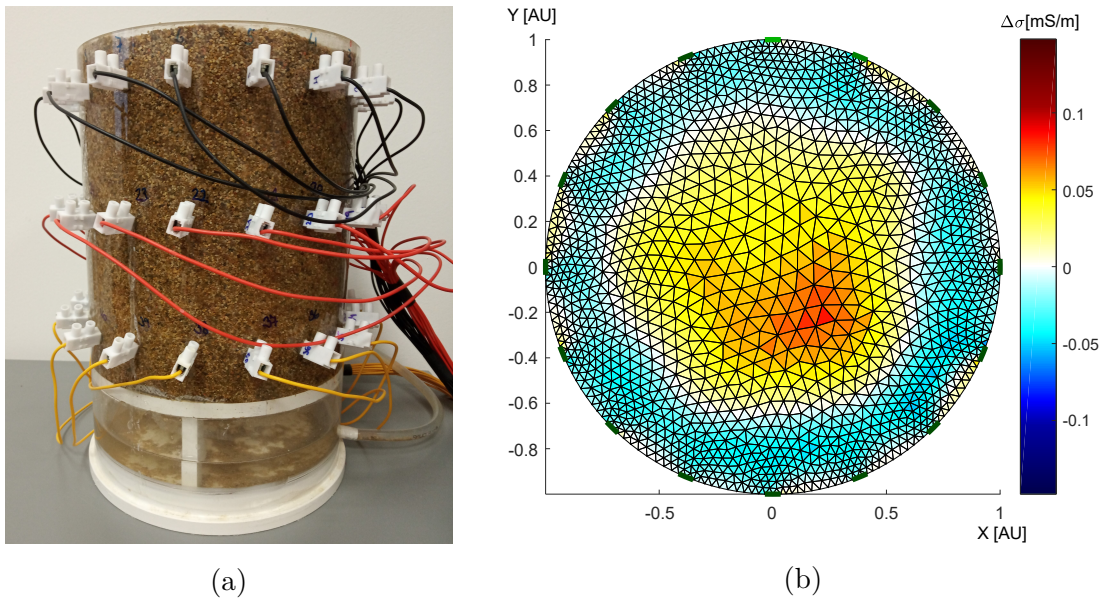


Fig. A.1: (a) The setup of the experiment; (b) the conductivity distribution of the soil sample, computed via a difference inverse algorithm [99].

The image reconstruction positioned the clay slightly below the center of the sand. Such an erroneous location can be attributed to material displacement due to gradual compaction of the soil; measurement; and reconstruction error [99].

Reconstructing the glass inserted in water

We filled the tomograph with water and inserted a glass cylinder, setting the excitation current to be 0.3 mA at 1 kHz. As regards the configuration and the measuring pattern, we employed 16 electrodes and adjacent driving, respectively. The measurement setup and the corresponding difference of the reconstructed admittivity distribution obtained through the Gauss-Newton method (expanded to involve a Tikhonov penalty) are visualized in Fig. A.2 [100].

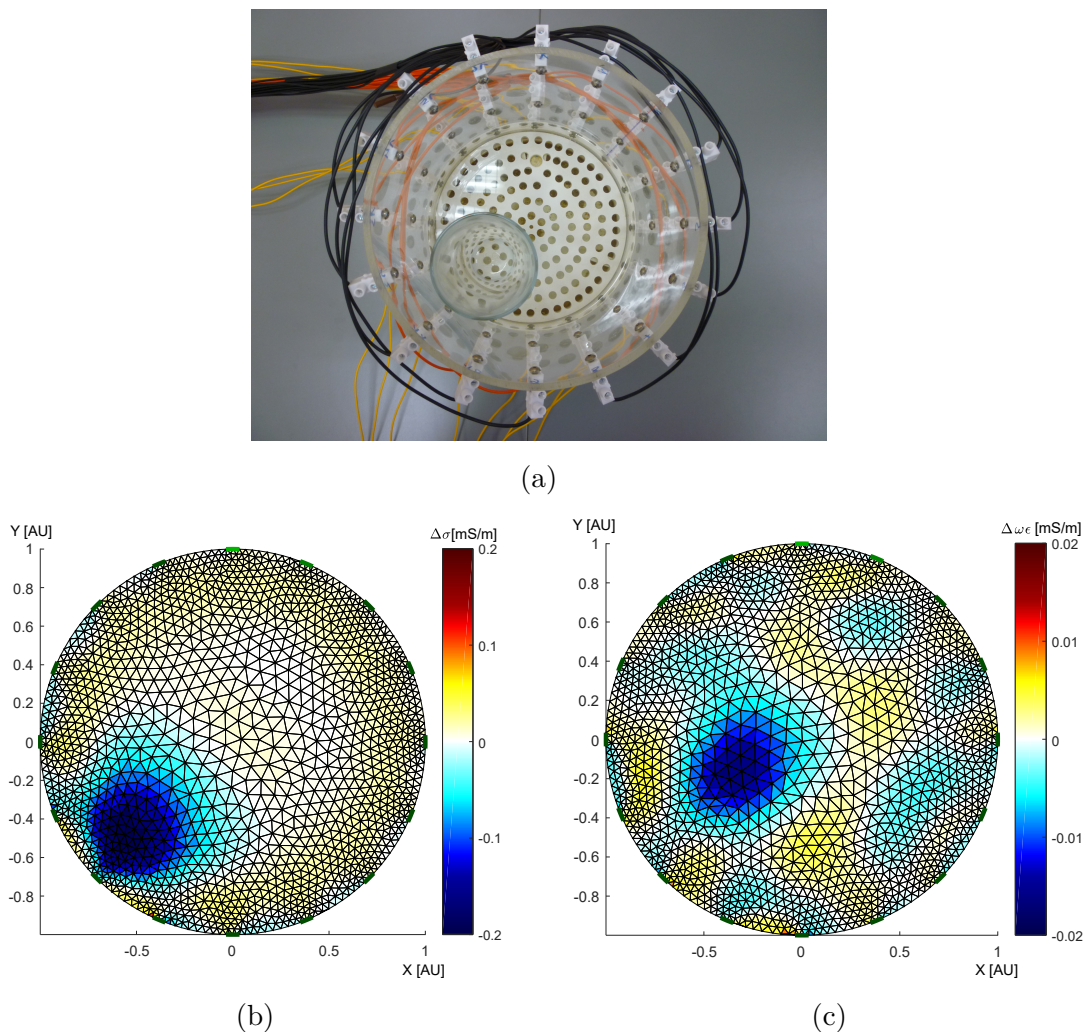


Fig. A.2: (a) The setup of the experiment, and the reconstructed differences of the (b) real and the (c) imaginary parts of admittivity [100].

In the reconstructed admittivity images, the real part could be localized precisely near the 11th electrode, while the imaginary component was situated farther from the boundary. The difference between the admittivity components had probably been caused by the uncertainty and the error in measuring the signal phase shift. The measurement was performed manually and took 3 hours [100].